Pyrometric Probes Based on Silicon Carbide Crystals

V. A. Karachinov, S. V. Il'in, and D. V. Karachinov

Novgorod State University, Velikiĭ Novgorod, Russia
e-mail: svyaz@novgorod.net
Received January 12, 2005

Abstract—We describe and characterize silicon carbide crystal devices of a new type—pyrometric probes, which can be used for temperature field measurements in hot gas flows. © *2005 Pleiades Publishing, Inc.*

Introduction. Measurement of the temperature of a hot gas flow is important both in basic research and in practical applications related to the diagnostics of various technical systems (gas welding equipment, metallurgical furnaces, jet engines, etc.) [1–3]. As is known, contactless pyrometric and spectroscopic methods can provide for the measurement of a maximum or average temperature of a gas flow, while the temperature distributions in selected cross sections of the flow are usually studied using probes based on thermal sensors such as thermocouples and hot tubes [3, 4]. Made of traditional materials, such probes are characterized by considerable thermal inertia and rather short working life, which is caused by rapid degradation in a highly reactive hot gas flow. Among the refractory compounds stable on heating above 1000°C in air, of considerable interest from the standpoint of pyrometry is silicon carbide [5]. This material was used for a long time for manufacturing polycrystalline Silit heaters and globars, and thin-film structures of the "silicon-carbide-on-insulator" type are used in modern IR spectroscopy [6].

This Letter presents the results of investigations aimed at the development of silicon carbide pyrometric probes (microradiators) for temperature measurements in hot gas flows.

Experimental. Pyrometric probes (single and multielement) were made of single crystal silicon carbide (SiC) by means of erosive profiling in a liquid dielectric medium [7, 8]. The initial 6H-SiC⟨N⟩ single crystal ingots grown using the classical Lely method or the LETI technique had an uncompensated donor concentration of $N_d - N_a = (1-3) \times 10^{18}$ cm^{-3} and exhibited no visible macroscopic defects. The crystals cut from the ingots were etched in KOH melt at $T = 600°C$ and mounted on cylindrical holders made of polycrystalline SiC. The probe could be placed at a desired point of a gas flow with the aid of a special 3D-positioning device with an accuracy of ±0.5 mm.
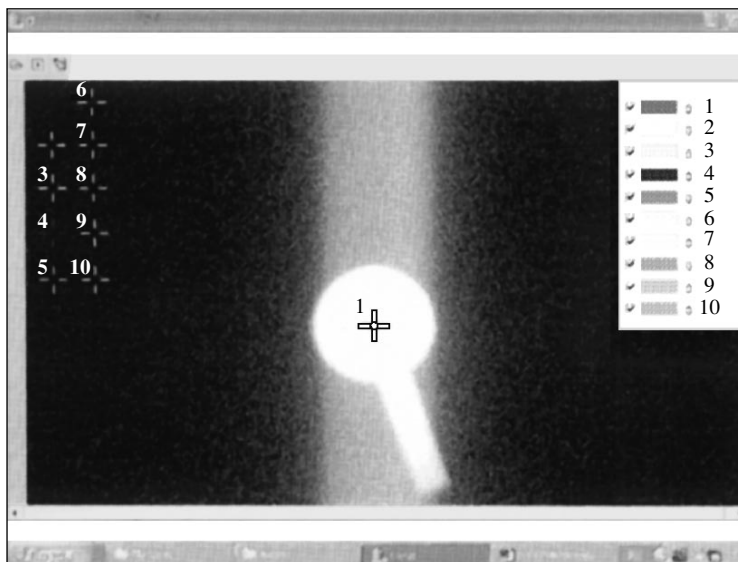
Fig. 1. Image of a SiC pyrometric probe in the flame of a microwelding device (longitudinal flow conditions; Parus program window).

T, K
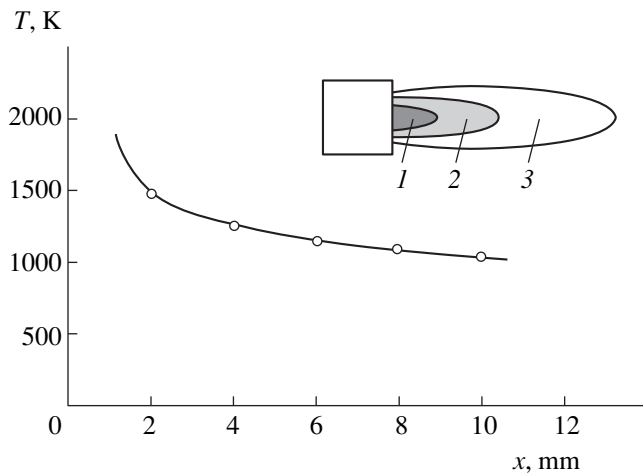
Fig. 2. Axial luminance temperature profile measured using a SiC pyrometric probe in the flame of a microwelding device: (*1*) core; (*2*) reduction zone; (*3*) flare.

The probes were imaged and their temperatures were measured by means of a TV pyrometric system of the Pyrotel-K type ($\lambda \cong 0.6$–0.72 μm) [9]. The system was computer-controlled using a specially developed Parus program package capable of providing simultaneous monitoring of a temperature field with up to ten probes. The reference thermal sensor was a thermocouple of the TKhA type [3].

Results and discussion. Preliminary calculations of the thermomechanical characteristics of the probes [10] allowed their design to be adapted to a particular range of gas flow velocities, mechanical loads, and thermal inertia. In particular, critical velocity values of the oncoming air flow producing fracture of the probes in the temperature range $T_{air} = 800$–$1600°C$ were determined for the probe with a round flat radiating pad with a radius of $d = 1$ mm mounted on a rectangular rod with dimensions $a \times b \times h = 0.6 \times 0.45 \times 5$ mm (see table).

Figure 1 gives an example of using a SiC pyrometric probe for temperature measurements in the flame of a gas-jet microwelding device. Figure 2 shows the typical axial temperature distribution in the flame. The results of our experiments showed that, in the range of "moderate" gas flow velocities ($v \leq 50$ m/s), the error of temperature measurements using the proposed SiC probes

did not exceed 5–7% and was determined for the most part by methodological factors related to the thermal conductivity (conductive heat transfer via probe mount) and radiative heat exchange (variation of the emissivity coefficient of the SiC surface). An important advantage of SiC probes is that the thermal conductivity of this material decreases with increasing temperature [11], which leads to a decrease in the conductive heat losses from the radiating pad.

Conclusions. The main results of this study are as follows:

(i) SiC devices of a new type—pyrometric probes were developed and experimentally tested;

(ii) critical values of the air flow velocity for the SiC probe fracture are determined;

(iii) the main factors of uncertainty for the temperature measurements with SiC probes in gas flows are classified.

Critical velocity of the air flow producing fracture of the SiC probe (radiating pad radius, $d = 1$ mm; rectangular rod base, $a \times b \times h = 0.6 \times 0.45 \times 5$ mm) at various temperatures

Working temperature, K	1073	1313	1873
Critical flow velocity, m/s	Longitudinal flow		
	585	650	390
	Transverse flow		
	390	430	260

REFERENCES

1. W. Hauf and U. Grigull, *Optical Methods in Heat Transfer* (Academic, New York, 1970).

2. M. L. Elder and J. D. Winefordner, Prog. Anal. At. Spectrosc. **6**, 293 (1983).

3. *Theoretical Foundations of Heat Engineering and Heat-Engineering Experiment: A Handbook*, Ed. by V. A. Grigor'ev and V. M. Zorin (Énergoatomizdat, Moscow, 1988), Vol. 2 [in Russian].

4. A. N. Gordov, *Principles of Pyrometry* (Metallurgiya, Moscow, 1971) [in Russian].

5. G. V. Samsonov and I. M. Vinitskii, *Handbook of Refractory Compounds* (Metallurgiya, Moscow, 1976; Plenum Press, New York, 1980).

6. A. V. Korlyakov, S. V. Kostromin, M. M. Kosyreva, *et al.*, Opt. Zh. **68** (12), 109 (2001).

7. O. G. Bazhenov and V. A. Karachinov, Pis'ma Zh. Tekh. Fiz. **22** (21), 26 (1996) [Tech. Phys. Lett. **22**, 875 (1996)].

8. V. A. Karachinov, RF Patent No. 2 189 664, Byull. Izobret., No. 26 (2002).

9. V. A. Karachinov, S. V. Il'in, S. B. Toritsin, *et al.*, in *Proceedings of the 6th International Conference on Crystals: Growth, Properties, Real Structure, and Applications* (VNIISIMS, Aleksandrov, 2003), pp. 91–92.

10. V. G. Zhilin, *Fiber-Optic Velocity and Pressure Transducers* (Énergoatomizdat, Moscow, 1987; Hemisphere, New York, 1990).

11. E. A. Burgemeister, W. Muench, and E. Pettenpaul, J. Appl. Phys. **50**, 5790 (1979).

Translated by P. Pozdeev

A Microscopic Model of Phase Transitions

V. A. Stepanov

Leipunskiĭ Institute of Physics and Power Engineering, State Scientific Center of the Russian Federation,
Obninsk, Russia
e-mail: stepanov@ippe.obninsk.ru
Received January 12, 2005

Abstract—A microscopic model of phase transitions in a lattice of interacting nodes, where each node is a statistical system with a certain internal structure, is proposed. The main parameter of the model is the configuration entropy related to the number of microscopic states in the node. The proposed model provides a consistent description of the first- and second-order phase transitions and reflects their distinctive features on the microscopic level. Equilibrium phase diagrams in the pressure versus temperature coordinates are constructed in the mean field approximation. © 2005 Pleiades Publishing, Inc.

An advantage of the microscopic models of phase transitions is the possibility of obtaining an explicit form of the nonequilibrium thermodynamic potential as a function of the order parameter $F(\eta)$, which can be used for analysis of a relationship between the microscopic parameters of a given system and the character of phase transitions in this system. The most thoroughly studied model of this kind is the Ising model, which considers a lattice of N nodes with two possible states of each node corresponding to the values $\mu = \pm 1/2$ of the magnetic (or electric) dipole moment. When the temperature decreases, such a lattice exhibits a second-order phase transition to a dipole-ordered state.

In various modifications of the Ising model, the dipole moments of the nodes in different states acquire the values $\mu = 0, \pm 1$ and the lattice energy is written as

$$E_N = -J\sum_{i,j}\mu_i\mu_j + \sum_i f(\mu_i), \qquad (1)$$

where J is the interaction energy. The second term is a positive definite quadratic function of μ_i, which describes the spectrum of energy states of the nodes [1–4]. In contrast to the simple Ising model, the models of type (1) are capable of describing both single- and two-phase regions in the phase diagrams. Such models provided an important step toward construction of a general microscopic model of the first- and second-order phase transitions. An analysis of these models shows that a rich set of possible phase states in the phase diagram can be expected if each interacting node in the lattice represents a system with a certain internal structure and the corresponding energy spectrum. On the other hand, a significant disadvantage of models (1) is their inability to describe completed phase transitions of both first and second order. At low temperatures, the phase diagram exhibits a two-phase domain featuring dipole-ordered and disordered states [4].

Further development of such microscopic models is based on the notion of a certain internal structure of the interacting nodes, which determines a set of microscopic states of the node for each value of the dipole moment μ (μ-state). Then, a phase transition—for example, of the first order—involves a change in the internal energy that is accompanied by a change in the entropy, which reflects a change in the probabilities of microscopic states on the passage from one phase to another. Variation of the number of ways in which a physical quantity related to the given phase transition is realized must be related to a change in the number of microscopic states of the node as a result of transitions between various μ-states.

Let us write an expression for the system energy with allowance for a change in the configuration entropy upon transitions between the states with $\mu = 0$, ± 1 in each node:

$$E_N = -J\sum_{i,j}\mu_i\mu_j - Ts\sum_i |\mu_i|, \qquad (2)$$

where s is the difference between the configuration entropies of the node in the states with $\mu = \pm 1$ and $\mu = 0$. By the node we imply either a single atom with variable magnetic moment or a group of atoms with the effective electric dipole or multipole moment μ corresponding to various configurations. The physical meaning of s is revealed by a comparison of expressions for the thermodynamic potential calculated in terms of the partition function (see, e.g., [5]) using the microkinetic approach (see, e.g., [6]).

In the mean field approximation, a nonequilibrium potential for Eq. (2) can be written as

$$F = \frac{qJ\eta^2}{2} - \frac{1}{\beta}\ln[1 + 2\exp(s)\cosh(qJ\eta\beta)], \qquad (3)$$
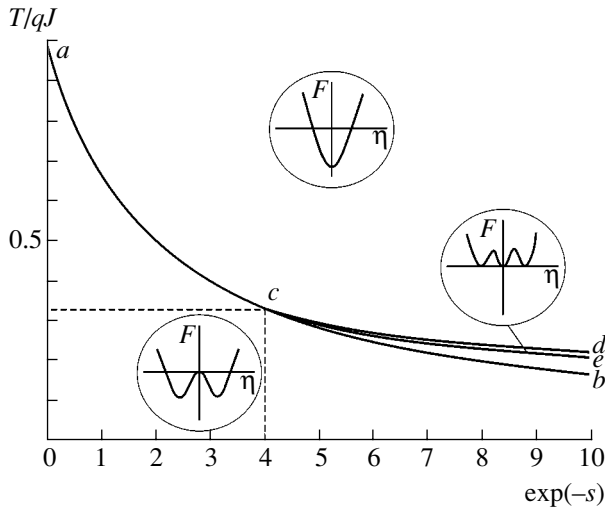
Fig. 1. Phase diagram constructed for the potential (3) in the T/qJ versus $\exp(-s)$ coordinates. The insets show the shape of the nonequilibrium potential in the corresponding regions.

where $\langle \mu_i \rangle = \eta$ and $\beta = T^{-1}$ is the inverse temperature in the energy units. In the microkinetic approach, the nonequilibrium potential in the mean field approximation is determined by the equation

$$\frac{1}{qJ}\frac{\partial F}{\partial \eta} = \eta - \sum_{\mu} \mu p_{\mu}, \qquad (4)$$

where p_{μ} is the probability for a given node to occur in the μ-state and q is the number of neighboring nodes. The probabilities of states for the nodes are determined by calculating the probabilities of transitions between states. For the transitions between states with $\mu = 0$ and ± 1, we have

$$\frac{1}{qJ}\frac{\partial F}{\partial \eta} = \eta - \frac{\dfrac{\nu(0,1)}{\nu(1,0)} - \dfrac{\nu(0,-1)}{\nu(-1,0)}}{1 + \dfrac{\nu(0,1)}{\nu(1,0)} + \dfrac{\nu(0,-1)}{\nu(-1,0)}}. \qquad (5)$$

The set of microscopic states for each state of a node with certain values of the dipole (multipole) moment μ corresponds to N_{μ} degenerate levels of the μ-state. Therefore, the relative probabilities (frequencies) of transitions depend both on the energy differences between the μ-states and on the numbers N_{μ} of levels in these states:

$$\frac{\nu(0,1)}{\nu(1,0)} = \frac{N_1}{N_0}\exp(-\beta E_1), \quad \frac{\nu(0,-1)}{\nu(-1,0)} = \frac{N_1}{N_0}\exp(-\beta E_{-1}). \qquad (6)$$

The values of energies for a node in the states $(1, 0, -1)$ in the applied mean field $(q\eta)$ are $E_1 = -qJ\eta$, $E_0 = 0$, and

$E_{-1} = qJ\eta$. Then, relations (5) and (6) yield

$$F = \frac{qJ\eta^2}{2} - \frac{1}{\beta}\ln\left[1 + 2\frac{N_1}{N_0}\cosh(qJ\eta\beta)\right], \qquad (7)$$

and the comparison with formula (3) gives $s = \ln(N_1/N_0)$.

Figure 1 shows a phase diagram calculated for nonequilibrium potential (3) in the T/qJ versus $\exp(-s)$ coordinates. According to this diagram, only a phase with $\eta \neq 0$ is stable below the boundary ab of the disordered phase ($\eta = 0$), whereas only the phase with $\eta = 0$ is stable above the acd curve. The dcb domain represents a two-phase state, in which the nonequilibrium potential exhibits two symmetric minima for $\eta \neq 0$ and one minimum for $\eta = 0$. The ce curve of the first-order phase transitions corresponds to equal F values in the minima. The critical point c has the coordinates $(4, 1/3)$, which are determined from the condition that the second and fourth derivatives of the nonequilibrium potential are zero for $\eta = 0$. As can be seen, the first-order phase transitions take place when the ratio of the number of realizations of the dipole-inactive state to the number of configurations of the dipole-active state (i.e., the entropy factor $\exp(-s)$) in the nodes is greater than four; otherwise, the system features the second-order phase transitions. Thus, the first-order phase transitions take place when a change in the configuration entropy upon transitions between states is greater than $\ln 4$.

The heat ΔH of the first-order phase transition is equal to the difference between average values of the entropy terms for the high- and low-symmetry phases in Eq. (2):

$$\Delta H = -\frac{Ts}{n}(\langle |\mu| \rangle_{\eta = \eta_0} - \langle |\mu| \rangle_{\eta = 0}), \qquad (8)$$

where n is the number of atoms in the node and the averaging of $|\mu|$ is performed at the nonsymmetric (for $\eta = \eta_0$) or symmetric (for $\eta = 0$) point of the phase transition. Expression (8) gives the following relation between the entropy factor and the heat of the first-order transition:

$$\frac{\Delta H}{T}n = r(s), \qquad (9)$$

where the function

$$r(s) = \ln(\exp(-s))$$
$$\times \left[\frac{2\cosh(qJ\eta_0\beta_0)}{\exp(-s) + 2\cosh(qJ\eta_0\beta_0)} - \frac{2}{\exp(-s) + 2}\right]$$

can be calculated by numerical methods. Evaluation of the entropy factor $\exp(-s)$ using relation (9) and the val-

ues of $\Delta H/T$ known for the structural phase transitions in solids gives values in the interval 4–4.5.

If the transitions from the states with $\mu = \pm 1$ to the state with $\mu = 0$ upon application of external pressure P are accompanied by a change ΔV in the volume of each node, the spectrum of states is $E_1 = -qJ\eta - P\Delta V$, $E_0 = 0$, and $E_{-1} = qJ\eta - P\Delta V$. Then, relations (5) and (6) yield the corresponding expression for the nonequilibrium potential:

$$F = \frac{qJ\eta^2}{2} - \frac{1}{\beta} \tag{10}$$
$$\times \ln[1 + 2\exp(s + P\Delta V\beta)\cosh(qJ\eta\beta)].$$

Figure 2 shows phase diagrams plotted for nonequilibrium potential (10) in the dimensionless coordinates of temperature (T/qJ) versus pressure ($p = P\Delta V/qJ$) for systems with different values of the entropy factor $\exp(-s)$. The diagrams are constructed for both positive and negative ΔV values. If the phase transition is accompanied by a positive volumetric effect, an increase in the pressure corresponds to the right-hand branch with $p > 0$. If the symmetric phase has a smaller volume, the pressure increment corresponds to the left-hand branch with $p < 0$. In Fig. 2, the region above the *acb* boundary corresponds to a symmetric phase with $\eta = 0$, while the region on the right of the curve 0*cb* corresponds to a low-symmetry phase with $\eta \neq 0$. The *ac*0 domain represents a two-phase state, and the critical point c (c', c'') has the coordinates $T/qJ = 1/3$, $p = (-s - \ln 4)/3$. For the first-order phase transitions with a positive volumetric effect, the transition temperature increases with growing pressure and, upon reaching the critical pressure $p_c = (-s - \ln 4)T_c/\Delta V$, the character of the transition changes from the first to second order. For systems featuring first-order transitions with negative volumetric effects (such as ice–water, graphite–diamond, etc.), the phase diagram exhibits no critical point, and the symmetric and low-symmetry phases at high pressures and low temperatures coexist. A change from the second-order phase transition ($\exp(-s) < 4$) to the first-order transition may take pace only in the case of a negative volumetric effect.
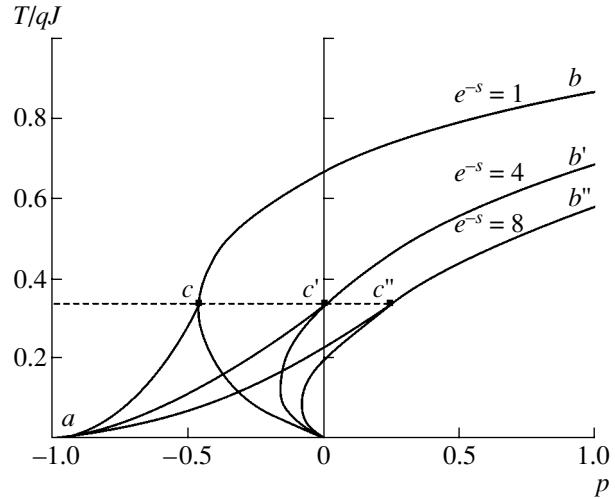
Fig. 2. Phase diagrams constructed for nonequilibrium potential (10) in the coordinates of dimensionless temperature (T/qJ) and pressure ($p = P\Delta V/qJ$) for systems with different values of the entropy factor $\exp(-s)$.

Nonequilibrium thermodynamic potential (10) corresponds to the energy

$$E_N = -J\sum_{i,j}\mu_i\mu_j - [P\Delta V + Ts]\sum_i |\mu_i|. \tag{11}$$

In this expression, each one of the interacting nodes is a statistical system whose states depend on the microscopic parameters (s and ΔV) and the external macroscopic parameters (pressure and temperature).

REFERENCES

1. H. W. Capel, Physica **32**, 966 (1966).
2. A. Benyoussef, T. Biaz, M. Saber, and M. Touzani, J. Phys. C **20**, 5349 (1987).
3. M. Blume, V. J. Emery, and B. Griffiths, Phys. Rev. A **4**, 1071 (1971).
4. O. A. Plaksin and V. A. Stepanov, Phase Trans. **40**, 105 (1992).
5. Yu. M. Gufan, *Structural Phase Transitions* (Nauka, Moscow, 1982) [in Russian].
6. H. E. Stanley, *Introduction to Phase Transitions and Critical Phenomena* (Clarendon Press, Oxford, 1971).

Translated by P. Pozdeev

Magnetic Anisotropy in the Films of Oriented Carbon Nanotubes Filled with Iron Nanoparticles

S. V. Komogortsev*, R. S. Iskhakov, E. A. Denisova, A. D. Balaev, V. G. Myagkov, N. V. Bulina, A. G. Kudashov, and A. V. Okotrub

Kirensky Institute of Physics, Siberian Division, Russian Academy of Sciences, Krasnoyarsk, 660036 Russia

Nikolaev Institute of Inorganic Chemistry, Siberian Division, Russian Academy of Sciences, Novosibirsk, 630090 Russia

* e-mail: komogor@iph.krasn.ru

Received December 14, 2004

Abstract—Films of carbon nanotubes oriented perpendicularly to the substrate surface and filled with iron nanoparticles have been synthesized and studied. Morphological features of these nanocomposite films lead to the appearance of an easy magnetization axis, which is perpendicular to the film plane. A method for enhancement of this effect is suggested and successfully tested. © *2005 Pleiades Publishing, Inc.*

Carbon nanotubes (CNTs) have received much attention due to a unique combination of electronic and magnetic properties. These properties make CNTs a highly promising material for the creation of a new generation of devices, such as emission tubes, nanotransistors, sources of spin-polarized electrons, planar displays, and for the development of hydrogen storage systems [1]. One of the most attractive applications of CNTs, which is directly related to their annular morphology and extremely high aspect ratio, is their use as nanodimensional containers for the second phase, in particular, a magnetically ordered one [2]. The introduction of magnetic phases in CNTs may lead to promising results in view of a significant shape anisotropy that must influence the encapsulated material. For example, this may provide for a better stabilization of the magnetic order (with respect to thermal fluctuations) as compared to that achieved in systems of equiaxial magnetic nanoparticles. Additional interest in such composite materials is related to the basic aspects of magnetic ordering in nearly one-dimensional nanostructures [3].

From the standpoint of practical applications, CNTs filled with a ferromagnetic phase are of interest as a media with a coercive force H_c exceeding theoretical predictions based on current knowledge about magneto-crystalline anisotropy ($H_c = 2K/M$) of bulk ferromagnetic materials. This possibility is related to the nanometer transverse dimensions of CNTs and to a significant influence of highly anisotropic interfaces on the magnetization processes. It is believed that the ability to control the magnetic anisotropy and coercivity of magnetic-phase-filled CNTs will lead to the development of new media for ultrahigh-density data recording, highly effective probes for magnetic force microscopes, and new recording heads [4].

This Letter reports the results of investigation of the magnetic anisotropy of a nanocomposite film comprising oriented CNTs filled with iron nanoparticles.
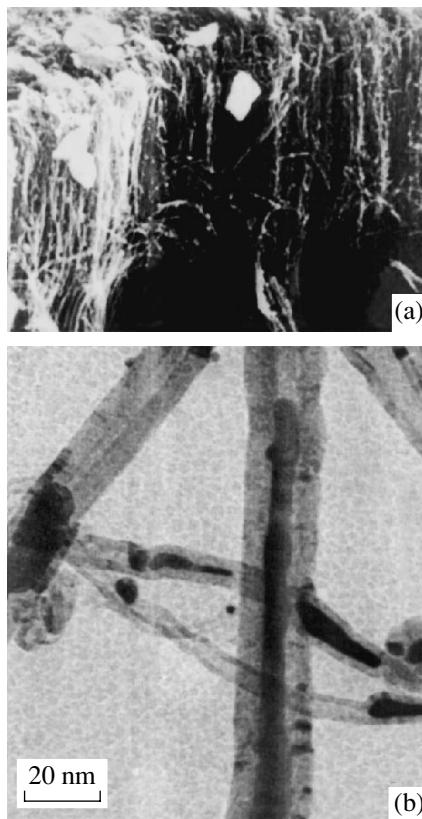
Fig. 1. (a) SEM image of a cleaved film composed of oriented CNTs; (b) TEM image of CNTs filled with Fe nanoparticles.

The films of oriented CNTs were obtained by thermolysis of a mixed vapor of C_{60} fullerene (a source of carbon) and ferrocene (a source of iron and the catalyst). A mixture of fullerene C_{60} and ferrocene (1 : 1) was placed into an alundum boat and transferred to a hot zone of the reactor. The duration of synthesis was 1 h. Upon cooling of the reactor, a dense black film was exfoliated from the inner surface of the quartz tube [5].

The thickness of exfoliated films was 10–15 μm. Examination by scanning electron microscopy (SEM) showed that the synthesized film comprises an agglomerate of nanotubes oriented parallel to each other, with a diameter of 10–20 nm and a length equal to or smaller than the film thickness (Fig. 1a). The SEM image of a cleaved section shows that the tubes are aligned predominantly perpendicularly to the substrate. Figure 1b presents an image obtained in the regime of transmission electron microscopy (TEM), from which it is seen that the inner cavities of CNTs are partly filled with iron (dark regions in the micrograph correspond to Fe particles and gray regions correspond to semitransparent graphite walls). Using the results of magnetization measurements, we determined the value of saturation magnetization and estimated the weight fraction of Fe atoms in the nanocomposite, which amounted to ~15–20%.

The macroscopic magnetic anisotropy of the obtained films was studied using a torque magnetometer. Figure 2 shows a plot of the torque versus the angle of the external magnetic field relative to the normal to the film surface. As can be seen from these data, the sample exhibits a pronounced uniaxial anisotropy, with the easy axis oriented perpendicularly to the film plane (that is, parallel to the direction of predominant orientation of CNTs). This anisotropy is apparently due to the anisotropy of Fe particles and the texture of nanotubes containing these particles.

The results of magnetization measurements using a vibrating sample magnetometer also provide information on the magnetic anisotropy in the system studied. However, the $M(H)$ curves of the nanocomposite films show only a weakly pronounced anisotropy with an easy axis perpendicular to the film surface (Fig. 3a). It was established that this result is explained by a nonideal texture and the lack of mechanical rigidity in the system of magnetic filaments. In order to enhance the texture and to impart rigidity to the agglomerate of CNTs filled with Fe nanoparticles, we fixed the orientation of nanotubes by placing the sample into a magnetic field oriented perpendicular to the film surface and impregnating the material with paraffin. Using this method, we obtained CNT film samples with a nonideal but well-pronounced magnetic anisotropy and the easy axis perpendicular to the film surface (Fig. 3b).

The energy of magnetic anisotropy was determined from the experimental magnetization curves and calcu-
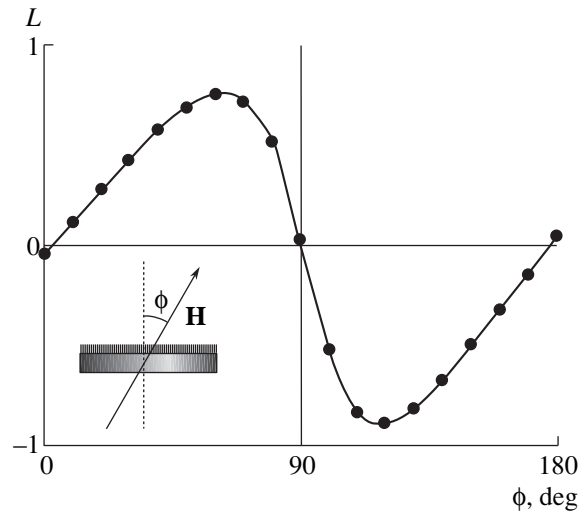

Fig. 2. A typical curve of the torque versus the angle of the external magnetic field relative to the normal to the film surface.
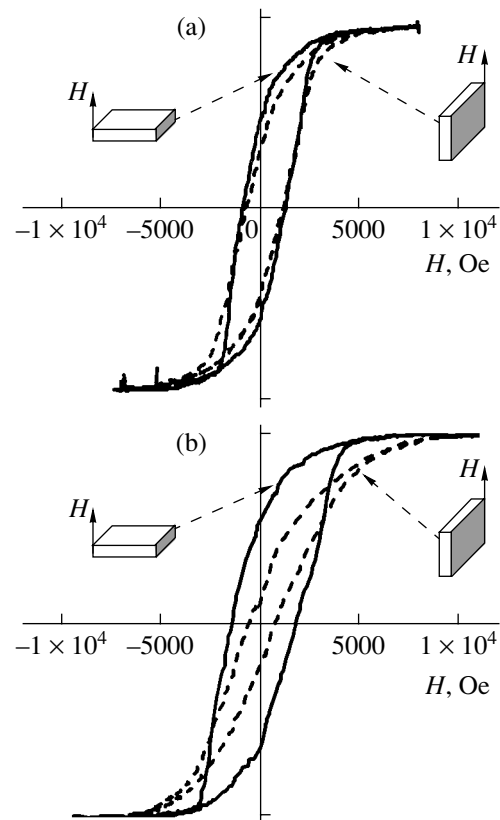

Fig. 3. Magnetization curves of a film composed of oriented CNTs filled with Fe nanoparticles, measured (a) in the initial state and (b) upon fixation of CNTs in a magnetic field of 3000 Oe.

lated using the formula

$$K_{\perp} = \int (M_{\perp}(H) - M_{\parallel}(H)) dH.$$

Some typical estimates are presented in the table. The

The energy of magnetic anisotropy of a film of CNTs filled with Fe nanoparticles

	Initial film	Film with CNTs fixed in magnetic field	
		500 Oe	3000 Oe
$K_\perp$, 10^6 erg/cm^3	0.9	1.6	2.8

maximum possible value of the energy of magnetic anisotropy for our nanocomposites modeled by cylindrical magnetic filaments can be evaluated as $\pi M_S^2 \sim 8 \times 10^6$ erg/cm^3. This implies that, by fixing the F-filled CNTs in a stronger magnetic field, we may provide for a threefold increase in the energy of magnetic anisotropy as compared to the maximum $K_\perp$ value achieved in our experiments. The nanocomposite film with the CNTs fixed in a field of 3000 Oe was also characterized by the energy of magnetic anisotropy determined from the $M_\perp(H)$ and $M_\parallel(H)$ curves measured at $T = 4.2$ K. The value of $K_\perp$ determined from these data was also equal to 2.8×10^6 erg/cm^3. The agreement of results obtained at room temperature and 4.2 K shows evidence for the same mechanism of magnetic anisotropy (shape anisotropy) and is indicative of an insignificant variation of the saturation magnetization of Fe nanoparticles in the entire temperature range from 4.2 to 300 K [3].

In order to evaluate a contribution due to the magnetocrystalline anisotropy to the observed macroscopic anisotropy, we measured the X-ray diffraction curves with and without the field. A comparison of the results of these measurements revealed no significant differences and showed the absence of a crystallographic texture. This implies that the crystallographic orientation of metal nanoparticles inside CNTs is virtually random and, on the average, is independent of the orientation of nanotubes. Therefore, the contribution due to the magnetocrystalline anisotropy is small compared to that due to the shape anisotropy of Fe nanoparticles contained inside the CNTs.

The coercive force of Fe particles reached 2000 Oe and 4.2 K and only slightly decreased (1800 Oe) upon increasing the temperature to 300 K. This result indicates that, despite small transverse dimensions of the CNTs, the blocking temperature T_B (corresponding to the ferromagnet–superparamagnet transition) for the Fe particles inside CNTs is significantly higher than room temperature. The simplest estimate of the blocking temperature is provided by the formula $T_B \sim VK/k_B$, where $V \sim d^2 l$ is the average volume of a nanoparticle, d is the average diameter of Fe filaments, l is their length, K is the energy of the local magnetic anisotropy, and k_B is the Boltzmann constant. In our samples, an increase in T_B is related to a considerable value of V achieved due to a large aspect ratio ($l \gg d$) of the Fe nanoparticles.

REFERENCES

1. C. Liu, Y. Y. Fan, M. Liu, *et al.*, Science **286**, 1127 (1999).

2. A. Bachtold, C. Strunk, J.-P. Salvetat, *et al.*, Nature **397**, 673 (1999).

3. R. S. Iskhakov, S. V. Komogortsev, A. D. Balaev, *et al.*, Pis'ma Zh. Éksp. Teor. Fiz. **78**, 271 (2003) [JETP Lett. **78**, 236 (2003)].

4. C. Prados, P. Crespo, J. M. Gonzalez, *et al.*, Phys. Rev. B **65**, 113405 (2002).

5. A. G. Kudashov, A. A. Pruss, O. G. Abrosimov, *et al.*, in *Proceedings of the Scientific Conference on Diamond Films and Films of Related Materials, Kharkov, 2002,* pp. 83–87.

Translated by P. Pozdeev

Atmospheric Pressure Volume Discharge
without External Preionization

I. D. Kostyrya[a], V. M. Orlovskiĭ[a], V. F. Tarasenko[a],*,
A. N. Tkachev[b], and S. I. Yakovlenko[b],**

[a] *Institute of High-Current Electronics, Siberian Division, Russian Academy of Sciences, Tomsk, Russia*
[b] *Institute of General Physics, Russian Academy of Sciences, Moscow, Russia*
e-mail: * vft@loi.hcei.tsc.ru; ** syakov@kapella.gpi.ru
Received January 12, 2005

Abstract—The phenomenon of electric breakdown in air at atmospheric pressure without additional preionization was studied by experimental and theoretical methods. Using voltage pulses of different polarity with subnanosecond leading front and nanosecond width, volume discharge can be obtained under such conditions between electrodes of various configurations, in particular, between two point electrodes. The development of an ionization wave in nitrogen is described within the framework of a diffusion-drift approximation in a spherical geometry. The fact that the qualitative character of discharge is independent of the voltage pulse polarity is explained by the multiplication of background electrons in the high-density gas. © *2005 Pleiades Publishing, Inc.*

Introduction. The volume electric discharge in high-density gases has been extensively studied by many research groups [1–6]. This interest is explained by the wide use of volume discharge, in particular, for pumping pulsed gas lasers [7]. Traditionally, much attention was devoted to the study of discharge in various gases at atmospheric pressure initiated by nanosecond voltage pulses [1, 2, 4, 5, 7] under the conditions of preionization in the discharge gap and with the initial voltage across the gap exceeding that in the quasi-stationary stage.

However, it was reported (see, e.g., review [6] and references therein) that a volume discharge in air and other gases at atmospheric pressure can also be obtained without preionization in the gap between a point cathode (electrode with a small radius of curvature) and a flat anode. Such a discharge was used for preionization in pulsed transverse discharge lasers [8].

Recently, it was pointed out [9] that the spreading of discharge in a high-density gas phase under certain conditions is determined by multiplication of the existing electrons at a low background density, rather than by the transport of electrons or photons. It was demonstrated that the intense multiplication of electrons takes place in prebreakdown fields in both electropositive and electronegative gases [9]. Such a prebreakdown multiplication can provide for a rather high density of background electrons, which is sufficient to consider the background a continuous medium for the multiplication wave propagation in the form of a streamer.

This mechanism of discharge development is independent of the electric field direction, which explains the volume discharge formation at a point anode, under conditions of a positive potential on the electrode. The study of ionization waves in a high-density gas is also important for elucidation of the mechanisms of streamer propagation and the high-power subnanosecond electron beam formation in gases at atmospheric pressure [6].

This Letter reports on the results of experimental and theoretical investigation of the conditions of a volume discharge formation in air at atmospheric pressure and the transition from volume to contracted discharge initiated by voltage pulses with subnanosecond leading front and nanosecond width.

Experimental. The experiments were performed using a nanosecond pulse generator of the ARINA X-ray setup [10], which produced voltage pulses with an amplitude of up to 150 kV (in the open-circuit regime). The voltage pulses had a full width at half maximum (FWHM) of several nanoseconds (depending on the load) at a leading front width below 1 ns. The generator was provided with a specially designed output insulator with an external diameter of 160 mm, which prevented continuous breakdown over the insulator surface in air even for a maximum cathode–anode distance of 67 mm. A cylindrical discharge chamber with an internal diameter of 160 mm, made of a 200-μm-thick copper foil, was connected to the generator with one edge and had a flat copper electrode on the opposite edge. In some experiments, the copper electrode had a 40-mm-diam hole closed with a 50-μm-thick AlBe foil. The side cylindrical wall of the chamber had a rectangular window 11 cm long and 5 cm wide. The potential electrode was in the form of a 40-mm-diam aluminum ball (electrode 1), a 6-mm-diam
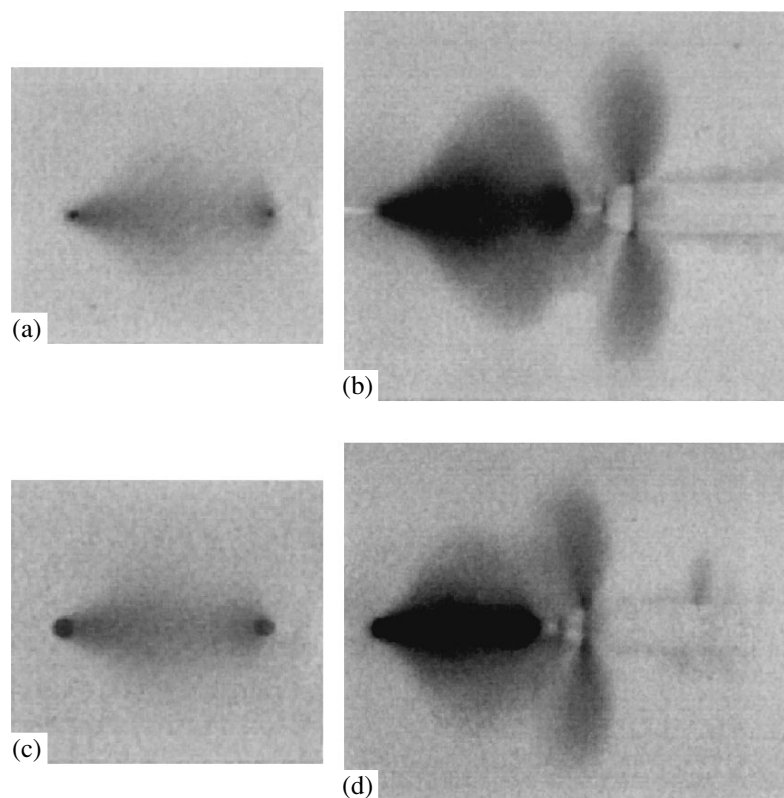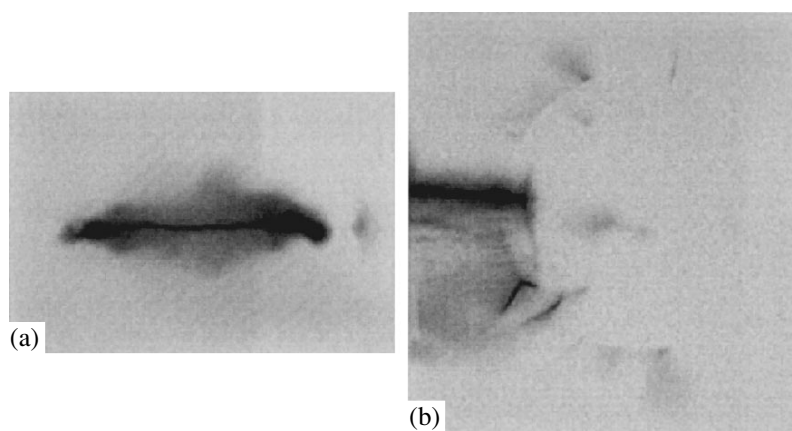
Fig. 1. Photographs of the volume discharge in air for (a, b) positive and (c, d) negative polarity of voltage pulses applied to the potential (right-hand) electrode. The experiments were performed at a gap width of 22 mm between two point electrodes of type 3, with the exposure to (a, c) one voltage pulse and (b, d) ten pulses.

tube made of a 50-μm-thick steel foil (electrode 2), or a point (electrode 3). The experiments were performed in air at atmospheric pressure (1 bar), with different polarities of applied voltage pulses, the interelectrode distance varying from 10 to 67 mm, and various shapes of the potential electrode (1–3). In addition, we have performed a series of experiments with discharge initiated between two point electrodes of type 3.

The integral pattern of discharge was photographed using a photocamera. The presence of X-ray radiation was detected by exposing an X-ray sensitive film of the RF-3 type, which was wrapped in a black paper and situated at the side window or behind the edge electrode with a hole.

Experimental results. Observations in the system described above gave the following results. For both possible voltage pulse polarities and potential electrodes of all types (1–3), a stable volume discharge was observed. Moreover, a stable discharge was formed as well in the case of two point electrodes of type 3 (Fig. 1). The volume discharge formation took place irrespective of the potential electrode polarity. However, X-ray radiation was detected only when a voltage of negative polarity was applied to the potential electrode.

For the appearance of a spark channel on the volume discharge background, it was necessary either to decrease the interelectrode distance or to increase the gas pressure. Figure 2a shows a photograph of the emission observed in air at 1 bar in a gap between two point electrodes spaced by 10 mm. As can be seen, there is a bright channel with slight bending on the volume (diffuse) discharge background. It should be noted that, in this system with a 10-mm gap, both a volume discharge (similar to that shown in Fig. 1 for a 22-mm gap) and a discharge with the bright channel (Fig. 2a) could be obtained. In the case of a ball electrode of type 1 with a 22-mm gap, the photographs revealed the formation of a growing (incomplete) channel. The channel appeared at the potential electrode and exhibited bending, sometimes at almost a right angle. The formation of a channel over the entire gap could be observed with a type-1 electrode when the gap width was reduced to 12 mm. Under such conditions, growing channels (leaders, covering only a part of the gap) were sometimes also observed (Fig. 2b). This behavior indicates that the application of nanosecond high-voltage pulses without preionization in the gap at atmospheric pressure leads initially to the formation of a volume discharge, which may exhibit subsequent contraction. The passage from volume to contracted discharge under the conditions

Fig. 2. Photographs of the volume discharge in air for (a) negative and (b) positive polarity of voltage pulses applied to the potential (right-hand) electrode. The experiments were performed at a gap width of (a) 10 mm between two point electrodes of type 3 and (b) 12 mm between a ball cathode of type 1 and a flat copper anode.

studied is probably explained by an increase in the specific energy deposited in the gas.

The results of the X-ray radiation detection on the photographic film showed that the radiation intensity was sufficient to produce a signal detectable during the action of several pulses only when voltage pulses of negative polarity were applied to electrodes 1–3. The maximum film blackening was observed on the side of the flat anode, which implies that the X-ray radiation is generated as a result of runaway electron bremsstrahlung at the anode. The maximum intensity was obtained with a ball cathode of type 1. On the films placed behind the flat electrode with an AlBe film, the maximum film blackening was also observed with electrode 1, and the minimum, with a point cathode of type 3. In these experiments, X-ray radiation was also detected only with the negative voltage pulse polarity on the potential electrode. For the positive polarity, X-rays were not detected even when the exposure (i.e., the number of pulses) was increased by one order of magnitude.

We believe that the main factors responsible for the volume discharge formation under the experimental conditions studied (i.e., with voltage pulses of large amplitude, nanosecond duration, and subnanosecond leading front) are (i) the appearance of fast electrons producing spontaneous preionization in the discharge gap and (ii) the intense multiplication of electrons in the regions of high electric field strength. Here, by "fast" electrons, we imply those with energies of several kiloelectronvolts, while the term "runaway" electrons refers to particles possessing energies of a few tens of kiloelectronvolts and above, although both types are essentially runaway electrons.

It is also necessary to emphasize a difference in the features of volume discharge formation upon alteration of the polarity of applied voltage pulses, which is manifested by the presence of a high-intensity X-ray radiation in the case of negative pulses applied to the potential electrode. Based on this result, we may suggest that the main reason for the volume discharge formation in the case of positive pulses with a short leading front applied to the potential electrode is the multiplication of background electrons appearing both due to the natural background of radioactivity and cosmic rays and due to incomplete (crown and surface) discharges in the experimental camber. When negative pulses are applied to the potential electrode, an important factor determining the volume discharge formation and especially the velocity of the ionization wave propagation is also played by fast electrons formed due to the electric field enhancement both at the anode and in the interelectrode gap [6].

Analysis of experimental results. In order to consider the electron multiplication wave, we have developed a one-dimensional diffusion-drift model, which provides a qualitative description of the ionization process within a spherical sector in the gas (nitrogen).

According to this model, we consider a plasma generated in the gap between spherical electrodes with $r_0 = 0.05$ cm $< r < r_1 = 3$ cm (r_0 and r_1 are the radii of the inner and outer electrodes, respectively). The process of plasma formation and the electric field screening were described in terms of the equation of momentum transfer, the electron and ion equations of continuity, and the Poisson equation for the electric field. Various quantities entering into equations of the diffusion-drift model (ionization frequencies, drift velocities, diffusion coefficients) were set as functions of the electric field strength using the published data [6, 11]. The voltage between electrodes was set as a function of time. Below, we present the results of solving these equations for a voltage linearly increasing over $t = 0.7$ ns to $U = 150$ kV and then remaining constant. The background was characterized by a small initial electron density of $N_0 = 10^6$ cm^{-3}.

The results of calculations showed that the main role in the plasma propagation is played by the background electron multiplication rather than by electron transport. The plasma starts rapidly moving toward the anode when the interelectrode voltage increases to $U \sim 50$ kV. The electron multiplication wave velocity becomes as high as 3×10^9 cm/s for $U = 150$ kV at $t \approx 1$ ns, when the plasma approaches the anode. This value agrees with a simple formula for the ionization wave propagation velocity recently obtained in [9] (see also reviews [6, 11]):

$$v = \frac{v_i r_0}{\zeta(E_0/p)},$$

$$\zeta(E_0/p) = 2\mathrm{Ln}\left(\frac{d\ln(u_{\mathrm{de}}(E/p)\xi(E/p))}{d\ln(E/p)}\right)_{E/p = E_0/p}.$$

(1)

Here, v_i is the ionization rate, $E_0 = E(z(0))$ is the electric field strength at the front surface, r_0 is the radius of a spherical surface approximating the front, p is the neutral gas pressure, $\mathrm{Ln} \equiv \ln(N_{\mathrm{cr}}/N_0)$, N_0 is the background plasma density, and N_{cr} is the critical plasma density corresponding to complete screening of the electric field. In relation (1), the ionization rate $v_i = \alpha_i u_{\mathrm{de}}$ is expressed as a product of the Townsend coefficient $\alpha_i(E, p) = p\xi(E/p)$ and the electron drift velocity $u_{\mathrm{de}}(E/p)$ ($\xi(E/p)$ is a function characteristic of a given gas).

The results of preliminary calculations give $E_0 \approx 150$ kV/cm, $E_0/p \approx 200$ V/(cm Torr), $r_0 \approx 1.5$ cm, and $N_{\mathrm{cr}} \approx 10^{13}$ cm^{-3}. Using data from [6, 11], we obtain $v_i \approx 1.4 \times 10^{11}$ s^{-1} and $\zeta \approx 75$. Then, according to formula (1), the ionization wave velocity under the conditions studied is $v \approx 3 \times 10^9$ cm/s.

Thus, if the field strength in the gas volume is sufficiently high, electrons exhibit rapid multiplication leading to a delay in the spark channel formation. Naturally, this field has to be created at a sufficiently high rate, such that no spark breakdown could take place during the field buildup time (in other words, the voltage pulse applied to the electrodes must have a steep leading front).

Conclusion. A volume electric discharge in air at atmospheric pressure can be generated without external preionization by voltage pulses with subnanosecond leading front and nanosecond width, irrespective of the potential electrode polarity. At a fixed voltage pulse duration, the contraction of the discharge is observed on decreasing the interelectrode gap width and increasing the gas pressure. Apparently, an increase in both the field strength and the gas density imposes higher requirements on the pulse front steepness necessary before the formation of a homogeneous discharge. At a given front width and FWHM of the voltage pulse, spark channels form beginning with a certain gas density (pressure) and applied field strength.

There are grounds to believe that a wave of background electron multiplication arises under the experimental conditions studied, since the character of such a waver is independent of the field direction and the discharge character remains qualitatively the same upon changing voltage polarity of the electrodes.

REFERENCES

1. G. A. Mesyats, Yu. I. Bychkov, and V. V. Kremnev, Usp. Fiz. Nauk **107**, 201 (1972) [Sov. Phys. Usp. **15**, 882 (1972)].

2. Yu. D. Korolev and G. A. Mesyats, *The Physics of Pulse Breakdown in Gases* (Nauka, Moscow, 1991) [in Russian].

3. L. P. Babich, T. V. Loiko, and V. A. Tsukerman, Usp. Fiz. Nauk **160** (7), 49 (1990) [Sov. Phys. Usp. **33**, 521 (1990)].

4. Yu. P. Raizer, *Gas Discharge Physics* (Nauka, Moscow, 1992; Springer-Verlag, Berlin, 1991).

5. V. V. Osipov, Usp. Fiz. Nauk **170**, 225 (2000) [Phys. Usp. **43**, 221 (2000)].

6. V. F. Tarasenko and S. I. Yakovlenko, Usp. Fiz. Nauk **174**, 953 (2004) [Phys. Usp. **47**, 887 (2004)].

7. G. A. Mesyats, V. V. Osipov, and V. F. Tarasenko, *Pulsed Gas Lasers* (Nauka, Moscow, 1991; SPIE Opt. Eng. Press, Bellingham, 1995).

8. A. I. Pavlovskiǐ, V. S. Bosamykin, V. I. Karelin, and V. S. Nikol'skiǐ, Kvantovaya Élektron. (Moscow) **3**, 601 (1976).

9. S. I. Yakovlenko, Pis'ma Zh. Tekh. Fiz. **30** (9), 12 (2004) [Tech. Phys. Lett. **30**, 354 (2004)].

10. G. A. Mesyats, *Pulsed Power Engineering and Electronics* (Nauka, Moscow, 2004; Kluwer, Boston, 2004).

11. A. N. Tkachev and S. I. Yakovlenko, Central European Journal of Physics (CEJP) **2**, 579 (2004); www.cesj.com/physics.html.

Translated by P. Pozdeev

Effect of Thickness on the Properties of FeAlN Films

A. S. Kamzin[a,*], F. Wei[b], Z. Yang[b], and S. A. Kamzin[a]

[a] *Ioffe Physicotechnical Institute, Russian Academy of Sciences, St. Petersburg, 194021 Russia*
[b] *Research Institute of Magnetic Materials, Lanzhou University, Lanzhou, 230000 China*
* e-mail: Kamzin@mail.ioffe.ru
Received December 27, 2004

Abstract—The magnetic properties, microstructure, and morphology of thin nanocrystalline FeAlN films synthesized by RF magnetron sputtering were studied as dependent on the film thickness. The best soft magnetic properties were observed for the films with thicknesses above 800 nm. These films consist predominantly of nanocrystalline α-Fe particles with an average size of ~15 nm and are characterized by crystal lattice expansion in the (110) plane approaching a critical level of 0.28%. FeAlN films with a thickness of 1000 nm are characterized by $\mu_1 \sim 2000$. © 2005 Pleiades Publishing, Inc.

The interest in studying FeN alloys arose upon the discovery [1] that the saturation magnetization of polycrystalline FeN films is higher than that of iron. Subsequent investigations showed that nanostructured thin films of the FeXN system (X = Ta, Hf, Nb, Zr, Si, Al) not only exhibit high values of the saturation magnetization but also possess other properties meeting requirements of soft magnetic materials used for manufacturing thin-film magnetic heads, magnet cores, etc. (see, e.g., [2–5] and references therein). The development of such materials has been stimulated by increasing requirements on the devices for high-density data writing and recording.

The main research effort was directed at the study of magnetic properties of FeXN films depending on the density of N and X atoms and the regime of synthesis. However, the film thickness is also an important parameter significantly influencing the properties of such materials. Unfortunately, data on the dependence of the properties of soft magnetic properties of FeXN films on their thickness have not been reported so far.

This Letter presents the results of our experimental investigation of the effect of thickness on the microstructure and magnetic properties of FeAlN films synthesized by RF magnetron sputtering on glass and (111)-oriented single crystal silicon substrates. The nanocrystalline structure and soft magnetic properties of FeAlN films were obtained by annealing the deposited samples for 1 h at 400°C in a vacuum furnace at a residual pressure of 5×10^{-5} Torr.

The soft magnetic properties of nanocrystalline FeAlN films are determined by N atoms, which modify the crystal lattice of α-Fe and decrease the grain size in the synthesized polycrystalline film. The chemical activity of N atoms in FeXN films significantly depends on the third element (X), in particular, on the probability of formation of a chemical compound between N and X (i.e., on their positions in the periodic table) [6].

The choice of X = Al in our case was determined by the fact that aluminum is capable of quite readily interacting with nitrogen [7], with the formation of aluminum nitrides leading to a decrease in the saturation induction B_S of the final alloys. For this reason, the content of Al atoms in the films has to be thoroughly controlled so as to avoid the formation of nonmagnetic compounds of aluminum and nitrogen [8].

In our experiments, the strict dosage of Al atoms in the films synthesized by RF sputtering was achieved by using a composite target. The target comprised a plate of pure iron partly covered by a foil made of pure aluminum. The relative content of Al atoms in the films could be controlled by varying the area of the iron plate masked by the aluminum foil. It was established [9] that sputtering of a target with 5% of the iron surface masked by aluminum gave FeAlN deposits with a 2.5% atomic fraction of aluminum. The experiments showed this very amount of aluminum to impart good soft magnetic properties to the films [9].

The content of N atoms in the synthesized films was controlled by varying the partial pressure $P(N_2)$ of nitrogen in the chamber during sputtering ($P(N_2)$ is the ratio of the pressure of nitrogen to the total pressure in the gas phase). The optimum conditions for the RF sputter deposition of desired FeAlN films were as follows: background pressure, 2×10^{-7} Torr; pressure during sputtering, 2×10^{-3} Torr; partial pressure of nitrogen, 3%; sputtering power density, 2.3 W/cm^2; substrate temperature, 20–220°C; film deposition rate, 20–30 nm/min.

The content of Fe and Al atoms in the synthesized films was determined by energy-dispersive X-ray spectroscopy. The saturation magnetization B_S and the coercive force H_C were measured using a highly sensitive vibrating sample magnetometer and a magnetic-flux meter, respectively. The crystal and magnetic phase
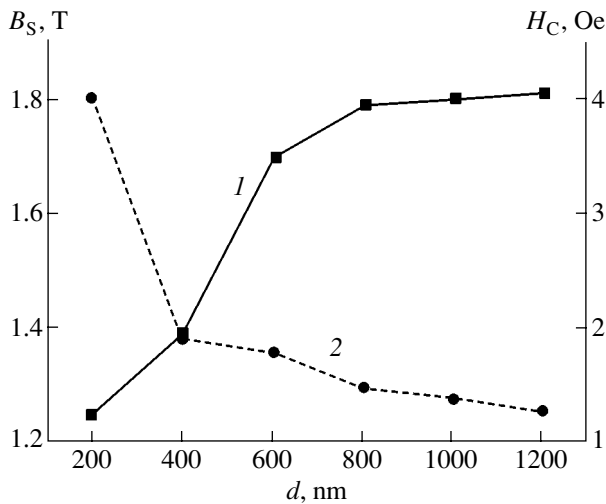
Fig. 1. Experimental plots of the (*1*) saturation magnetization B_S and (*2*) coercive force H_C versus thickness d of the synthesized FeAlN films deposited at $P(N_2) = 5\%$.
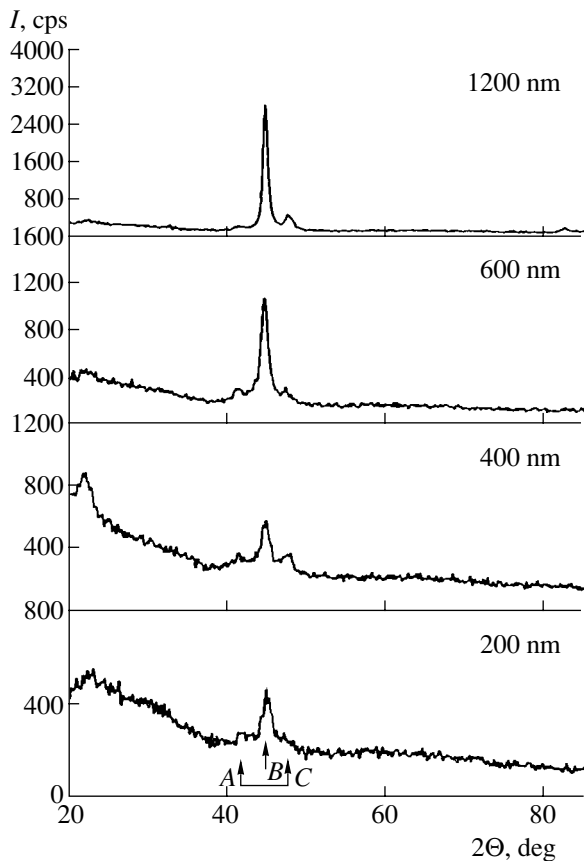
Fig. 2. X-ray diffractograms of FeAlN films of various thicknesses. The arrows *A*, *B*, and *C* indicate the diffraction lines corresponding to γ-Fe$_4$N(111), α-Fe(110), and γ-Fe$_4$N(200) phases, respectively.

analyses were performed using X-ray diffraction and the Mössbauer conversion electron spectroscopy techniques, respectively. The surface morphology of the films was examined on an atomic force microscope.

Figure 1 shows the experimental plots of the saturation magnetization B_S and the coercive force H_C versus thickness d of the synthesized FeAlN films. As can be seen from these data, B_S first monotonically increases with the film thickness and, then (at $d \sim 1000$ nm), exhibits saturation. As is known, the magnetic properties of materials are closely related to their structure. For this reason, we have studied variations of the structure of FaAlN deposits with the film thickness.

Figure 2 presents the typical X-ray diffraction patterns of the synthesized FeAlN film with various thicknesses. As can be seen, the diffractograms exhibit three lines corresponding to α-Fe(110), γ-Fe$_4$N(111), and γ-Fe$_4$N(200) phases, with the relative intensities dependent on the film thickness. As the film thickness grows, the content of α-Fe increases. This may account for the observed increase in B_S for the films with thicknesses increasing up to 600 μm. However, further increase in the film thickness does not lead to additional growth in B_S. The variation of H_C is opposite to that of B_S. While the intensity of a line corresponding to α-Fe(110) increases, the width of this line varies rather insignificantly. This implies that the average size of α-Fe grains in the films does not significantly vary with the film thickness and remains shorter than the characteristic length of the ferromagnetic exchange interaction between these particles.

Thus, thicker films contain a greater amount of α-Fe grains exhibiting ferromagnetic correlation. This leads to a decrease in H_C, since an increase in the number of such grains leads to a stronger exchange coupling and, hence, weaker effective magnetocrystalline anisotropy. In addition, an increase in the film thickness is accompanied by a slight decrease in the width of the α-Fe(110) line. It can be suggested that a longer sputtering time leads to heating of the substrate and improves the conditions of crystallization. As a result, more perfect α-Fe grains are crystallized and the level of residual stresses decreases. These factors also favor a decrease in the coercivity of thicker films.

Figure 3 shows the Mössbauer spectra of FeAlN films of various thicknesses measured in the backscattering mode with the detection of conversion and Auger electrons. An analysis showed that the spectra of 600-nm-thick films (Fig. 3a) exhibit several Zeeman sextuplets, quadrupole-splitting doublets, and a single line at the zero Doppler velocity of the Mössbauer source. The hyperfine splitting parameters of the Zeeman component with the maximum line intensity correspond to an effective magnetic field on Fe nuclei of 326 ± 5 Oe and a zero quadrupole splitting. This component is assigned to α-Fe. The linewidths in this sextuplet reach ~1 mm/s, which indicates that the α-Fe phase contributes to the Mössbauer spectrum with a set of sextuplets with the effective magnetic fields indicated above. This pattern is observed when the α-Fe phase is formed by a system of nanodimensional particles. The other components (Zeeman sextuplets with
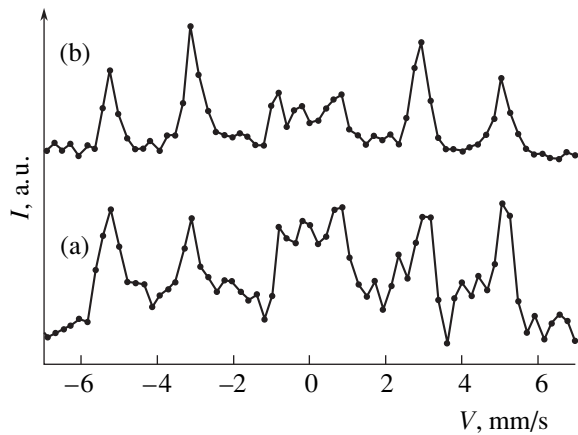
Fig. 3. The Mössbauer conversion electron spectroscopy spectra of FeAlN films with thicknesses (a) 600 and (b) 1000 nm deposited at $P(N_2) = 3\%$.

lines of low intensity, quadrupole-splitting doublets, and the single line at $V = 0$) represent the contributions from magnetic and nonmagnetic FeN compounds (e.g., γ-Fe$_4$N)].

The Mössbauer spectrum of a 1000-nm-thick FeAlN film (Fig. 3b) consists of two components: a Zeeman sextuplet and a single line at the zero Doppler velocity. The narrow linewidth in the sextuplet (below 1 mm/s) indicates that the Zeeman component represents the α-Fe phase composed of nanoparticles with dimensions of about 10–15 nm. The relative areas under lines in the Zeeman sextuplet are 3 : 4 : 1 : 1 : 4 : 3, which is evidence that the magnetic moments of Fe ions in the α-Fe particles forming this film are oriented perpendicularly to the wavevector of γ radiation (which is directed along the normal to the film surface). Thus, the magnetic moments of Fe ions occur in the film plane. The line of small intensity observed in the region of zero velocity is indicative of the presence of a certain amount of iron in the paramagnetic state.

Conclusions. Experimental data on the dependence of the magnetic properties of FeAlN films on their thickness are obtained. It is established that the best soft magnetic properties (i.e., the maximum saturation magnetization and the minimum coercive force) are exhibited by the films with thicknesses above 800 nm. The films with thicknesses below 800 nm are multiphase, while thicker films consist predominantly of nanocrystalline α-Fe grains with an average size (~15 nm) below the characteristic length of the ferromagnetic exchange interaction between these particles (~35 nm [10]). As a result, the strong ferromagnetic exchange interaction between α-Fe grains leads to a decrease in the local magnetocrystalline anisotropy [6]. The crystal lattice expansion in the (110) plane approaches a critical level of 0.28%, which also leads to the formation of FeAlN films with good soft magnetic properties [11]. The FeAlN films with a thickness of 1000 nm are characterized by rather high values of the parameter μ_i (~2000).

REFERENCES

1. M. Takahashi, I. Hatakeyama, and T. K. Kim, Czech. J. Phys. B **21**, 574 (1971).
2. K. H. Kim, Y. H. Kim, J. Kim, *et al.*, J. Magn. Magn. Mater. **215**–**216**, 368 (2000).
3. D. Zheng, Y. Ma, D. Wu, *et al.*, Phys. Status Solidi A **193**, 61 (2002).
4. Y. Ma, X. Li, T. Xie, *et al.*, Mater. Sci. Eng. **103**, 233 (2003).
5. A. S. Kamzin, F. Wei, Z. Yang, and S. A. Kamzin, Fiz. Tverd. Tela (St. Petersburg) **47**, 493 (2005) [Phys. Solid State **47**, 508 (2005)].
6. B. Viala, M. K. Minor, and J. A. Barnard, J. Appl. Phys. **80**, 3941 (1996).
7. R. D. Pehlke and F. Elliott, Trans. AIME **218**, 1088 (1960).
8. D. J. Rogers, S. Wang, D. E. Laoghlin, and M. H. Kryder, IEEE Trans. Magn. **28**, 2419 (1992).
9. T. Xie, D. Zheng, X. Li, *et al.*, Chin. Phys. **11**, 725 (2002).
10. J. F. Löffher, H. B. Braun, W. Wanger, *et al.*, Mater. Sci. Eng., A **304**–**306**, 1050 (2001).
11. M. Takahashi, T. Shimatsu, and H. Shoji, Proc. ICF **6**, 1483 (1992).

Translated by P. Pozdeev

"Nanotube": Scanning Microscope Probe
as a Controlled Source of Microwave Radiation

G. V. Dedkov* and A. A. Kyasov

Kabardino-Balkarian State University, Nalchik, Kabardino-Balkaria, Russia
** e-mail: gv_dedkov@mail.ru*
Received January 19, 2005

Abstract—A nanoparticle (scanning microscope probe) can be effectively heated by equilibrium thermal radiation in a vacuum chamber. The particle also can re-radiate energy via near-field modes to the sample surface. A possible design of an oscillating source of microwave radiation ("nanotube") based on these phenomena is considered. © *2005 Pleiades Publishing, Inc.*

In recent years, considerable progress has been observed in nanoelectrodynamics and nanooptics—the fields of physics studying the propagation of electromagnetic waves in nanodimensional structures [1–6] and the near field effects at a heated solid surface [3, 6–11]. In particular, it was established that a nanoparticle occurring in the surface near-field zone is capable of effectively absorbing and emitting energy in the form of nonradiative electromagnetic modes [3, 6, 7, 11]. This phenomenon is employed in scanning near field optical microscopy, whereby laser energy is supplied to the sample surface via an optical fiber with an output aperture significantly smaller than the pumping radiation wavelength.

An important distinctive feature of the microwave radiation, which is related to the near field structure, is the dependence of the emissivity and absorptivity of a nanoprobe on the dielectric characteristics of the solid surface [3, 6, 7, 11]. This behavior differs from that of the radiation characteristics of a heated macroscopic body (blackbody radiation) in the far field zone, where the radiation power is determined by the universal Stefan's law. Another important difference is the dependence of the radiation power on the shape and size of the nanoprobe, the distance from the surface, and the direction of motion [8, 9]. In particular, it was demonstrated that an intense heat flux between such a scanning probe and a sample takes place even at a small (<1 K) difference in their temperatures [9]. Correct calculation of the rates of heat exchange between the probe (and its holder) and the vacuum background, as well as between the probe and the sample surface, is very important in applications. In this context, it is necessary to study the possibility of providing and controlling the necessary temperature difference and to determine the reserve of thermal energy (power) for such a radiation source ("nanotube").

A spherical particle (nanoprobe) of radius R has the thermal energy $\Delta Q = \dfrac{4\pi}{3} R^3 \rho C_p \Delta T$, where ρ and C_p are the density and heat capacity of the material. For example, a silicon particle with $R = 20$ nm ($\rho = 2300$ kg/m^3 and $C_p = 700$ J/(kg K) at $T = 273$ K) at a temperature difference of $\Delta T = 1$ K possesses an excess energy of about 340 eV. This energy can be transferred to the surface via electromagnetic near field modes of the scanning probe performing harmonic oscillations. A schematic diagram of the proposed device is presented in Fig. 1. Over most of the oscillation period, the moving probe occurs in the zone of equilibrium radiation with increased temperature $T + \Delta T$ and restores the energy reserve. The accumulated energy is radiated within the short period of time when the probe occurs in close constant with a surface possessing energy T. In the case of rapid oscillations, heat exchange in the probe–holder contact can be ignored [9] and, hence, the time of thermal relaxation is determined only by the processes of the probe heating due to equilibrium thermal back-
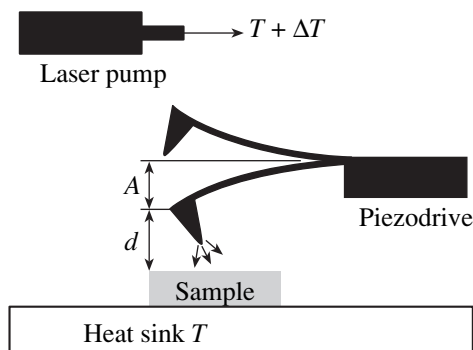
Fig. 1. Schematic diagram of the microwave "nanotube." The background temperature is controlled by microwave laser radiation.

ground radiation and the probe cooling due to energy transfer to the surface. It should be emphasized that we are speaking of the near-field (contactless) heat exchange between the probe and the sample surface. The heat exchange between the probe and the background radiation (see formula (1) below) is also mediated by the near field modes.

According to our recent theory [10], the rate of heating (cooling) of a small spherical particle having a temperature T_1 and exposed to a homogeneous background radiation with a temperature T_2 is

$$\dot{Q}_h = -\frac{4\hbar}{\pi c^3}\int_0^\infty d\omega\,\omega^4\alpha''(\omega)(\Pi(\omega, T_1) - \Pi(\omega, T_2)),$$

$$\Pi(\omega, T) = \left(\exp\frac{\hbar\omega}{k_B T} - 1\right)^{-1},$$

(1)

where $\alpha''(\omega)$ is the imaginary part of the complex polarizability of the particle, $\hbar$ is the Planck constant, c is the velocity of light in vacuum, and k_B is the Boltzmann constant. Formula (1) was obtained under the assumption that $\left(\frac{k_B R}{2\pi\hbar c}\right)\max(T_1, T_2) \ll 1$. At the same time, the rate of heating (cooling) of a particle near the flat surface of an absorbing dielectric medium can be expressed as [8, 11]

$$\dot{Q}_c$$
$$= -\frac{\hbar}{\pi z_0^3}\int_0^\infty d\omega\,\omega\alpha''(\omega)\Delta''(\omega)(\Pi(\omega, T_1) - \Pi(\omega, T_2)),$$

(2)

where z_0 is the distance from the surface, $\Delta''(\omega)$ is the imaginary part of the complex function $\Delta(\omega) = (\varepsilon(\omega) - 1)/(\varepsilon(\omega) + 1)$, and $\varepsilon(\omega)$ is the dynamic permittivity of the surface. Note that formula (2) takes into account only the contribution due to nonradiative electromagnetic modes, which is predominant for z_0 in the nanometer range.

Let us assume that the particle and surface materials are described by the same dielectric function of the type described in [6], with the characteristic parameters ω_T and γ_T (the frequency and the damping constant of optical phonons, respectively) and the permittivities ε_0 and ε_∞ (for $\omega = 0$ and the optical frequencies, respectively). It should be noted that use of a high-conductivity material in the range of normal temperatures is ineffective. Taking into account that, for a spherical particle of radius R, $\alpha(\omega) = R^3(\varepsilon(\omega) - 1)/(\varepsilon(\omega) + 2)$ and using

formulas (1) and (2), we obtain expressions for the heating and cooling rates,

$$\dot{Q}_h = \frac{3}{\pi}\left(\frac{R\omega_T}{c}\right)^3(k_B\Delta T\omega_T)\frac{\tilde{\gamma}(\varepsilon_0 - \varepsilon_\infty)}{(\varepsilon_\infty + 2)^2}f_1(\beta, q, \tilde{\gamma}), \quad (3)$$

$$\dot{Q}_c = -\frac{3}{2\pi}\left(\frac{R}{z_0}\right)^3(k_B\Delta T\omega_T)$$

$$\times \frac{\tilde{\gamma}^2(\varepsilon_0 - \varepsilon_\infty)^2}{(\varepsilon_\infty + 2)^2(\varepsilon_\infty + 1)^2}f_2(\beta, p, q, \tilde{\gamma}),$$

(4)

$$f_1(\beta, q, \tilde{\gamma}) = \beta^2\int_0^\infty\frac{x^6 dx}{\sinh(\beta x/2)^2}\frac{1}{[(q - x^2)^2 + \tilde{\gamma}^2 x^2]}, \quad (5)$$

$$f_2(\beta, p, q, \tilde{\gamma}) = \beta^2\int_0^\infty\frac{x^4 dx}{\sinh(\beta x/2)^2}$$

$$\times\frac{1}{[(p - x^2)^2 + \tilde{\gamma}^2 x^2][(q - x^2)^2 + \tilde{\gamma}^2 x^2]},$$

(6)

where

$$\beta = \frac{\hbar\omega_T}{k_B T}, \quad \tilde{\gamma} = \frac{\gamma_T}{\omega_T}, \quad p = \frac{\varepsilon_0 + 1}{\varepsilon_\infty + 1}, \quad q = \frac{\varepsilon_0 + 2}{\varepsilon_\infty + 2}.$$

For a scanning microscope probe having the shape of a paraboloid of revolution with a radius R and a height H, the corresponding expressions are obtained from formulas (3) and (4) upon the substitutions $R^3 \longrightarrow 3RH^2/4$ and $R^3/z_0^3 \longrightarrow (3/4)RH^2/z_0(H + z_0)^2$, where z_0 is the distance from the probe apex to the surface. Let f and A be the frequency and amplitude of oscillations of such a parabolic nanoprobe, respectively, and d be the distance from the surface to the probe apex in the neutral position. Representing the probe heat capacity as $C = \pi RH^2\rho C_p$ and introducing the dimensionless time $\tau = 2\pi ft$, we can write an equation for the probe temperature at an arbitrary time:

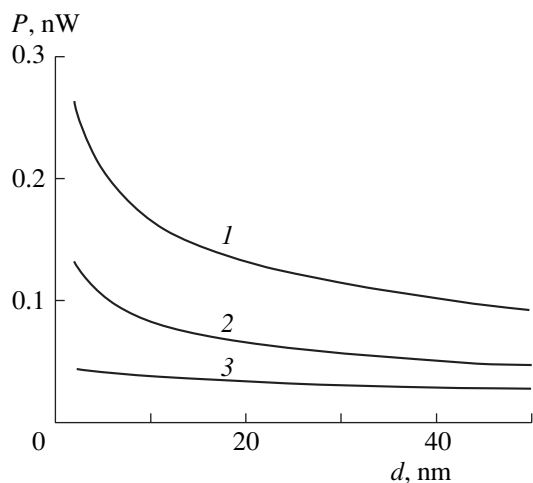$$\frac{dT}{d\tau} = \beta_1(T_1 - T) + \beta_2(T_2 - T)$$

$$\times\frac{1}{(1 - \gamma_1\sin\tau)^2}\frac{1}{(1 - \gamma_2\sin\tau)},$$

(7)

where

$$\gamma_1 = \frac{A}{H + d}, \quad \gamma_2 = \frac{A}{d}, \quad T_1 - T_2 = \Delta T,$$

$(T - T_2)/\Delta T$
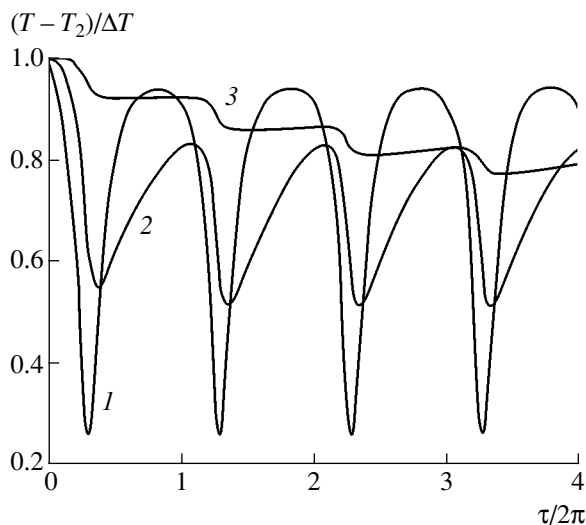
Fig. 2. Plots of the temperature of a parabolic nanoprobe versus time (in reduced dimensionless coordinates) for various frequencies $f = 1$ (1), 10 (2), and 100 kHz (3). The curves were calculated for the material parameters corresponding to silicon carbide [6] and $H = 500$ nm, $d = 20$ nm, $A = 19$ nm, and $R = 10$ nm.

P, nW

Fig. 3. Plots of the power P radiated by the scanning microscope probe versus distance to the sample surface d for the oscillation amplitude $d - 1$ nm, $T = 600$ K, $\Delta T = 1$ K, and various pairs of the probe parameters: (1) $H = 500$ nm, $R = 20$ nm; (2) $H = 500$ nm, $R = 10$ nm; (3) $H = 250$ nm, $R = 10$ nm.

and the coefficients β_1 and β_2 are given by the formulas

$$\beta_1 = \frac{9}{8\pi^3} \frac{k_B \omega_T}{f\rho C_p} \left(\frac{\omega_T}{c}\right)^3 \frac{\tilde{\gamma}(\varepsilon_0 - \varepsilon_\infty)}{(\varepsilon_\infty + 2)^2} f_1(\beta, q, \tilde{\gamma}), \quad (8)$$

$$\beta_2 = \frac{9}{16\pi^3} \frac{k_B \omega_T}{(H + d)^2 df\rho C_p}$$

$$\times \frac{\tilde{\gamma}^2(\varepsilon_0 - \varepsilon_\infty)^2}{(\varepsilon_\infty + 2)^2(\varepsilon_\infty + 1)^2} f_2(\beta, p, q, \tilde{\gamma}). \quad (9)$$

A solution to Eq. (11) with the initial condition $T(0) = \Delta T + T_2$ has the following form:

$$\frac{T - T_2}{\Delta T} = \exp(-\Phi(\tau))\left(1 + \beta_1 \int_0^\tau \exp(\Phi(x))dx\right), \quad (10)$$

$$\Phi(x) = \int_0^x \frac{dt}{(1 - \gamma_1 \sin t)^2} \frac{1}{(1 - \gamma_2 \sin t)}.$$

Figure 2 shows plots of the nanoprobe temperature versus time for various frequencies. These curves were calculated for the material parameters corresponding to silicon carbide [6] and $H = 500$ nm, $d = 20$ nm, $A = 19$ nm, $T = 600$ K, and $\Delta T = 1$ K. As can be seen from Fig. 2, an increase in the frequency of oscillations leads to a relaxation decrease in the temperature and the amplitude of its oscillations, with gradual saturation.

The energy radiated by the sample per cycle of oscillations is

$$W = \pi R H^2 \rho C_p \beta_2 \Delta T \int_0^{2\pi} \frac{dt}{(1 - \gamma_1 \sin t)^2} \frac{\tilde{\Phi}(t)}{(1 - \gamma_2 \sin t)}, \quad (11)$$

where $\tilde{\Phi}(t)$ is the function in the right-hand part of first equation (10). The average temperature T_r of the probe can be determined from Eq. (7) by setting $dT/d\tau = 0$ and averaging the right-hand part over the period, which yields $(T_r - T)/\Delta T = (1 + (\beta_1/2\pi\beta_2)\Phi(2\pi))^{-1}$. The T_r value is independent of the frequency f but depends on d, H, A, and other parameters of the system. As the frequency is increased, the power $P = Wf$ grows approximately according to a logarithmic law. This is related to the fact that local minima in the probe temperature correspond to the moments when the probe occurs in close contact with the surface and exhibits rapid cooling, which corresponds to smoothening of the integrand function in expression (11). When the frequency f grows, the amplitude of oscillations in the temperature decreases (Fig. 2) and the integral (11) increases.

Figure 3 shows the dependence of P on d for various pairs of the parameters R and H for the oscillation amplitude $d - 1$ nm. The output power can be significantly increased by optimizing the regime with respect to T, ΔT, H, A, and $d - A$ and selecting the optimum probe shape and material parameters. Allowance for the probe heating via the holder will also increase the output power, but this would require considering a three-dimensional heat exchange model. In concluding, it should be noted that the absolute values indicated in Fig. 3b are already comparable with or greater than the output power of scanning near field optical microscopes possessing much higher apertures (50–100 nm).

REFERENCES

1. Ch. H. Henry and R. F. Kazarinov, Rev. Mod. Phys. **68**, 801 (1996).

2. H. Schmid, H. Biebuyck, B. Michel, and O. J. F. Martin, Appl. Phys. Lett. **72**, 2379 (1998).

3. J. B. Pendry, J. Phys. C **11**, 6621 (1999).

4. O. Di Stefano, O. Savasta, and R. Girlanda, Phys. Rev. A **60**, 1614 (1999).

5. E. A. Vinogradov, Usp. Fiz. Nauk **172**, 1371 (2002) [Phys. Usp. **45**, 1213 (2002)].

6. F. Marquier, K. Joulain, J.-P. Mulet, *et al.,* Phys. Rev. B **69**, 155412 (2004).

7. A. I. Volokitin and B. N. J. Persson, Phys. Rev. B **69**, 045417 (2004).

8. G. V. Dedkov and A. A. Kyasov, Pis'ma Zh. Tekh. Fiz. **30** (13), 65 (2004) [Tech. Phys. Lett. **30**, 560 (2004)].

9. G. V. Dedkov and E. G. Dedkova, Pis'ma Zh. Tekh. Fiz. **30** (6), 52 (2004) [Tech. Phys. Lett. **30**, 240 (2004)].

10. G. V. Dedkov and A. A. Kyasov, Pis'ma Zh. Tekh. Fiz. **30** (13), 65 (2004) [Tech. Phys. Lett. **30**, 560 (2004)].

11. G. V. Dedkov and A. A. Kyasov, Fiz. Tverd. Tela (St. Petersburg) **44**, 1729 (2002) [Phys. Solid State **44**, 1809 (2002)].

Translated by P. Pozdeev

Special Features in the Pyroelectric Properties
of PZT Films Containing Excess Lead Oxide

A. A. Bogomolov[a,*], O. N. Sergeeva[a], D. A. Kiselev[a],
E. Yu. Kaptelov[b], and I. P. Pronin[b]

[a] Tver State University, Tver, Russia
[b] Ioffe Physicotechnical Institute, Russian Academy of Sciences, St. Petersburg, 194021 Russia
* e-mail: Alexey.Bogomolov@tversu.ru
Received January 18, 2005

Abstract—Pyroelectric hysteresis in unipolar lead zirconate titanate (PZT) films was studied upon preliminary poling in a strong external electric field and immediately in the applied external field. The asymmetry of the observed hysteresis loops is considered within the framework of an electromechanical approach to the phenomenon of natural unipolarity (spontaneous polarization) in thin-film ferroelectric capacitors formed on silicon and glass-ceramic composite substrates. © 2005 Pleiades Publishing, Inc.

Thin integrated ferroelectric films based on lead zirconate titanate (PZT) find increasing use in microelectronics for the development of nonvolatile memory (NVFRAM) devices, microelectromechanical systems (MEMS), and pyroelectric matrix sensors [1, 2]. An important feature of the synthesis of such films by RF magnetron sputtering consists in adding excess lead oxide (PbO) to the target material, which is necessary to ensure crystallization of the perovskite phase in the entire film volume. Unfortunately, the excess PbO is nonuniformly distributed both in depth and over the surface of the deposited thin film and may localize on the upper and lower interfaces, as well as on the grain boundaries [3–5].

The excess or lack of PbO is believed to account for the effect of unipolarity (spontaneous polarization), whereby a synthesized film turns out to be partly or completely polarized even without application of an external electric field [5–7]. The question of whether this effect has an electromechanical or flexoelectric nature is still under discussion [8–10]. In the first case, we deal with a combined action of the electric forces (space charge localized at the lower interface of a thin-film ferroelectric capacitor, which polarizes the ferroelectric layer) and mechanical compression caused by a difference in the linear thermal expansion coefficients of the ferroelectric layer and the substrate (which tends to realign the polar axis in the direction possibly close to the normal to the substrate surface) [8]. In the second case, the unipolarity is related to inhomogeneous mechanical stresses in the film, and the orientation of the unipolar axis depends on the direction of bending of the substrate with the synthesized multilayer thin-film composition [9, 10].

Measurements of the pyroelectric response offer one of the most reliable ways to obtain information concerning the character of the polarized state of a thin ferroelectric layer. In this study, we have measured the pyroelectric hysteresis loops in PZT films with inherent unipolarity, both in the presence of an external electric field and upon switching off the field. Previously, such measurements were either incomplete [11, 12] or missing.

The PZT films were obtained by RF magnetron sputtering of a $PbZr_{0.54}Ti_{0.46}O_3$ target containing additional PbO in an amount of 10 mol % [5]. The film composition corresponded to the region of rhombohedral symmetry immediately adjacent to the morphotropic phase boundary separating the tetragonal and rhombohedral modifications of the ferroelectric phase [13]. The ferroelectric film thickness was within 0.5–0.7 μm. The films had a polycrystalline structure with a grain size of 100–200 nm and a predominant ⟨111⟩ crystal orientation [8], The films were deposited onto glass-ceramic composite (Sitall CT-50) and single crystal silicon substrates. The upper and lower electrodes in thin-film ferroelectric capacitors were obtained by depositing 80-nm-thick platinum layers. The upper contact pad diameter was 130 μm.

The pyroelectric hysteresis loops of the films were measured using a dynamic method with heat fluxes modulated by rectangular pulses. The thermal radiation source was an LGN-222 laser (λ ~ 0.63 μm) with an average power of 30 mW and a pulse repetition rate of 24 Hz. The laser beam was focused in a 1-mm-diam spot on the film surface [14].

The results of these measurements showed that all the thin-film capacitor structures studied initially had a spontaneous polarization vector oriented toward the lower electrode, which was indicative of an impurity conductivity of the electron type. The dielectric hysteresis loops and reversible voltage dependences of the
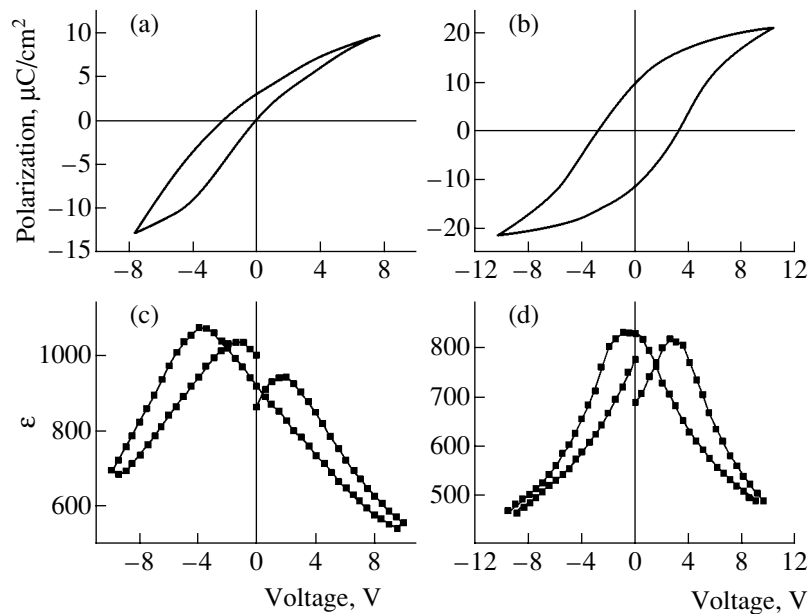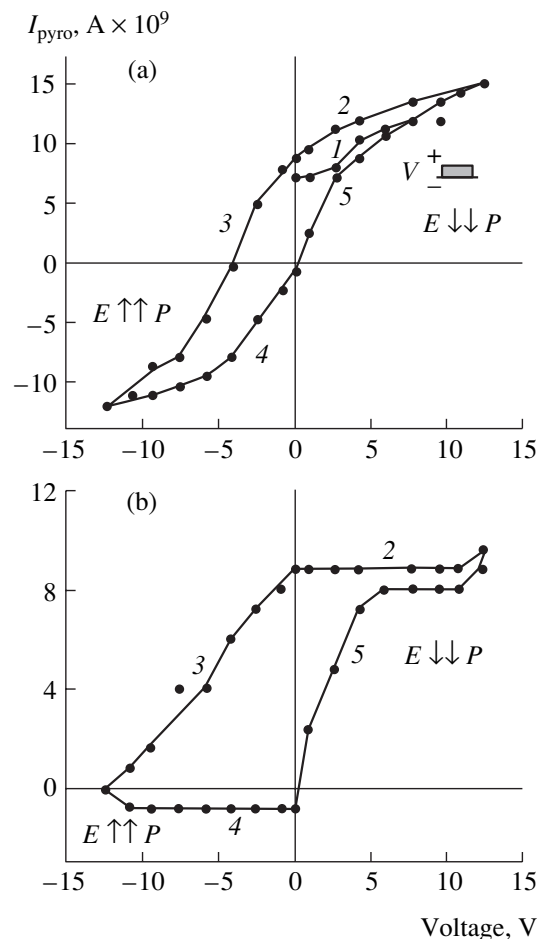
Fig. 1. (a, b) Dielectric hysteresis loops measured at 50 Hz and (c, d) reversible voltage dependences of the permittivity $\varepsilon(V)$ measured at 1 MHz for (a, c) the inherently unipolar PZT films and (b, d) the films upon thermal treatment at $T = 300°C$.

permittivity $\varepsilon(V)$ were substantially asymmetric and reflected the presence of an internal built-in electric field on the order of 20–25 kV/cm in the ferroelectric layer (Figs. 1a and 1b).

Figure 2a illustrates the influence of an external field on the pyroelectric response of PZT films. As the applied voltage (field strength) was increased, the response pyroelectric signal was initially independent of the field whose direction coincided with that of the self-polarization (Fig. 2a, curve *1*) and, then, beginning with a voltage of 3 V (equivalent to 40 kV/cm), gradually increased up to a level of about two times the initial value (which is probably related to the inclusion of 109° (or 71°) domains into the repolarization process). Further increase in the applied voltage (above 12 V) led to the appearance of noise hindering the direct measurement of a pyroelectric response in the applied field and the evaluation of the maximum (saturation) response. As the applied field in this direction was decreased to zero, the pyroelectric response dropped to a level slightly exceeding the initial value (Fig. 2a, curve *2*), which was indicative of a small value of the residual polarization induced by the external electric field.

A field of about 60 kV/cm applied in the opposite direction reoriented the sample polarization (Fig. 2a, curve *3*). In this case, the pyroelectric response did not exhibit saturation. As the field was decreased to zero, the pyroelectric response completely vanished (curve *4*). In contrast, further increase in the field (again coinciding with the self-polarization direction) led to reproduction of the above pattern (curve *5*).

The magnitude of the displacement field directed from upper to lower electrode was 30 kV/cm, which

Fig. 2. Pyroelectric hysteresis loops of inherently unipolar PZT films measured (a) in the presence of an external polarizing field and (b) upon switching off the external field.
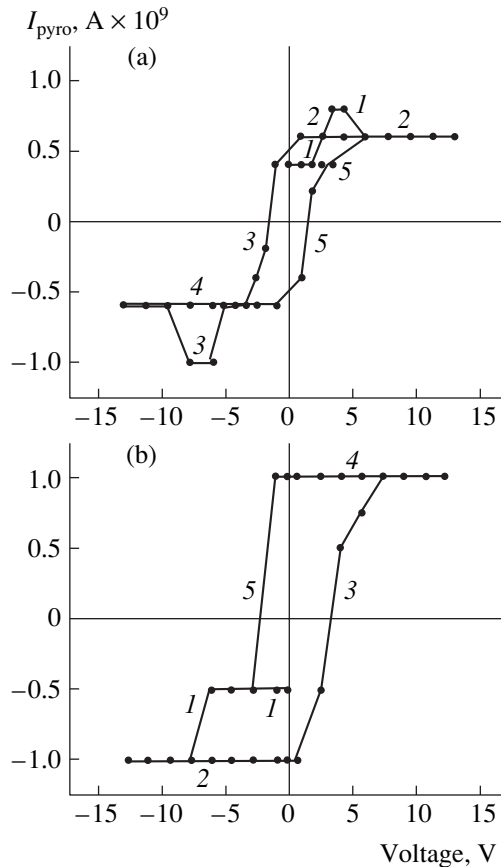
Fig. 3. Pyroelectric hysteresis loops of PZT films on (a) glass-ceramic composite and (b) single crystal silicon substrates measured upon thermal treatment at $T = 300°C$.

approximately corresponded to the field strength determined from the $\varepsilon(V)$ curve (Fig. 1b). A shift of the pyroelectric hysteresis loop for the inherently unipolar films also took place on the ordinate axis, which implied that the pyroelectric response was maximum for the maximum field applied in the direction coinciding with the vector of spontaneous (unipolar) polarization.

The asymmetry of the pyroelectric hysteresis loop was especially manifested when the pyroelectric response was measured after switching off the external electric field (Fig. 2b). Note a considerable value of the internal displacement field (~75 kV/cm) and a sharp difference between the values of pyroelectric response for the opposite directions of the electric field preliminarily applied to the field. Previous estimates [8] showed that the field at the lower interface might reach 150 kV/cm and above. For this reason, the possibility of reversal of the polarized state in this region (even by applying a very strong electric field) seems to be problematic. The internal field (Fig. 2b) reflects the field localized at the lower film interface to a greater extent than does the field determined from Fig. 2a. We believe that only a part of the film (corresponding to about half of its volume) is switched, which leads to an almost complete compensation of the pyroelectric response by

the oppositely polarized domains adjacent to the lower and upper interfaces.

The degree of unipolarity varied within 1.5 times from one contact pad to another, which might be indicative of an inhomogeneous distribution of PbO over the film surface. The maximum degree of unipolarity (≈0.8) was observed in the films deposited onto ceramic substrates, despite the considerable thickness (0.7 μm) and high permittivity of these films. The extremal values of permittivity (700–800) at the morphotropic phase boundary reduce the polarizing field at the lower interface of the ferroelectric film, thus objectively hindering its high polarizability [8]. The high unipolarity can be due to compressive mechanical stresses acting upon the PZT film from a ceramic substrate, which orient the spontaneous polarization axis along the substrate normal, in contrast to the tensile stresses acting upon the PZT layer from a silicon substrate [8].

Annealing of the ferroelectric capacitor structures was performed at temperatures close to and above the Curie point of PZT films. In all cases, the asymmetric hysteresis loop changed to a nearly symmetric loop (Figs. 1c and 1d), which was related to the electric charge redistribution between the upper and lower interfaces and the boundaries of grains in the ferroelectric film. It was expected that the hysteresis loop would exhibit considerable changes and the degree of unipolarity would significantly decrease [15].

It was impossible to obtain the pyroelectric loop immediately under the action of an external electric field (because of a considerable noise level), and the pyroelectric response was measured after switching off the external electric field (Figs. 3a and 3b). The shape of the pyroelectric hysteresis loop became significantly more symmetric (despite the presence of a residual polarization) and, on the whole, corresponded to the character of the dielectric hysteresis and $\varepsilon(V)$ curves. The pyroelectric response (and unipolarity) of the films decreased, but not as much as was expected. Moreover, the films deposited onto silicon substrates (Fig. 3b) exhibited a change in the spontaneous polarization direction, whereas the unipolarity vector in the films deposited onto ceramic substrates (Fig. 3a) retained its orientation from upper to lower electrodes. This behavior can be explained by a difference in the degree of texturing of the crystalline structure in the films deposited onto substrates of the two types (ceramic against single crystal silicon), which probably leads to a difference in the thermal-treatment-induced charge distribution between interfaces of the ferroelectric capacitor [15].

Thus, an excess of lead oxide in PZT films accounts both for their unipolarity and for a strong asymmetry of the pyroelectric hysteresis curves. Orientation of the spontaneous polarization vector is indicative of the electron conductivity in such films. A high degree of unipolarity can be observed in the films of practically important compositions near the morphotropic phase

boundary, where both piezoelectric and pyroelectric coefficients reach their maximum possible values.

REFERENCES

1. J. F. Scott and C. A. Paz de Araujo, Science **246**, 1400 (1989).

2. R. W. Whatmore, Ferroelectrics **225**, 179 (1999).

3. V. V. Lemanov, G. N. Mosina, L. M. Sorokin, *et al.*, Fiz. Tverd. Tela (St. Petersburg) **38**, 3108 (1996) [Phys. Solid State **38**, 1700 (1996)].

4. Zh.-J. Wang, R. Maeda, and K. Kikuchi, Jpn. J. Appl. Phys., Part 1 **38**, 5242 (1999).

5. V. P. Afanas'ev, G. N. Mosina, A. A. Petrov, *et al.*, Pis'ma Zh. Tekh. Fiz. **27** (11), 56 (2001) [Tech. Phys. Lett. **27**, 467 (2001)].

6. M. Kobune, H. Ishito, A. Mineshige, *et al.*, Jpn. J. Appl. Phys., Part 1 **37**, 5154 (1998).

7. Zh. Song, W. Ren, L. Zhang, *et al.*, Thin Solid Films **353**, 25 (1999).

8. I. P. Pronin, E. Yu. Kaptelov, A. V. Gol'tsev, and V. P. Afanas'ev, Fiz. Tverd. Tela (St. Petersburg) **45**, 1685 (2003) [Phys. Solid State **45**, 1768 (2003)].

9. A. Gruverman, B. J. Rodriguez, A. I. Kingon, *et al.*, Appl. Phys. Lett. **83**, 728 (2003).

10. W. Ma and L. E. Cross, Appl. Phys. Lett. **82**, 3293 (2003).

11. J. Lee, S. Esayan, J. Prohaska, and A. Safari, Appl. Phys. Lett. **64**, 294 (1994).

12. A. S. Sigov, M. I. Maleto, E. Ph. Pevtsov, *et al.*, Ferroelectrics **226**, 183 (1999).

13. B. Jaffe, W. J. Cook, and H. Jaffe, *Piezoelectric Ceramics* (Academic Press, London, 1971).

14. A. A. Bogomolov, O. N. Sergeeva, D. A. Kiselev, *et al.*, in *Proceedings of the International Scientific-Technical Conference on Piezoelectrics, Moscow, 2003* (Moscow University of Electronics and Automatics, Moscow, 2004), pp. 23–27.

15. I. P. Pronin, E. Yu. Kaptelov, E. Yu. Tarakanov, and V. P. Afanas'ev, Fiz. Tverd. Tela (St. Petersburg) **44**, 1659 (2002) [Phys. Solid State **44**, 1736 (2002)].

Translated by P. Pozdeev

Reflex Triode with Virtual Cathode and Emitter Based on Magnetically Confined Discharge

S. V. Bulychev, A. E. Dubinov, I. L. L'vov, S. A. Sadovoĭ, and V. D. Selemir

Institute of Experimental Physics, Russian Federal Nuclear Center, Sarov, Russia

Received January 20, 2005

Abstract—A new reflex triode with virtual cathode (VC) was developed and experimentally studied, in which surface discharge along a ferroelectric is used as the source of electrons and loop antennas are used for extracting the radiation. The electrode system in the proposed device is designed so that magnetic forces of the discharge would confine the plasma to the dielectric surface. This system provides for a ~20-fold increase in the generation time as compared to that achieved in prior designs. The new reflex triode generates wideband RF pulses in a range of frequencies from 20–230 MHz at a power of about 140 W. © *2005 Pleiades Publishing, Inc.*

Electromagnetic radiation generators with virtual cathodes (VCs), including vircators and reflex triodes, constitute a wide class of high-power relativistic microwave triode oscillators possessing unique properties, which are still under extensive investigation and development [1–4]. The principle of operation of these devices is based on the injection of an electron beam into an equipotential cavity (in vircators) or a cavity with retarding electric field (in reflex triodes), with a current sufficient to form a VC. The oscillating VC acts as the source of electromagnetic radiation extracted from the cavity with the aid of an antenna system.

Our recent work [5] outlined a new direction in the development of microwave oscillators with VCs, which provides moderate-power radiation sources operating at a relatively low accelerating voltage from several units to tens of kilovolts. Such generators can fill the gap between usual triodes (employing thermionic emission) with a diode voltage of up to several kilovolts and relativistic reflex triodes (employing explosive electron emission) operating at a voltage of 100 kV and above.

The new possibility is provided by the use of special electron emitters based on the phenomenon of pulling electrons out of a complete vacuum discharge confined to a dielectric surface. In order to reduce the voltage necessary for initiating the surface discharge, it was suggested [5] to use ferroelectric materials as dielectrics with high permittivities ε. In this context, we have previously developed and tested a new reflex triode with VC, which operates at an accelerating voltage as low as 1 kV. Loaded on a system of loop antennas, this reflex triode provides an output radiation power of 80 W at a frequency of 320 MHz.[1] The RF pulse duration in this triode does not exceed 100 ns, which is

related to the fact that a magnetic pressure of the discharge current drives the surface discharge plasma to the anode grid. As a result, the plasma shortens the cathode–anode gap of the reflex triode, thus terminating the electron beam production.

In order to increase the generation time, it is expedient to use an electron source employing either an incomplete surface discharge or a magnetically confined surface discharge as described in [7]. According to this technical solution, we have designed, constructed, and tested a new reflex triode. The device, which is schematically depicted in Fig. 1, comprises a source of the control voltage U_c, a source of the accelerating voltage U_a, a system for extracting the electromagnetic radiation (loop antennas), and a vacuum chamber. The vacuum chamber contains a collector, an electron-transparent anode (representing a grid made of 0.1-mm tantalum wire with a geometric transparency of 95%) connected to the U_a source, a plasma-forming surface discharge dielectric element (a disk made of a ferroelectric PZT ceramics of the TsTS-19 grade) mounted inside a grounded electrode, and a control electrode mounted with one end in the hole at the center of the dielectric element and connected with its other end to the U_a source. The control and grounded electrodes form a gap at the surface of the plasma-forming dielectric element on the anode side. The positions of the anode and collector relative to the dielectric surface can be adjusted within 1.5 mm.

The antenna system comprises four parallel connected loops uniformly arranged over the azimuth relative to the triode axis. The loops, made of a 3-mm copper wire, have a rectangular shape with a perimeter length approximately equal to a quarter-wavelength of the generated radiation.

The principle of operation of the new reflex triode is as follows. A positive high-voltage pulse applied to the control electrode initiates a discharge at the dielectric

---

[1] It should be noted that Drori *et al.* [6] developed and tested a microwave oscillator of another type (gyrotron) with a ferroelectric emitter and obtained an output radiation power of 25 W at an accelerating voltage of 9 kV.
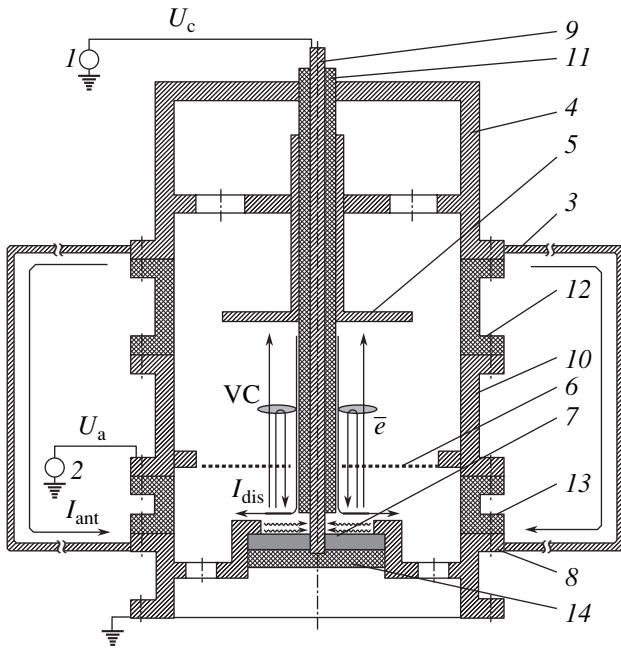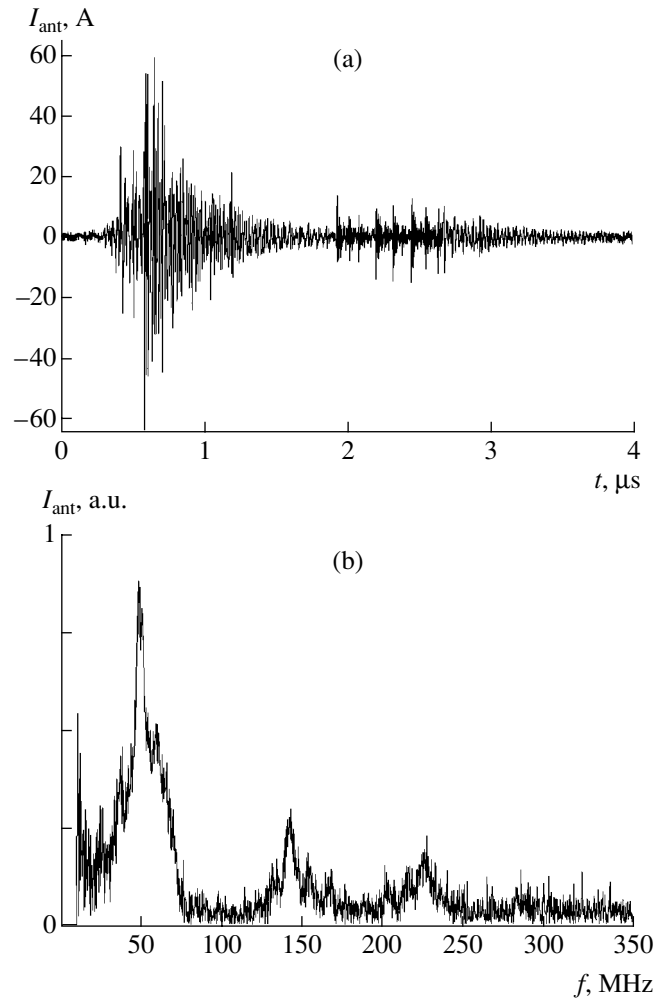
Fig. 1. Schematic diagram of the reflex triode: (*1*) control voltage source; (*2*) accelerating voltage source; (*3*) loop antennas for extracting microwave radiation; (*4*) vacuum chamber; (*5*) collector; (*6*) anode grid; (*7*) plasma-forming dielectric element with a central hole; (*8*) grounded electrode; (*9*) control electrode; (*10*) anode flange; (*11*) insulator; (*12*, *13*) insulating flanges; (*14*) insulating disk.

Fig. 2. Typical characteristics of the reflecting triode: (a) oscillogram of the total current pulse measured in the loop antenna; (b) typical output radiation spectrum.

surface in the gap between this electrode and the edge of the grounded electrode. A high constant positive voltage is applied to the anode from the U_a source via the anode flange. This anode voltage pulls electrons from the surface discharge plasma. These electrons travel through the transparent grid and form a VC behind the anode. The current of electrons passing through the VC and reaching the collector is transferred via the conducting elements to the loop antennas connected between the vacuum chamber and the grounded electrode. The antennas radiate electromagnetic waves in the microwave frequency range. In Fig. 1, thick arrows indicate the direction of discharge currents, wavy arrows show the motion of electrons in the discharge plasma, and thin solid arrows indicate the motion of electrons in the beam pulled out of the discharge.

In the proposed reflex triode, the surface discharge circuit is such that the Ampere forces confine the plasma to the dielectric surface (rather than pushing the plasma out of the gap). Indeed, the interelectrode gap is situated on the inner side of the surface discharge circuit and, hence, the Ampere forces hinder the motion of plasma toward the anode and keep plasma at the dielectric surface. Since the plasma is confined to the dielectric, the distances from plasma to the anode and to the VC remain constant. Therefore, the geometric parameters of the potential well, in which electrons reflected

from the VC are oscillating, also remain constant, and the oscillation frequency is unchanged. This favors stabilization of the reflex triode frequency, which is equal to the frequency of electron oscillations in the potential well. Since the plasma is separated from the anode, the emitter–anode gap is not shorted and the anode potential is constant. For this reason, the energy of electrons pulled out of the plasma is not decreased and the beam formation is not terminated. This explains a significant increase in the beam pulse duration, the generation time, and the output energy as compared to those achieved previously [5].

The tests were performed on a reflex triode prototype with an emitter–anode grid gap of 5 mm and a plasma-emitting surface discharge area of 30 mm². Powered with 1-kV pulses, the oscillator generated wideband RF pulses with a power of 140 W, a repetition rate of 50 Hz, and a radiation frequency in the range from 50 to 230 MHz. Figure 2a shows the typical oscil-

logram of the total current pulse measured in the loop antenna. Figure 2b presents the typical output radiation spectrum. Thus, using the technical solutions developed in [7], we have increased the pulse duration by a factor of ~20 and the pulse energy by a factor of ~30.

In conclusion, we can outline the prospects for future development of the proposed reflex triode. According to the well-known Child's law, an increase in the diode voltage by a factor of α must lead to an increase in the output power by a factor of $\alpha^{5/2}$. This circumstance provides the possibility for the reflex triodes to fill the aforementioned gap between usual and relativistic triodes. Although the reflex triode prototype was studied only within the framework of verification of the technical solutions proposed in [7], we also plan to use this device for studying the RF pulse transmission through a gas discharge plasma.

REFERENCES

1. A. N. Didenko, A. P. Arzin, A. G. Zherlitsyn, *et al.*, in *Relativistic Microwave Electronics* (IPF AN SSSR, Gorki, 1984), Issue 4, p. 104 [in Russian].
2. A. A. Rukhadze, S. D. Stolbetsov, and V. P. Tarakanov, Radiotekh. Élektron. (Moscow) **37**, 385 (1992).
3. A. E. Dubinov and V. D. Selemir, Zarubezhn. Radioélektronika, No. 4, 54 (1995).
4. A. E. Dubinov and V. D. Selemir, Radiotekh. Élektron. (Moscow) **47**, 645 (2002).
5. S. V. Bulychev, A. E. Dubinov, V. S. Zhdanov, *et al.*, Fiz. Plazmy **26**, 639 (2000) [Plasma Phys. Rep. **26**, 598 (2000)].
6. R. Drori, M. Einat, D. Shur, *et al.*, Appl. Phys. Lett. **74**, 335 (1999).
7. S. V. Bulychev, A. E. Dubinov, I. L. L'vov, *et al.*, RF Patent No. 2214648 (2001); Byull. Izobret., No. 29 (2003).

Translated by P. Pozdeev

Evolution of Nonequilibrium Aerosol Parameters in Crown-Streamer Discharge Plasma

A. V. Kozyrev*, A. G. Sitnikov, and N. S. Sochugov

Institute of High-Current Electronics, Siberian Division, Russian Academy of Sciences, Tomsk, Russia
* e-mail: kozyrev@to.hcei.tsc.ru
Received January 21, 2005

Abstract—Nonstationary parameters of an aerosol formed from unsaturated vapors of styrene and *n*-hexane in a pulsed crown-streamer discharge in air or argon at atmospheric pressure have been studied. In the initial stage of aerosol formation, the concentration of aerosol particles was on the order of 10^7 cm^{-3}. The characteristic time of nonequilibrium hexane aerosol degradation in the experimental chamber amounted to several hours. The aerosol particle size distribution function has a bimodal shape. Within the first seconds upon aerosol formation, the maximum particle size does not exceed 0.6 μm, whereas in several hours, the boundary of the particle size spectrum reaches the micron range. © 2005 Pleiades Publishing, Inc.

As is known, chemical processes in low-temperature plasma may lead to the formation of aerosols. As a rule, such aerosols consist of nonvolatile substances appearing as a result of plasmachemical reactions [1]. Under certain conditions, when the concentration of nonvolatile products is very low because of a small energy deposited in the plasma, metastable aerosols may form even from unsaturated vapors of organic compounds [2].

The aim of this study was to determine the parameters of such a nonequilibrium aerosol and to follow their evolution with time.

The formation of a nonequilibrium aerosol in discharge plasma can be described as follows. Ions appearing in the ionized gas act as centers for the condensation of organic vapor, on which the primary nuclei-droplets of nanometer dimensions are formed. The subsequent kinetics of aerosol formation depends on the relative rates of interrelated processes such as the coagulation of charged aerosol particles and their recharge, evaporation, and loss on the chamber walls.

We have studied the aerosol formed in the plasma of a crown-streamer discharge excited by a generator producing voltage pulses with an amplitude of 80 kV, a base width of 5 ns, and a repetition rate of 100 Hz [3]. The pulse energy was 0.03 J, so that the average power deposited in the discharge was 3 W. The high-voltage pulses from the generator were transmitted via a coaxial line with a wave impedance of 55 Ω and applied to a system of electrodes comprising a grounded cylindrical case with an internal diameter of 110 mm and a high-voltage electrode of the squirrel cage type consisting of 24 parallel wires with a diameter of 0.2 mm. The interelectrode gap width was 2 cm. The application of voltage pulses of a very short duration led to the excitation of incomplete crown-streamer discharge between the electrodes.

A gas (argon or air) at atmospheric pressure, containing unsaturated vapor of styrene or *n*-hexane (1–8% of the corresponding saturated vapor pressure), was supplied via an input valve to the discharge zone (with a volume of about 2 l), where the aerosol formation was initiated. Then, the gas entered a buffer aerosol chamber of variable volume (0.63–2.9 l) and exhibited partial mixing. Finally, the gas flow reached the main aerosol chamber with a volume of 31 l, which was made of glass plates and had a parallelepiped shape with dimensions 25 × 31 × 40 cm. The gas was supplied at a flow rate of 250 l/h. By measuring the rate of hydrocarbon consumption at the input of the discharge zone, it was possible to evaluate the density M [g/m^3] of hydrocarbons in the plasma volume. For the gas flow parameters and the generator power indicated above, the specific deposited energy was about 0.04 J/cm^3.

After filling of the main aerosol chamber, which usually required about 20 min, the input and output of this chamber were closed, the pulse generator was switched off, and the spectrum of the optical attenuation factor α [cm^{-1}] in a wavelength range of $\lambda = 360$–750 nm was measured over a period of several hours. These measurements were performed as follows. The radiation from a source with a continuous spectrum (a halogen lamp) was transmitted twice through the aerosol chamber (with reflection from a mirror). The output light beam was collimated (two parallel 1-mm-wide slits spaced by 100 mm), passed through a monochromator, and detected by a photoresistor. The output voltage was measured using a digital voltmeter. The optical path length in the aerosol chamber was 850 mm. The optical attenuation factor in these experiments reached maximum values on the order of 4.2 m^{-1}.
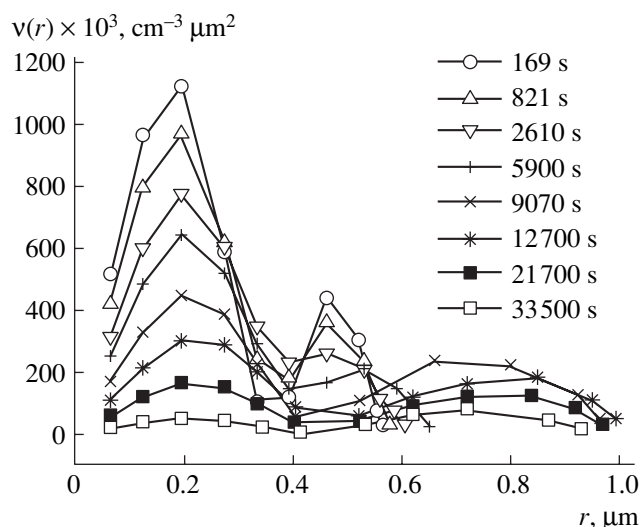
Fig. 1. Temporal evolution of the particle distribution with respect to radius for a styrene aerosol in argon ($M = 1.4$ g/m^3).

Using the results of measurements of the $\alpha(\lambda)$ spectrum and the well-known method of solution of the inverse problem of scattering, we studied evolution of the aerosol particle size distribution. The calculations were performed using a regularization algorithm based on the smoothening functional according to the Tikhonov method, with direct minimization of this functional in the K-dimensional vector space [4].

The dimensions of aerosol particles were also determined by independent methods. In some experiments with the styrene aerosol in argon, the particles were either deposited onto glass substrates situated in the aerosol chamber or collected on the analogous substrates situated outside the chamber and then polymerized under UV irradiation. The deposits were analyzed using an optical microscope (MII-4) and an atomic force microscope (NT-MDT Solver P47).

The results of these experiments showed that the hexane aerosol did not leave significant traces on the chamber walls. This was a convincing evidence for a nonequilibrium character of the process of aerosol formation. At the same time, aerosol formed in styrene

Aerosol parameters

Compound	Medium	M, g/m^3	M_0, %	M_V, g/m^3	N_a, cm^{-3}
Styrene	Argon	1.4	4.6	0.25	5.2×10^7
Styrene	Air	1.46	5.2	0.09	1.1×10^7
n-Hexane	Argon	3.8	1.0	0.1	1.1×10^7
n-Hexane	Argon	21	5.2	0.07	1.3×10^7
n-Hexane	Argon	31	8.0	0.05	1.4×10^7
n-Hexane	Air	31.6	7.9	0.55	3.0×10^7

vapor was deposited on the walls and bottom of the chamber. This is probably related to a partial polymerization of styrene under the action of discharge (radiation factors). In order to terminate the evaporation process, it was necessary to irradiate the deposit additionally with UV light for several minutes.

Figure 1 presents the calculated particle size distribution functions for a styrene aerosol, which were obtained from the experimental optical transmission data by solving the inverse problem of scattering. The curves show the evolution of the volume of particles $v(r)$ with the radius r with time after aerosol formation. As can be seen, the aerosol has a bimodal disperse structure, and the time to complete aerosol degradation in the chamber volume amounts to several hours.

The first group of particles in the distribution has a modal radius of about 0.2 μm, while the right-hand boundary of this mode reaches 0.4 μm. These parameters remain virtually unchanged with time. The particle size distribution function for the second mode significantly changes in the course of aerosol evolution: both the average radius and the dispersion of this mode increase with time, with the modal radius reaching 0.75 μm and the right-hand boundary shifting to the micron range. The total concentration of aerosol particles in both modes monotonically decreases with time.
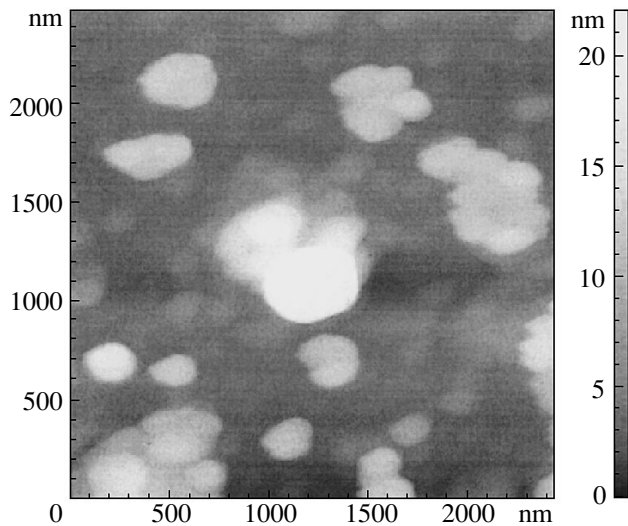
Experimental values of the aerosol parameters in the initial stage (within the first several minutes after generator switch-off) for a gas phase temperature of $T \approx 290$ K are summarized in the table. Here, M is the hydrocarbon vapor density in the gas phase, M_0 is the relative degree of saturation (percentage) of the hydrocarbon vapor, M_V is the mass density of the aerosol, and N_a is the number density of aerosol particles.

As can be seen from data in the table, the M_V of the styrene aerosol in argon is about one order of magnitude higher than the value in air at approximately equal degrees of vapor saturation $M_0 \approx 5\%$. Assuming that ions serve as the centers of condensation for the liquid phase nucleation, this result may imply that the ion density for the discharge in argon is about ten times that for the discharge in air. The situation for hexane is the inverse: M_V is lower in argon than in air for approximately the same $M_0 \approx 8\%$. This difference is probably related to the fact that oxidative plasmachemical reactions of styrene in air (oxygen-containing medium) may lead to the formation of low-volatile compounds capable of condensation.

It is interesting to note that an increase in the hexane vapor density M in argon is accompanied by a decrease in the mass density M_V of the corresponding aerosol, while the number density of aerosol particles exhibits a slight increase. We believe that this behavior is related to a relatively high degree of ionization of hexane vapor in the discharge plasma and to the fact that charged hexane molecules do not pass to the condensed phase.

Fig. 2. The typical AFM micrograph of styrene aerosol particles formed in a crown-streamer discharge in argon and collected on a glass substrate outside the chamber 5 min after switching off the voltage generator ($M = 1.5$ g/m^3).

Investigation of the samples of styrene aerosol in argon, which were collected on glass substrates and examined in the atomic force microscope (AFM) (Fig. 2) and in the optical microscope, showed that the radii of aerosol particles change from hundreds of nanometers in the initial stage to microns in the final stage. This result agrees with the data on the particle size distribution obtained from the optical measurements. As can be seen in the AFM image (Fig. 2), particles with radii near and below 0.5 μm consist of smaller species with a radius on the order of 0.1 μm. Examination of the coarse particles with dimensions on the order of microns showed that these are monolithic objects with the shape close to an oblate spheroid, that is, represent condensed drops.

In our experiments on aerosol formation from unsaturated vapors, the mass density of styrene aerosols correlates with the ion density in the crown-streamer discharge plasma. The method of aerosol formation described above can provide a basis for generating liquid-droplet aerosols, cleaning air from low concentrations of organic impurities, and obtaining solid polymeric particles of submicron dimensions.

REFERENCES

1. V. E. Fortov, A. G. Khrapak, and I. T. Yakubov, *Physics of Nonideal Plasmas* (Fizmatlit, Moscow, 2004; World Sci. Publ., London, 1999).

2. S. P. Bugaev, A. V. Kozyrev, V. A. Kuvshinov, and N. S. Sochugov, Dokl. Ross. Akad. Nauk **361**, 612 (1998) [Dokl. Phys. **43**, 473 (1998)].

3. S. P. Bugaev, V. B. Zorin, and B. M. Kovalchuk, in *Proceedings of the 10th IEEE International Pulsed Power Conference, Albuquerque, 1995*, pp. 1206–1210.

4. I. E. Naats, *Theory of Multifrequency Laser Probing of Atmosphere* (Nauka, Novosibirsk, 1980) [in Russian].

Translated by P. Pozdeev

Variation of the Orientational Order Parameter in a Nematic Liquid Crystal–COANP–C$_{70}$ Composite Structure

N. V. Kamanina[a,*], A. V. Komolkin[b,**], and N. P. Yevlampieva[a]

[a] Vavilov Optical Institute, State Scientific Center of the Russian Federation, St. Petersburg, Russia
[b] Fock Institute of Physics, St. Petersburg State University, St. Petersburg, Russia
*e-mail: * kamanin@ffm.ioffe.ru; ** komolkin@esr.phys.spbu.ru*

Received January 17, 2005

Abstract—Behavior of the orientational order parameter in structures of the nematic liquid crystal (NLC)–organic donor–fullerene type was studied by pulsed ^{1}H NMR techniques. In the NLC sensitized by a fullerene-containing charge transfer complex, the order parameter at temperatures 10 K below the nematic–isotropic phase transition exhibits an increase and exceeds the value for the initial liquid crystal. This effect is not typical of nonmesogenic additives. © *2005 Pleiades Publishing, Inc.*

Introduction. The extensive development of optoelectronics and laser technologies has stimulated investigations aimed at increasing the performance of optical elements and devices. An important aspect of this work is the creation, synthesis, and characterization of new materials. There are substances which, being introduced into a liquid crystal matrix, significantly modify the spectral, photoelectric, dynamic, and optical (including nonlinear) properties of this matrix. The group of such additives includes fullerenes C$_{60}$ and C$_{70}$ [1–5].

Previously, it was demonstrated [6, 7] that the introduction of fullerene-containing complexes into a nematic liquid crystal (NLC) influences the speed of reorientation of NLC molecules in a liquid crystal cell. In particular, it was shown that the NLC cell switching rate can be increased by two orders of magnitude, which implies that the fullerene-containing NLC composites can be switched with characteristic times approaching those typical of fast smectics [8, 9]. However, NLCs are less expensive than smectics and can be more readily oriented. From the standpoint of simplification of the processing technology and minimization of the cost of components, fullerene-doped NLC structures offer some advantages over smectic mesophases.

Previously, we have successfully proved the high switching rate of fullerene-containing liquid crystals [8, 9] in experiments with various photosensitive systems (fullerene-containing charge transfer complexes based on various electron donors), obtained micrographs of such objects [8], and studied their polarization properties, which allowed the increase in the switching rate to be explained by growing macropolarization of the medium [10]. However, there were no direct investigations devoted to changes in the orientational order parameter of liquid crystals caused by the introduction of fullerene-containing complexes.

This Letter presents the results of investigation of the effect of fullerenes on the orientational order parameter of a liquid crystal in the case of an NLC modified by a complex of 2-cyclooctylamine-5-nitropyridine with C$_{70}$ fullerene (NLC–COANP–C$_{70}$ system).

Experiment: materials and techniques. We have studied an NLC belonging to the class of cyanobiphenyls in comparison to the same composition sensitized by a COANP–C$_{70}$ charge transfer complex. The electron affinity of the intramolecular fragment of COANP is 0.54 eV, which is about one-fourth of the value for the C$_{70}$ fullerene (2.65–2.70 eV) [11, 12]. For this reason, the fullerene molecule in the COANP–C$_{70}$ complex acts as an effective electron acceptor. The complex was synthesized from a fullerene powder containing 97% C$_{70}$ (Alfa Aesar, Johnson Matthey Co.). The content of fullerene relative to COANP was 2.0–0.5 wt %, and the ratio of NLC to the photosensitive component in the system studied was 6 : 1 (v/v).

The samples of initial and fullerene-sensitized NLCs were studied by ^{1}H NMR spectroscopy. The measurements were performed on a Bruker SXP 4-100 spectrometer with a modified detecting unit. The resonance frequency of ^{1}H nuclei was 70.0 MHz, which corresponded to a magnetic induction of 1.64 T. The free induction signal was excited by single 90° pulses with a duration of 7 μs. The response signal was digitized at 4096 points at a 3-μs step and accumulated over 8–64 scans. Although the base line was distorted by instrumental factors, the positions of characteristic peaks in the ^{1}H NMR spectra remained unchanged (Fig. 1).

The samples of liquid crystal compositions were placed into standard 5-mm-diameter ampules and heated by a flow of air in the spectrometer cavity. The sample temperature was stabilized to within ±0.3 K

over short periods of time and within ±0.5 K over a period of 12 h. In the course of experiments, the samples were heated to a temperature 5 K above the nematic–isotropic phase transition point and then slowly (1 K for 5 min) cooled. The phase transition was indicated by the appearance of a characteristic broad component in the spectra.

Results and discussion. The initial liquid crystal has a nematic–isotropic phase transition temperature $T_{NI} = 61 \pm 0.5°C$. Introduction of the COANP–C$_{70}$ complex into the NLC composition led to a depression of the transition temperature to $48.0 \pm 0.5°C$. Such behavior is usually observed upon introduction of nonmesogenic additives into liquid crystals.

The orientational order parameter of a liquid crystal is characterized in terms of the average deviation of the long axes of molecules from the direction of their predominant orientation (i.e., from the director):

$$S = \left\langle \frac{3\cos^2\theta - 1}{2} \right\rangle, \qquad (1)$$

where θ is the angle between the long axis of a molecule and the director [13] and angle brackets denote averaging over the ensemble. In NLCs, the $S(T)$ value increases with decreasing temperature T: from 0.3–0.4 at $T = T_{NI}$ to 0.7–0.8 near the crystallization temperature [14].

The ^{1}H NMR spectra are determined mainly by the direct magnetic dipole–dipole interactions of ^{1}H nuclei [12]. In the presence of multiple interacting pairs of nuclei, the spectrum appears as a broad partly structured line (Fig. 1). In the temperature range of the existence of a nematic phase, the set of possible conformations of NLC molecules in the ensemble can be considered independent of the temperature. For this reason, the Hamiltonian $\mathcal{H}(T)$ (i.e., the energy) of the dipole–dipole interaction is proportional to the orientational order parameter:

$$\mathcal{H}(T) = S(T)\mathcal{H}_{S=1}, \qquad (2)$$

where $\mathcal{H}_{S=1}$ is the Hamiltonian of the dipole–dipole interaction in a molecule aligned with the director. Relation (2) implies that the shape of the NMR line is independent of the temperature (only the frequency scale may change). The splitting $\Delta\nu(T)$ between characteristic points of the NMR spectrum (we selected the separation between the external doublet components indicated in Fig. 1) is proportional to the orientational order parameter $S(T)$.

Figure 2 shows experimental plots of the splitting $\Delta\nu(T)$ in the ^{1}H NMR spectra versus $\Delta T = T_{NI} - T$ for the pure NLC and the NLC–COANP–C$_{70}$ system. The experimental curves were approximately described using the formula [13, p. 227]

$$S(T) = K\left[1 + \left(1 - \frac{8}{9}\frac{T - T_{NI}}{T_{NI} - T_{NI}^*}\right)^{1/2}\right] \qquad (3)$$
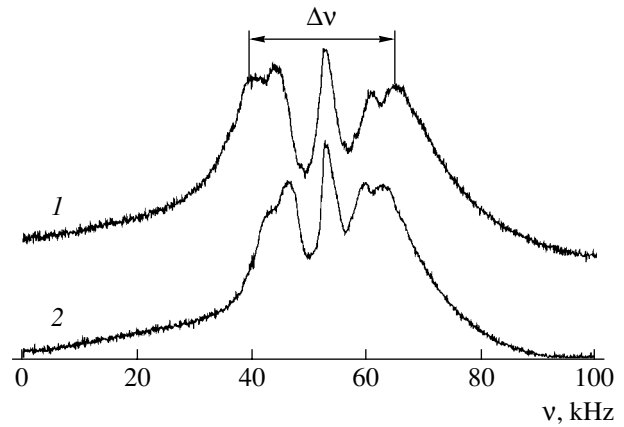
Fig. 1. Typical ^{1}H NMR spectra of (*1*) the NLC at $\Delta T = 36$ K and (*2*) the NLC–COANP–C$_{70}$ composition at $\Delta T = 14$ K. In spectrum *1*, $\Delta\nu$ is the splitting of the outer doublet components used as a measure of the line width.
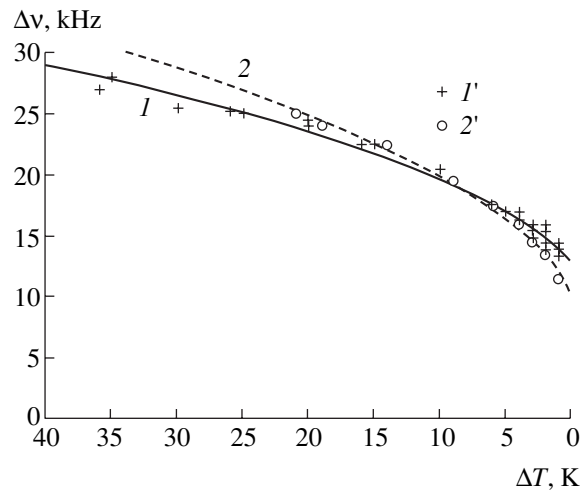
Fig. 2. Plots of the outer doublet splitting $\Delta\nu$ versus $\Delta T = T_{NI} - T$ for (*1, 1'*) pure NLC and (*2, 2'*) NLC–COANP–C$_{70}$ composition: (*1', 2'*) experiment; (*1, 2*) approximation using formula (2).

with two variable parameters: K (a temperature-independent constant) and T_{NI}^* (the temperature at which only the nematic phase is stable). As can be seen from Fig. 2, the two temperature dependences intersect at $\Delta T = 9$ K. The orientational order parameter of the NLC–COANP–C$_{70}$ system near T_{NI} is lower than that of the pure NLC, while at $\Delta T > 9$ K the order parameter of the modified liquid crystal is greater than that of the initial composition. This effect on the degree of orientational order in liquid crystals is not typical of nonmesogenic additives. It should be noted that the observed difference exceed the uncertainty of determination of the $\Delta\nu(T)$ value.

We believe that the charge transfer complex introduced into the NLC matrix is polarized as a result of the

interaction with a strong electric dipole of the alkylcy-anobiphenyl molecule. The polarized complex is surrounded by a solvated shell with increased order of the NLC molecules. This effect may account for the observed difference in the degree of order in the two systems studied. Such a structurization may lead to a decrease in size of the liquid crystal domains to the dimensions of the solvated shell of the fullerene-containing complex. This change must facilitate reorientation of these domains under the action of external fields and, accordingly, increase the NLC cell switching rate.

Conclusions. A fullerene-containing NLC–COANP–C_{70} system was studied by pulsed ^1H NMR techniques. Introduction of the COANP–C_{70} charge transfer decreases the nematic–isotropic phase transition temperature T_{NI} and changes the orientational order parameter of the initial liquid crystal. When the temperature decreases by 10 K below T_{NI}, the fullerene-containing complex favors an increase in the order parameter in the NLC–COANP–C_{70} system as compared to that in the initial liquid crystal, which is not typical of nonmesogenic additives to liquid crystals. In order to elucidate a model of the interaction between the fullerene-containing complex and the liquid crystal matrix, we are planning to study the temperature dependence of the orientational order parameter and the dependence of the diffusion coefficient on the COANP–C_{70} complex concentration in the liquid crystal matrix.

REFERENCES

1. A. Itaya, I. Sizzuki, Y. Tsuboi, and H. Miyasaaka, J. Phys. Chem. B **101**, 5118 (1997).
2. V. P. Belousov, I. M. Belousova, V. G. Bespalov, *et al.*, Opt. Zh. **64** (9), 82 (1997).
3. K. Dou, J. Y. Du, and E. T. Knobbe, J. Lumin. **83**–**84**, 241 (1999).
4. N. Kamanina, A. Barrientos, A. Leyderman, *et al.*, Mol. Mater. **13**, 275 (2000).
5. N. V. Kamanina, *Fullerenes as New Optical Materials: Properties and Applications* (State Electrotechnical University, St. Petersburg, 2002) [in Russian].
6. N. V. Kamanina, J. Opt. A: Pure Appl. Opt. **4**, 571 (2002).
7. L. P. Rakcheeva and N. V. Kamanina, Pis'ma Zh. Tekh. Fiz. **28** (11), 28 (2002) [Tech. Phys. Lett. **28**, 457 (2002)].
8. N. V. Kamanina, I. Yu. Denisyuk, M. M. Mikhailova, and I. Yu. Sapurina, Opt. Zh. **71** (5), 72 (2004).
9. N. V. Kamanina, A. I. Denisyuk, M. M. Mikhailova, and I. Yu. Sapurina, Mol. Cryst. Liq. Cryst. (2005) (in press).
10. N. V. Kamanina, Usp. Fiz. Nauk **175**, 445 (2005) [Phys. Usp. **48** (4) (2005)].
11. L. V. Gurvich, G. V. Karachevtsev, V. N. Kondrat'ev, Yu. A. Lebedev, V. K. Medvedev, V. K. Potapov, and Yu. S. Khodeev, *Energy of Chemical Bond Rupture, Ionization Potentials and Electron Affinity* (Nauka, Moscow, 1974) [in Russian].
12. A. V. Eletskiĭ and B. M. Smirnov, Usp. Fiz. Nauk **165**, 977 (1995) [Phys. Usp. **38**, 935 (1995)].
13. A. S. Sonin, *Introduction to Physics of Liquid Crystals* (Nauka, Moscow, 1983) [in Russian].
14. *Quantum Radio Physics: Student's Manual*, Ed. by V. I. Chizhik (St. Petersburg State University, St. Petersburg, 2004) [in Russian].

Translated by P. Pozdeev

A Mathematical Model
of Thermoelectronic Laser Energy Conversion
in Moving Plasma

I. V. Alekseeva, A. P. Budnik, V. A. Zherebtsov, and A. V. Zrodnikov*

*Leipunsky Institute of Physics and Power Engineering, State Scientific Center of the Russian Federation,
Obninsk, Russia*
* *e-mail: avzrod@ippe.obninsk.ru*
Received January 13, 2005

Abstract—A theoretical model of the continuous optical discharge (COD) in plasma moving in the interelectrode space of a thermoelectronic laser energy converter has been developed. Using this model, the COD has been mathematically modeled with allowance for the energy and particle transfer in nonequilibrium near-electrode layers. © 2005 Pleiades Publishing, Inc.

First successful experimental investigations [1] of the process of thermoelectronic laser energy conversion [2] stimulated the passage from simplified engineering calculations of the energy characteristics of such a converter [1, 3] to the development of the general theory of this method. This theory describes the structure of a continuous optical discharge (COD), the interaction of discharge plasma with electrodes, the propagation of laser radiation in this plasma, and the intrinsic radiation transfer in the plasma. To the present, the theory of the thermoelectronic laser energy conversion has been developed only for the stationary COD in immobile gases [4–6].

This Letter describes a theoretical model and its application to simulation of the process of laser energy conversion in the COD in a moving plasma. The use of converters with plasma moving along the interelectrode gap makes it possible to stabilize the discharge, to increase its length, to increase the proportion of the laser beam energy deposited in the discharge, and to construct ac current generators [1].

Discharge model. We consider a symmetric axial thermoelectronic laser energy converter with a hot inner electrode (emitter) of external radius r_1 and a relatively cold outer electrode (collector) of internal radius r_2. The COD is maintained by a weakly focused beam of laser radiation with a wavelength λ_L propagating along the symmetry axis z. The discharge can be shifted in the interelectrode gap, and a gas can be purged through this space. According to [4, 5], the COD can be conditionally divided into three main parts representing the equilibrium core and two nonequilibrium near-electrode regions.

COD core. The equilibrium discharge plasma is described by the continuity equation, the Navier–Stokes equation, and the plasma energy balance equa-

tion (see, e.g., [5, 7]). Here, we write only the energy balance equation, which takes into account the heating of plasma and the energy transfer with the electron current:

$$
\rho c_p \frac{\partial T}{\partial t} + \rho c_p \mathbf{v} \nabla T = \nabla(\lambda \nabla T) + \frac{eJ^2}{nu_e}
$$
$$
- \mathbf{J}\left[\frac{3}{2}\nabla T + T\nabla k_e^{(T)} - T\nabla(\ln n)\right] + W_L - Q, \tag{1}
$$

where t is the time; ρ, T, $\mathbf{v}$, λ, and η are the density, temperature, velocity, thermal conductivity, and dynamic viscosity of the plasma, respectively; c_p is the specific heat at a constant pressure; e is the elementary (electron) charge; $\mathbf{J}$ is the electron flux density; u_e is the electron mobility; n is the number density of electrons (ions); $k_e^{(T)}$ is the thermal diffusion ratio for electrons; W_L is the specific laser power deposited in the plasma; and Q is the specific power lost in the plasma as a result of the intrinsic radiation and absorption. In order to determine the electron flux density and the electric field potential, the system of gasdynamic equations is supplemented by the equations of continuity and motion for electrons. The intrinsic radiation transfer in the plasma can be described in the group diffusion approximation, and the laser beam interaction with the discharge plasma can be described using a parabolic equation for the complex field amplitude [5].

Boundary conditions on interfaces between the COD core and near-electrode regions. In order to study the energy and particle transfer in nonequilibrium near-electrode layers and formulate the boundary conditions for interfaces between the COD core and near-electrode regions under the conditions of COD moving

in the interelectrode gap and a gas purged along this gap, it is necessary to use the equations of continuity, motion, and energy conservation for electrons, ions, and atoms with the known boundary conditions for the particle and energy flows on the electrodes and the conditions of equilibrium for the aforementioned interfaces. The electron and ion velocities at the electrode obey the sticking condition, while the interfaces between the COD core and the near-electrode regions meet the conditions of matching for the velocity and its derivatives. Thin near-electrode regions are considered flat [5, 8].

For the x axis directed toward the plasma along the normal to the electrode surface, the energy balance equation at the boundary between the COD core and the near-electrode regions can be written as

$$-\lambda_T\left(\frac{dT}{dx}\right)_T = -2J_E(T_T - T_E) + S_{Hx1}$$
$$+ (E_i + 2T_T + e\Delta\varphi_1)(j_{ix1} - j_{ixT})$$

$$-J_{xT}\left[\left(\frac{1}{2} + k_{eT}^{(T)}\right)T_T - e\Delta\varphi_T\right] + \int_0^{L_r}(\mathbf{v}_a\nabla P_a + \mathbf{v}_i\nabla P_i)dx$$

$$-\frac{5}{2}(v_{axT}P_{aT} + v_{ixT}P_{it}) \qquad (2)$$

$$-\frac{\partial}{\partial t}\int_0^{L_r}\left[n\left(E_i + \frac{3}{2}T + \Delta\varphi_1\right) + \frac{3}{2}n_aT\right]dx$$

$$-\frac{\partial}{\partial z}\int_0^{L_r}\left\{\left[-\lambda_e\frac{\partial T_T}{\partial z} - \lambda_H\frac{\partial T}{\partial z} + (E_i + 2T_T + e\Delta\varphi_1)j_{iz}\right]\right.$$
$$\left.+ J_z\left[\left(\frac{1}{2} + k_e^{(T)}\right)T_T - e\varphi\right] + \frac{5}{2}(v_{az}P_a + v_{iz}P_i)\right\}dx,$$

where the quantities with subscripts "1" and "T" refer to plasma at the electrode and at the COD core boundary; J_E is the flux density of electrons emitted from the electrode; T_E is the electrode temperature; T is the temperature of atoms and ions; $\mathbf{S}_H$ is the heat flux density transferred by atoms and ions; E_i is the atomic ionization potential; $\Delta\varphi_1$ and $\Delta\varphi_T$ are the potential jumps in the Langmuir layer and in the near-electrode region, respectively; φ is the electric field potential (electrode potential is zero); $\mathbf{j}_i$ is the ion current density; L_r is the near-electrode region thickness; $\mathbf{v}_a$ and $\mathbf{v}_i$ are the velocities of atoms and ions, respectively; n, n_a and P_i, P_a are the densities and partial pressures of ions and atoms, respectively; and λ_e and λ_H are the thermal conductivities of electrons and heavy particles (atoms and ions),

respectively. The physical meaning of the first five terms of Eq. (2) was considered previously [4, 5]. The other terms describe the nonstationary character of COD and the flow of plasma in the interelectrode gap. For the characteristic case of a stationary COD with weakly ionized plasma in the near-electrode regions and $v_{azT} \ll v_\lambda = (\lambda_{HT}/n_{aT}L_r)(L_D/L_r)$, these terms are small compared to S_{Hx1} and, hence, can be ignored (L_D is the COD length along the z axis).

In addition, for $v_{azT} \ll v_\lambda$ and $v_d = (D_{aT}/L_r)(L_D/L_r)$, the plasma is shifted by a distance much shorter than L_D during the ion diffusion and the heat transfer with atoms and ions going out of the near-electrode region (here, D_a is the ambipolar diffusion coefficient). Then, the particle generation and the particle and energy transfer in the near-electrode regions can be considered as independent of the gas flow. Accordingly, the parameters S_{Hx1}, $j_{ix1} - j_{ixT}$, $\Delta\varphi_1$, and $\Delta\varphi_T$ in Eq. (2) can be described by the expressions for COD in the absence of a purged gas (see [5, 8]). Calculations show that the velocities v_d and v_λ rapidly increase with the temperature T_T and become sufficiently large (above 10 m/s) for $T_T \approx 10$ kK (v_λ is one order of magnitude greater than v_d). For a stationary gas flow in the near-electrode region (where the flow velocity weakly depends on the coordinate z), the plasma velocity at the boundary between the COD core and the near-electrode region is

$$v_{xT} = 0, \quad \left(\frac{\partial v_z}{\partial x}\right)_T = v_{zT}/\eta_{aT}\int_0^{L_r}\frac{dx}{\eta_a}. \qquad (3)$$

Mathematical modeling of the COD plasma motion. The method and algorithm of the numerical solution of the set of equations for the COD core were developed using the method of nonstationary dynamic variables [9]. Figures 1 and 2 show the typical results of mathematical modeling for moving COD plasma in argon flowing at a pressure of 0.5 bar. The plasma was moving in a weakly focused beam (focus length, 1.2 m) of a CO_2 laser. A homogeneous flow of argon at a temperature of 2 kK was supplied at a velocity of 20 cm/s into a coaxial gap with $r_1 = 0.2$ cm, $r_2 = 1.4$ cm, and a length of $z_{max} = 40$ cm. The oncoming cold gas flow bypasses the high-temperature plasma region in the middle of the gap and partly penetrates into this region. As a result, the gas flow velocity in the middle of the gap increases by approximately two orders of magnitude. The gas flow is partly displaced toward the walls. Nevertheless, the flow in the near-wall regions "follows" the bimodal spatial distribution of the temperature in the high-temperature region. This circumstance hinders application of the standard boundary layer theory, which has to be substantially modified for use in the problem under consideration.
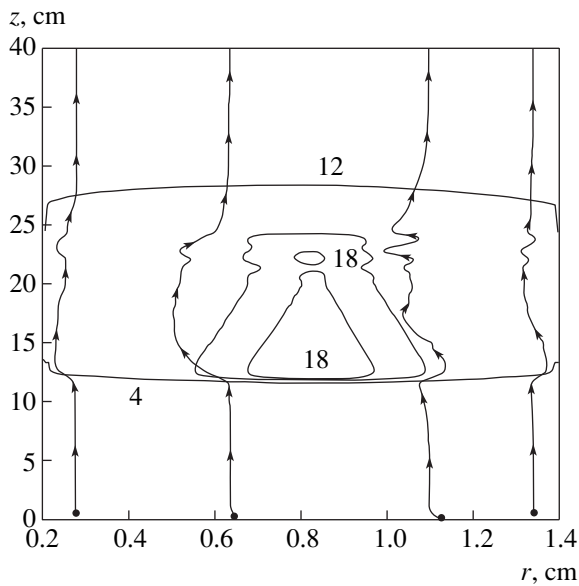
Fig. 1. Current lines and isotherms at $t = 1$ ms numerically calculated for a COD plasma in argon (figures at the curves indicate the temperature in kilokelvins).
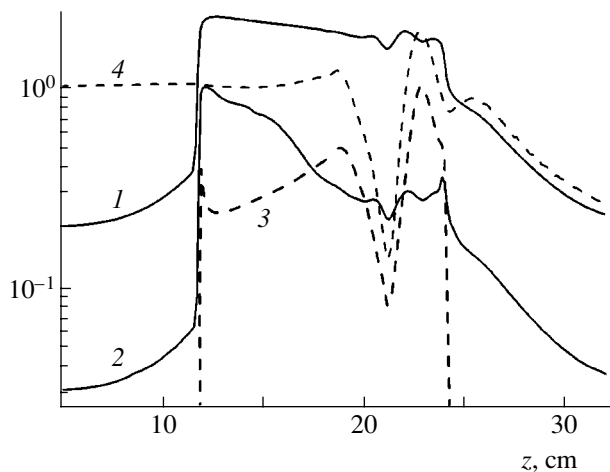
Fig. 2. Profiles of the (*1*) temperature, (*2*) flow velocity, (*3*) specific laser radiation power deposited in the COD, and (*4*) laser radiation intensity along the z axis for fixed $r = (r_1 + r_2)/2$ at the same time as in Fig. 1.

Figure 2 presents the typical longitudinal structure of COD for a fixed $r = (r_1 + r_2)/2$ at a time of $t = 0.84$ ms. The temperature is expressed in kilokelvins,

while the other variables are normalized to their maximum values: $v_{z_{max}} = 18.6$ m/s; $W_{L\,max} = 56$ kW/cm^3, and $I_0 = 4.8 \times 10^5$ W/cm^2 (I_0 is the maximum laser beam intensity at the input). At a large laser beam power (hundreds of kilowatts), a channel in which the electron density is reduced as compared to that in the surrounding plasma is formed in the middle of the interelectrode gap. For this reason, the laser beam exhibits partial self-focusing that leads to the appearance of several local maxima in the temperature profile along the z axis.

Thus, we have developed for the first time a theoretical model and applied it to numerical modeling of the COD in plasma moving in the interelectrode space of a thermoelectronic laser energy converter.

REFERENCES

1. N. P. Kozlov, A. V. Pekshev, Yu. S. Protasov, and V. I. Suslov, *Radiation Plasmadynamics* (Énergoatomizdat, Moscow, 1991), Vol. 1, pp. 462–498 [in Russian].

2. N. S. Rasor, in *Laser-Energy Conversion Symposium of NASA Ames Research Center*, NASA TM X-62, pp. 51–62.

3. E. J. Britt, in *Proceedings of the 3rd NASA Conference on Radiation Energy Conversion in Space, New York, 1978*, pp. 421–436.

4. I. V. Alekseeva, A. P. Budnik, V. A. Zherebtsov, *et al.*, Pis'ma Zh. Tekh. Fiz. **25** (7), 90 (1999) [Tech. Phys. Lett. **25**, 290 (1999)].

5. I. V. Alekseeva, A. P. Budnik, P. P. D'yachenko, *et al.*, Zh. Tekh. Fiz. **70** (11), 91 (2000) [Tech. Phys. **45**, 1462 (2000)].

6. A. P. Budnik and V. A. Zherebtsov, Zh. Tekh. Fiz. **71** (6), 60 (2001) [Tech. Phys. **46**, 704 (2001)].

7. S. T. Surzhikov, Kvantovaya Élektron. (Moscow) **30**, 416 (2000).

8. V. A. Zherebtsov, Teplofiz. Vys. Temp. **42**, 689 (2004).

9. S. T. Surzhikov, Mat. Model. **7** (8), 3 (1995).

Translated by P. Pozdeev

Tunneling of Spin-Polarized Charge Carriers in La$_{0.8}$Ag$_{0.1}$MnO$_{3 + \delta}$ Film with Variant Structure: Magnetotransport and Magnetooptical Data

Yu. P. Sukhorukov*, A. V. Telegin, E. A. Gan'shina, N. N. Loshkareva, A. R. Kaul',
O. Yu. Gorbenko, E. V. Mostovshchikova, O. V. Mel'nikov, and A. N. Vinogradov

Institute of Metal Physics, Ural Division, Russian Academy of Sciences, Yekaterinburg, 620041 Russia
Moscow State University, Moscow, 119899 Russia
* e-mail: suhorukov@imp.uran.ru
Received January 27, 2005

Abstract—Epitaxial La$_{0.8}$Ag$_{0.1}$MnO$_{3 + \delta}$ film with variant structure on ZrO$_2$(Y$_2$O$_3$) substrate was grown for the first time, and the optical, magnetooptical, and transport properties of this film were studied in order to elucidate special features in the mechanism of conductivity and magnetoresistance (*MR*) in this film. An original method has been developed for separating the *MR* contributions related to the colossal *MR* near T_C and the tunneling *MR* component. This method is based on the comparative analysis of data on the *MR* and the IR magnetotransmission of the film. It is established that the tunneling *MR* component is related to the large-angle boundaries of structural domains and its temperature dependence is described by the function $\Delta\rho/\rho \sim (a + b/\sqrt{T})$. The degree of spin polarization of charge carriers in the La$_{0.8}$Ag$_{0.1}$MnO$_{3 + \delta}$ film with variant structure amounts to $P \sim 0.5$. © *2005 Pleiades Publishing, Inc.*

The problem of increasing the properties of manganites exhibiting colossal magnetoresistance (*CMR*) near the Curie temperature (T_C) can be solved by selecting appropriate doping elements capable of increasing T_C and improving the magnetotransport properties of the material. In particular, the doping of LaMnO$_3$ with monovalent ions of Na and Ag leads to an increase in the magnetoresistance (*MR*) and T_C [1–6]. Recently, it was established that polycrystalline La$_{1 - x}$Ag$_x$MnO$_3$ samples are characterized by an additional *MR* component due to the tunneling of spin-polarized electrons (TSPEMR) [1–5]. This contribution exhibits nonlinear growth with decreasing temperature in the ferromagnetic state and tends to a maximum at $T \sim 0$. At $T = 80$ K, the tunneling *MR* component in a composition with $x_{Ag} = 0.165$ in a magnetic field of ~1 T reaches 20% [2].

In recent years, the nature of the magnetoresistance in La$_{1 - x}$Ag$_x$MnO$_3$ manganites has been extensively studied [1–5], but the results reported in various papers for polycrystalline samples are rather contradictory. No data are available on the optical and magnetooptical properties of compounds of the La$_{1 - x}$Ag$_x$MnO$_3$ system. This study was performed on a 760-nm-thick epitaxial La$_{0.8}$Ag$_{0.1}$MnO$_{3 + \delta}$ film grown for the first time by metalorganic chemical vapor deposition (MOCVD) using an original two-step procedure described elsewhere [1, 4]. A special feature of this film, grown on an (001)-oriented single crystal ZrO$_2$(Y$_2$O$_3$) substrate ($a =$

0.514 nm), is the presence of large-angle (19.5°, 70.5°, and 90°) boundaries in the (110) plane of the film, which is related to the growth of azimuthal structural variants (equivalent or variant structure) with like grains representing structural domains with dimensions of 30–40 nm [7]. The set of angular orientations of such large-angle boundaries is strictly fixed, and their concentration does not vary in depth of the film. This is a substantial difference of the variant structures from usual polycrystalline materials. In films grown on the ZrO$_2$(Y$_2$O$_3$) substrate, the formation of a variant structure leads to the appearance of highly conducting ferromagnetic (FM) nanodimensional regions separated by ~0.4-nm large-angle boundaries [8]. This microstructure makes possible the new mechanisms of conductivity with different contributions to the magnetoresistance, including temperature-independent and -dependent *MR* components related to the tunneling (or hopping) of charge carriers between nanograins [9]. Important information for separating these contributions can be provided by optical investigations in the range of the interaction of light with charge carriers.

This Letter presents the results of a comparative study of the optical, magnetooptical, and transport properties of the La$_{0.8}$Ag$_{0.1}$MnO$_{3 + \delta}$ film with variant structure. These data are analyzed in order to reveal peculiarities in the mechanisms of conductivity and magnetoresistance in this material.

The results of electron-probe microanalysis and X-ray diffraction measurements indicate that silver atoms partly occupy the vacancies of lanthanum ($x < y$). The data of X-ray photoelectron spectroscopy showed the absence of metal silver in the film. According to the X-ray diffraction data, the $La_{0.8}Ag_{0.1}MnO_{3+\delta}$ (LAMO) film has an epitaxial rhombohedral perovskite structure. The optical properties of the film were studied on a highly sensitive prism spectrometer in a wavelength range $1 \mu m \le \lambda \le 10 \mu m$ at temperatures from 80 to 350 K and in magnetic fields of up to $H = 10$ kOe. The resistivity ρ was measured in the same temperature range (80–350 K) in magnetic fields of up to 10 kOe. The transversal Kerr effect δ was studied in the energy interval $1.5 eV < E < 4.2 eV$ for fields up to 3.5 kOe and temperatures up to 350 K.

The obtained temperature and field dependences of the Kerr effect (Fig. 1) showed that the LAMO film passes to the FM state at $T_C^* = 312$ K and is a soft ferromagnet with a coercive force of $H_c \cong 50$ Oe at 300 K. As the temperature decreases, the H_c value slightly grows. The effective Curie temperature T_C^* was determined by extrapolating the $\delta(T)$ curve to intersection with the abscissa axis. The shape of the $\delta(E)$ curves is generally the same as that observed for the manganites doped with divalent Sr^{2+} and Ca^{2+} ions and for nonstoichiometric manganites [12–18]. However, the magnitude of the Kerr effect at low temperatures was lower, while the width of the main maximum at ~2.7 eV was greater than in the other optimum-doped manganites [10, 11]. This behavior of the Kerr effect indicates that the FM phase in the Ag-doped film with variant structure is different from the metallic FM phase in the manganites doped with Sr^{2+} and Ca^{2+} ions, which is probably related to a more pronounced magnetic and structural inhomogeneity of the Ag-containing film.

Previously, we have demonstrated [6, 12–18] that the temperature-dependent variation of the IR transmission (I) in optimum-doped lanthanum manganites near T_C is analogous to the temperature dependence of the resistivity $\rho(T)$. In the case of weak doping, whereby the FM phase content is insignificant and the $\rho(T)$ behavior is semiconductor like, the metal–insulator (MI) transition in the $I(T)$ curve indicates the presence of regions with metallic conductivity. For the LAMO film with variant structure (see the inset in Fig. 2a), the $\rho(T)$ curve shows a smeared MI transition (with a maximum resistance at $T_\rho = 250$ K) and exhibits an anomaly at 307 K in the semiconductor branch of $\rho(T)$. In the temperature dependence of the optical transmission (see the inset in Fig. 2b), a transition to the "metallic" character of transmission is observed at $T_I = 312$ K (bending point on the $I(T)$ curve), which coincides with T_C^* and is close to the position of the anomaly (307 K) in $\rho(T)$. A difference in the behavior of $I(T)$ and $\rho(T)$ is
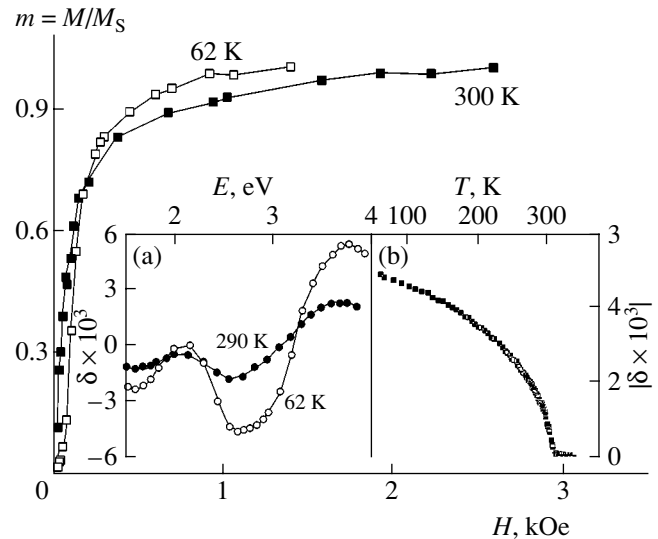

Fig. 1. Field dependences of the relative magnetization $m = M/M_S$ of the LAMO film with variant structure at different temperatures in the magnetic field parallel to the film surface. The inset shows (a) the spectrum and (b) the temperature dependence of the transversal Kerr effect δ at $H = 3.5$ kOe and $E = 2.7$ eV.

indicative of a complex character of conductivity in our LAMO film with variant structure.

In polycrystalline manganites doped with silver [3], the presence of anomalies in the $\rho(T)$ curve for $x_{Ag} = 0.1$ was explained by the interplay of two contributions to the conductivity: (i) a component due to the bulk conductivity with $T_C = 302$ K and (ii) a component due to the spin-polarized electron tunneling through grain boundaries with a low silver content and $T_C = 250$ K. The latter contribution may reach up to several tens of percents [4]. In our case, the through conductivity via boundaries of the structural domains in the bulk of the film appears only at $T \sim 250$ K (see the inset in Fig. 2a). The delayed decay in the $\rho(T)$ curve at $T < 250$ K for the LAMO film is probably related to the charge carrier scattering on large-angle domain boundaries at low temperatures. At the same time, the formation of metallic FM regions in the film takes place near T_C, which is confirmed by the temperature dependence of the optical transmission with $T_I = 312$ K and by a weak anomaly in $\rho(T)$ at 307 K. It should be emphasized that the contribution to conductivity due to the grain boundaries is not manifested in the optical absorption. Thus, a comparison of the optical and electrical characteristics allows us to separate the two contributions to the conductivity. A difference in the character of conductivity in the film with variant structure is most clearly pronounced in the temperature dependences of the magnetoresistance $MR = (\rho_H - \rho_0)/\rho_0 = \Delta\rho/\rho_0$ and the magnetotransmission $MT = (I_H - I_0)/I_0$.

The results of investigations of a large number of epitaxial films of lanthanum manganites showed that
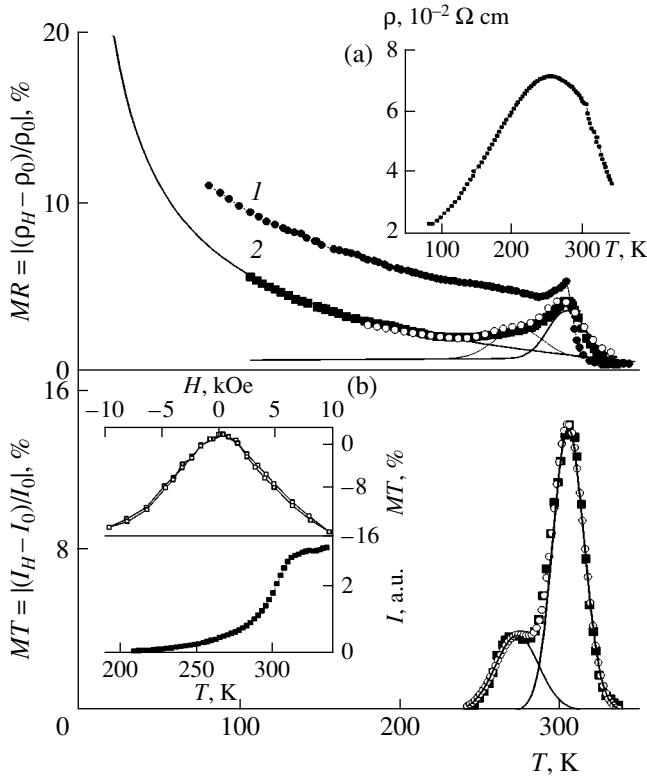
Fig. 2. (a) Temperature dependences of the magnetoresistance *MR* of the LAMO film at $H = 4$ kOe for the field oriented (*1*) along and (*2*) perpendicularly to the film surface. Black circles represent experimental points; open circles show the curve obtained by fitting to experiment; solid curves correspond to the Gaussian and the $f = a + b/\sqrt{T}$ functions (see text); the inset shows the temperature dependence of the resistivity ρ; (b) the temperature dependence of the magnetotransmission *MT* at $H = 4$ kOe (squares represent experimental points, open circles show the curve obtained by fitting two Gaussians to experiment); the inset shows the field dependence of the *MT* at $T = 304$ K (top panel) and the temperature dependence of the optical transmission *I* at $\lambda = 6$ μm (bottom panel).

the magnetotransmission takes place only in the vicinity of T_C [11, 12–14, 18]. The *MT* is a high-frequency analog of *CMR* related to the formation of metallic FM regions upon the transition from para- to ferromagnetic state. The temperature intervals of the existence of *MT* and *CMR* coincide. However, as can be seen from Fig. 2, the *MT* vanishes at $T < 240$ K, whereas the *MR*(*T*) exhibits growth related to the tunneling *MR* component. The presence of two maxima in the *MT*(*T*) curve measured at $\lambda = 6$ μm and $H = 8$ kOe (Fig. 2b) is indicative of the existence of two metallic FM phases with different T_C (312 and 274 K). We may suggest that the main phase with higher T_C is related to the doping of $La_{1-x}MnO_3$ with Ag^+ ions, while the phase with lower T_C corresponds to undoped $La_{1-x}MnO_3$. Since the domain size is much (about ten times) smaller than the film thickness, it is unlikely that the pure $La_{1-x}MnO_3$ phase is retained inside the domains: if it

were so, this phase would also be predominant in the bulk of the film. Presumably, this phase is present only in a region at the film–substrate boundary, in which the penetration of Ag ions can be hindered by epitaxial stresses. It is also possible that this phase is formed at the boundaries between structural domains and has T_C close to the Curie temperature of $La_{0.83}MnO_3$ [12]. Further elucidation of this question requires the use of chemical profiling techniques.

We have analyzed the shapes of *MR*(*T*) curves taking into account that the *MR* near T_C is analogous to *CMR* and using data on the temperatures of *MT* maxima (T_{MT}^{max}) determined from the *MT*(*T*) curves and the half-widths of the analytical Gaussian curves fitting to experiment. At high temperatures, the *MR*(*T*) curve corresponds to the *CMR* behavior (Fig. 2a) determined by the contributions from two magnetic phases manifested in the *MT*(*T*) curve (Fig. 2b). The *MR* growth at $T <$ 250 K is due to TSPEMR and can be described by the function

$$\Delta\rho/\rho_0 = a + b/\sqrt{T}, \tag{1}$$

where $a = 0.02$ is a constant independent of the temperature, and $b \sim 30$ K$^{1/2}$ for the field oriented parallel to the film plane and ~ 100 K$^{1/2}$ for the field oriented in the normal direction. It should be noted that relation (1) differs from the expression $f = a + b/(T + c)$ valid for polycrystalline $La_{2/3}Sr_{1/3}MnO_3$ [19] and from the expression $\Delta\rho/\rho = -(JP/4k_BT)[m^2(H, T) - m^2(H, 0)]$ for TSPEMR in granular metallic FM films (where *J* is the exchange interaction constant, *P* is the degree of spin polarization, and *m* is the relative magnetization normalized to the saturation value) [9, 20, 21].

Function (1) depends on the temperature in the same way as the function describing the *MR* component due to the correlated tunneling of spin-polarized electrons between large grains through the sequences of much smaller grains [9, 22] ordered into parallel chains:

$$\Delta\rho/\rho_0 \approx -P^2m^2(1 + \sqrt{(C/T)}). \tag{2}$$

Here, *C* is a constant dependent on the excess Coulomb energy gained upon electron charging of a small grain in the chain and on the tunneling barrier parameters. Apparently, this type of temperature dependence more corresponds to the ordered variant structure of our film than to a usual ceramic material [19]. For the LAMO film, extrapolation of the *MR*(*T*) curve to intersection with the ordinate axis indicates that the TSPEMR contribution reaches 60% at $T = 0$ K. This value is close to the TSPEMR contribution ($\sim$50%) reported for polycrystalline LAMO samples [3]. Using the TSPEMR contribution estimated by extrapolation to $T = 0$ K, we have also evaluated the degree of electron spin polarization from the relation $\Delta\rho/\rho_0 = 2P^2/(1 - P^2)$ [9]. For the LAMO film with variant structure, this yields $P \sim 0.5$.

$MR = |(\rho_H - \rho_0)/\rho_0|,\ \%$

85 K

295 K

H, kOe
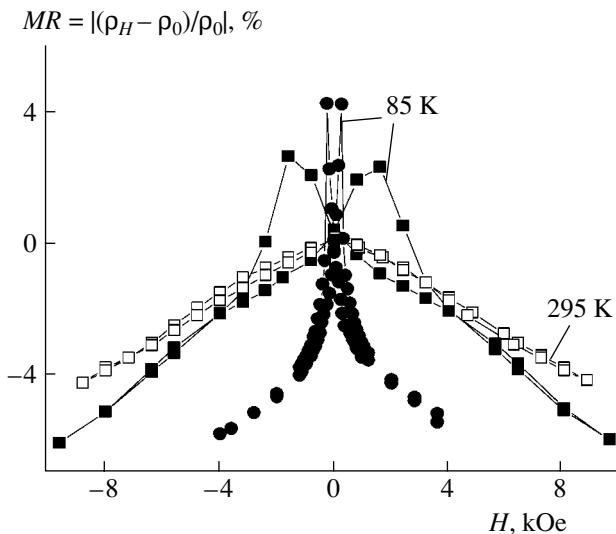
Fig. 3. Plots of the magnetoresistance *MR* versus magnetic field *H* oriented parallel (circles) and perpendicular (squares) to the LAMO film surface.

A difference in the behavior of *CMR* and tunneling *MR* component as functions of the magnetic field is illustrated in Fig. 3. In the temperature interval 280 K < *T* < 320 K, both *MR* and *MT* exhibit monotonic increase with the magnetic field strength (see Fig. 3 and the inset in Fig. 2b), weakly depend on the field orientation (parallel against perpendicular) relative to the film plane, and exhibit no hysteresis, which is related to the maximum fluctuations of magnetic moments near T_C. At *T* ~ 80 K, the field dependence of the TSPEMR contribution is substantially nonmonotonic, shows a hysteresis, and depends on the magnetic field orientation relative to the film plane (Fig. 3). The coercive force is H_c = 1.6 kOe for the film magnetized in the perpendicular direction and 250 Oe, for the in-plane magnetization. The coercive force was determined as a half-spacing between the *MR*(*H*) maxima, by analogy with the case of a $La_{0.67}Sr_{0.33}MnO_3/TB/La_{0.67}Sr_{0.33}MnO_3$ structure with a 4.4-nm-thick $SrTiO_3$ tunneling barrier (TB) [9]. A lower H_c value for the in-plane magnetization is indicative of the predominantly in-plane anisotropy of TSPEMR. A high positive value of *MR* ~ 4% observed for an in-plane field of 250 Oe can be used in practical applications. Note that a hysteresis in the TSPEMR contribution appears at *T* < 200 K and is determined by the variant structure of our LAMO film. The magnetotransmission *MT* of the $La_{0.8}Ag_{0.1}MnO_{3+\delta}$ film with variant structure reaches a maximum in the wavelength range of λ ~ 2–4 μm at *T* = 307 K and *H* = 8 kOe. The colossal magnitude of *MR* ~ 22%, together with a giant value of the TSPEMR contribution, can also find practical use.

REFERENCES

1. O. Yu. Gorbenko, O. V. Melnikov, A. R. Kaul, *et al.*, Chem. Mat. (2005) (in press).
2. S. L. Ye, W. H. Song, J. M. Dai, *et al.*, J. Magn. Magn. Mater. **248**, 26 (2002).
3. L. Pi, M. Hervieu, A. Maignan, *et al.*, Solid State Commun. **126**, 229 (2003).
4. O. Yu. Gorbenko, O. V. Melnikov, A. R. Kaul, *et al.*, Mater. Sci. Eng., B (2005) (in press).
5. T. Tang, Q. Q. Cao, K. M. Gu, *et al.*, Appl. Phys. Lett. **77**, 723 (2000).
6. Yu. P. Sukhorukov, N. N. Loshkareva, A. V. Telegin, *et al.*, Pis'ma Zh. Tekh. Fiz. **29** (21), 55 (2003) [Tech. Phys. Lett. **29**, 904 (2003)].
7. A. R. Kaul', O. Yu. Gorbenko, and A. A. Kamenev, Usp. Khim. **73**, 932 (2004).
8. O. Yu. Gorbenko, R. V. Demin, A. R. Kaul', *et al.*, Fiz. Tverd. Tela (St. Petersburg) **40**, 290 (1998) [Phys. Solid State **40**, 263 (1998)].
9. M. Ziese, Rep. Prog. Phys. **65**, 143 (2002).
10. E. A. Balykina, E. A. Gan'shina, G. S. Krinchik, *et al.*, J. Magn. Magn. Mater. **117**, 259 (1992).
11. E. A. Gan'shina, I. K. Rodin, N. N. Loshkareva, *et al.*, Izv. Akad. Nauk, Ser. Fiz. **66**, 767 (2002).
12. Yu. P. Sukhorukov, N. N. Loshkareva, E. A. Gan'shina, *et al.*, Zh. Éksp. Teor. Fiz. **123**, 293 (2003) [JETP **96**, 257 (2003)].
13. Yu. P. Sukhorukov, N. N. Loshkareva, E. A. Gan'shina, *et al.*, Fiz. Tverd. Tela (St. Petersburg) **46**, 1203 (2004) [Phys. Solid State **46**, 1241 (2004)].
14. Yu. P. Sukhorukov, E. A. Gan'shina, B. I. Belevtsev, *et al.*, J. Appl. Phys. **91**, 4403 (2002).
15. E. A. Gan'shina, H. V. Vashuk, A. N. Vinogradov, *et al.*, in *Proceedings of the 2nd Euro-Asian Symposium "Trends in Magnetism" (EASTMAG-2004), Krasnoyarsk, 2004*, p. 231.
16. N. N. Loshkareva, N. I. Solin, Yu. P. Sukhorukov, *et al.*, Physica B **293**, 390 (2001).
17. N. N. Loshkareva, Yu. P. Sukhorukov, S. V. Naumov, *et al.*, Pis'ma Zh. Éksp. Teor. Fiz. **68**, 89 (1998) [JETP Lett. **68**, 97 (1998)].
18. Yu. P. Sukhorukov, A. P. Nossov, N. N. Loshkareva, *et al.*, J. Appl. Phys. **97**, 103710 (2005).
19. H. Y. Hwang, S.-M. Cheong, N. P. Ong, and B. Batlogg, Phys. Rev. Lett. **77**, 2041 (1996).
20. J. S. Helman and B. Abeles, Phys. Rev. Lett. **37**, 1429 (1976).
21. J. I. Gittleman, Y. Goldsrein, and S. Bozowski, Phys. Rev. B **5**, 3609 (1972).
22. S. Mitani, S. Takanashi, K. Yakushiji, *et al.*, Phys. Rev. Lett. **81**, 2799 (1998).

Translated by P. Pozdeev

Regeneration of Graphite Explosive-Emission Cathodes Operating at High Repetition Rates of Nanosecond Accelerating Pulses

S. D. Korovin*, S. K. Lyubutin, E. A. Litvinov, G. A. Mesyats**, A. M. Murzakaev,
V. V. Rostov, S. N. Rukin, B. G. Slovikovsky, M. R. Ul'maskulov, K. A. Sharypov,
V. G. Shpak, S. A. Shunailov, and M. I. Yalandin***

Institute of High-Current Electronics, Siberian Division, Russian Academy of Sciences, Tomsk, 634055 Russia

Institute of Electrophysics, Ural Division, Russian Academy of Sciences, Yekaterinburg, 620219 Russia

Lebedev Institute of Physics, Russian Academy of Sciences, Moscow, 117924 Russia

e-mail: * korovin@hcei.tsc.ru; ** mesyats@pran.ru; *** yalandin@iep.uran.ru

Received February 8, 2005

Abstract—We have experimentally studied the possibility of increasing the working life of explosive-emission cathodes operating at high repetition frequencies (several kilohertz) of nanosecond accelerating voltage pulses. Micrographs of the cathode surface upon training, photographs of the operating cathode, and analyses of the material carried away from the cathode showed that a substantial role in the cathode degradation is played by heating of some regions of the emissive edge up to a temperature of graphite melting. © 2005 Pleiades Publishing, Inc.

Previously [1], we described the pattern of changes in the characteristics of a graphite explosive-emission tubular sharp-edge cathode in a coaxial magnetically insulated vacuum diode under the action of accelerating voltage pulses (Fig. 1) with a full width at half maximum (FWHM) of ~1.5 ns, an amplitude of –280 kV, and a repetition frequency within $F = 1$–3.5 kHz. The cathode training at $F \leq 1$ kHz was accompanied by degradation of the emission characteristics, while the passage to a regime with $F = 3.5$ kHz led to the restoration of these characteristics. In the latter case, the micrographs of the cathode edge showed evidence of homogenization of the material surface, which appeared much like that upon melting. Evaluation of the temperature regime in the vicinity of an individual center of the explosive electron emission showed that the period $\tau > 1$ ms between voltage pulses is sufficient for the emission zone to cool down to 300 K, whereas the pulses arriving at $\tau \approx 300$ μs ($F \approx 3$ kHz) keep the zone at a residual heating to ~800–900 K [1]. Based on these experimental data and calculations, it was suggested that the phenomenon of polishing of the surface of explosive-emission cathodes under the action of short voltage pulses at small repetition rates [2] has a certain frequency threshold.

The aim of this experimental investigation was to elucidate the mechanism of regeneration of the cathode emissivity, which is apparently explained by a significant contribution of thermionic emission to the explosive electron emission initiated by residual heat in the regions not cooled during the period of time between

pulses. Since this hypothesis is related to the increasing heating and probably melting of graphite, we have tried to determine the spatial location of individual explosive emission zones and to find fused graphite particles in sprayed products of the cathode material.

Taking into account the phenomenon of the cathode surface screening by the space charge of electrons emitted from the leading centers [3] and using the estimates obtained previously [1], we may suggest that the num-
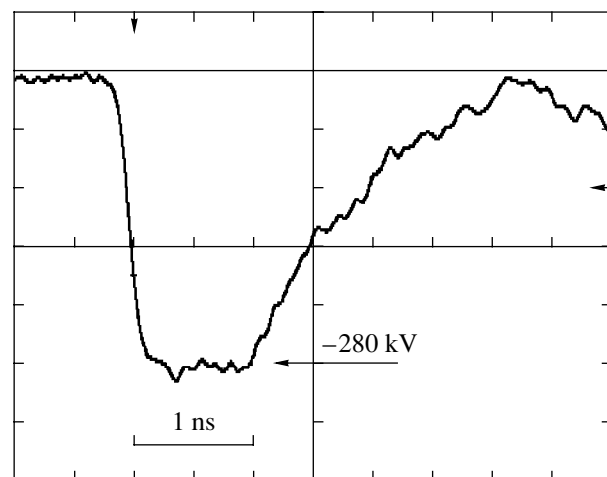
Fig. 1. The typical oscillogram of an accelerating voltage pulse with a full width at half maximum ~1.5 ns, a leading front width of ~200 ps, and an amplitude of –280 kV (measured with 6-GHz Tektronix TDS 6604 at 20 G/s).
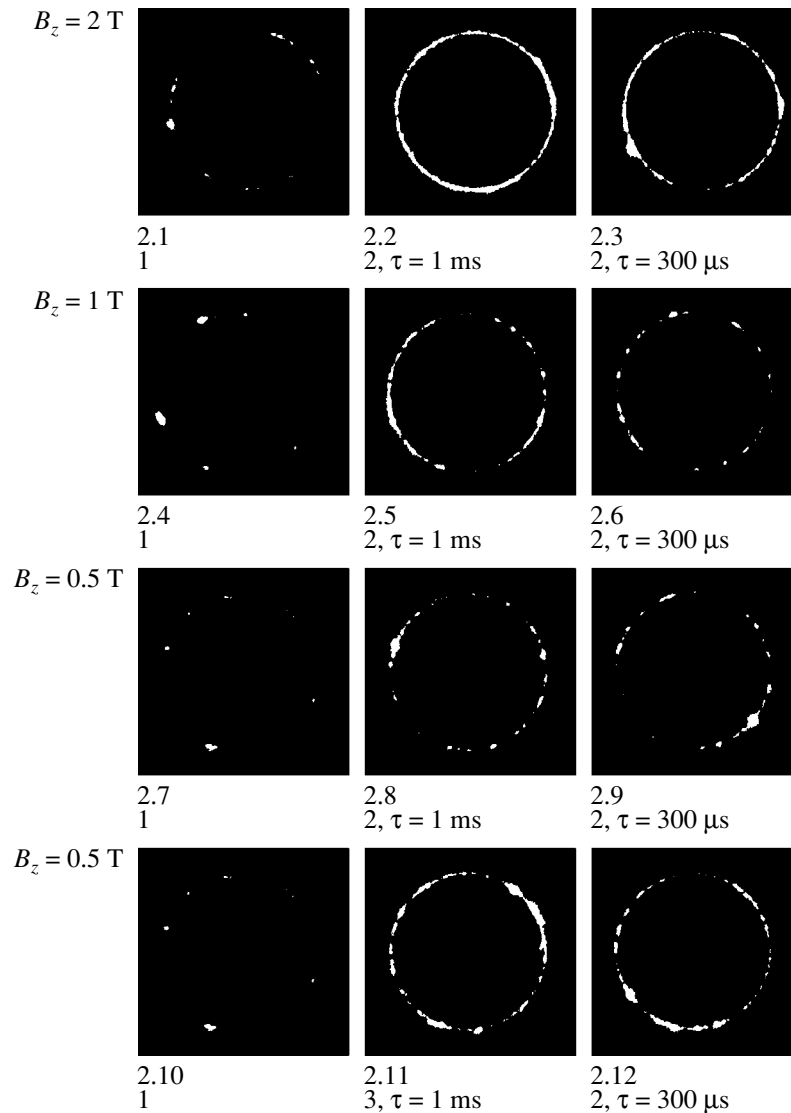
Fig. 2. A series of photographs of the emissive edge of a tubular graphite cathode with an outer diameter of 8.6 mm. The shots were made with an open shutter for various values of the magnetic induction (B_z = 0.5–2 T), the number of voltage pulses (from 1 to 3), and the interval between pulses (τ = 1 ms or 300 μs).

ber of explosive emission zones at the cathode edge varies (depending on the magnetic field strength) from several units to several tens. For this reason, the spatial location of the individual explosive emission zones in the regime with $F \approx 3$ kHz (but not at $F \approx 1$ kHz) must be confirmed by photographs of the operating cathode edge made with an open camera shutter in the regime of accumulation of the same number of shots. These experiments were performed on a setup described previously [1] at the same parameters of accelerating pulses (Fig. 1) and a beam current of ~2 kA. The explosive-emission tubular sharp-edge cathode with a diameter of 8.6 mm and an emitting edge radial size of ~150 μm was made of MPG-6 grade graphite. The residual pressure in the coaxial magnetically insulated vacuum diode was on a level of 10^{-4} Torr. Prior to the photographic monitoring, the cathode was trained

using a total of ~2300 pulse trains with repetition frequencies within 100–3000 Hz. According to [4], this training is sufficient to clean the surface layers from adsorbed molecules and technological contaminations.

The emissive edge was photographed in the regimes of cathode operation with intervals τ = 1 ms and 300 μs and the number of pulses N_p = 1, 2 or 3 (Fig. 2). A further increase in N_p in the absence of special optical filters led to excessive background exposure, which hindered comparison of the photographs. The focusing magnetic field in the diode was varied within 0.5–2 T. The obtained negatives were analyzed by means of transmission scanning, with all shots processed in the identical regime of image contrast enhancement in order to reveal the bright spots of cathode plasma torches and compare their numbers.
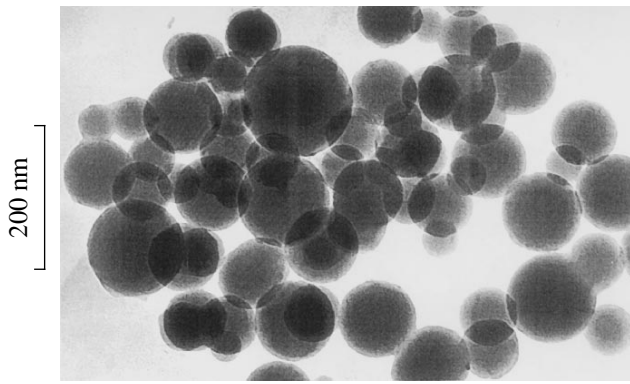
Fig. 3. Electron micrographs of graphite nanoparticles having the shape of fused spherical droplets.

Examination of the series of shots (2.7 ⟶ 2.4 ⟶ 2.1), (2.8 ⟶ 2.5 ⟶ 2.2), and (2.9 ⟶ 2.6 ⟶ 2.3) in Fig. 2 shows that an increase in the magnetic induction is accompanied by growth in the number of emission centers, in accordance with the screening effect. A comparison of the pairs of shots (2.2 ⟶ 2.3), (2.5 ⟶ 2.6), (2.8 ⟶ 2.9), and (2.11 ⟶ 2.12) shows that the number of emission centers appearing for the same magnetic field and an equal number of pulses (2 or 3) decreases when the repetition period is reduced from 1 ms to 300 μs. It is important to note that, for $\tau = 300$ μs, the number of observed plasma torches in the case of two or three pulses is greater than their number for $N_p = 1$. This implies that new emission centers are not completely localized in the vicinity of centers formed by the first pulses in the same train. This result is quite explainable, since the emission zone temperature upon application of the first several pulses at $\tau \approx 300$ μs (even if the subsequent emission centers were related to the previous ones) must be about ~1000–2000 K [1]. Although this heating already distinguishes the given emission zone on the background of surrounding "cold" graphite, the competitive field-emission processes at the "fresh" microinhomogeneities of the cathode surface may proceed in parallel and partly mask the effect of "thermionic" localization of the explosive emission centers.

A more illustrative manifestation of the localization effect is possible in cases involving an increase in the residual temperature of the explosive emission zones. Since the pulse repetition frequency was limited, we may suggest that the effect of localization at $F \approx 3$ kHz must be more pronounced after a relatively large number of sequential pulses in the train. Indeed, according to the estimates obtained in [1], the temperature of an explosive emission zone for $N_p \approx 10$ may reach ~4500 K, which is a prerequisite for graphite melting (in accordance with the phase diagram [5]). In this case, the material carried away from the cathode must contain a fraction of droplets that was found previously in the regime of rare nanosecond pulses applied to a graphite point cathode [6].

In this study, electron-microscopic examination of the sprayed cathode material collected in the gap between the cathode and the collector also revealed a fraction of spherical droplets with a diameter of 30–200 nm (Fig. 3), as well as agglomerates of such droplets and fragments of submicron dimensions. The graphite structure of these products was confirmed by the electron diffraction patterns. The appearance of submicron particles is most probably related to thermomechanical fracture of the electron collector, which was also made of graphite. Estimates show that short pulse trains at a repetition frequency of 3 kHz produce adiabatic heating of the zone of deposition of an annular electron beam with a maximum electron energy of ~300 keV, current density above 10^4 A/cm^2, and a pulse energy ~1 J. A ring deposition zone of the collector can also be heated up to the melting point of graphite, but this would require a number of pulses ten times as great as that necessary for reaching the same temperature within microscopic localization zones near the explosive emission centers on the cathode (in addition, these zones are featuring maximum pressures at the moment of beam injection [6]).

Thus, there are grounds to believe that we have experimentally proved the existence of a frequency threshold for the effect of polishing of the explosive-emission cathodes under the action of short voltage pulses. These results, together with our previous data on cathode training, show the possibility of eliminating degradation of the cathode emissivity under the action of short accelerating pulses at a high repetition rate.

REFERENCES

1. S. D. Korovin, E. A. Litvinov, G. A. Mesyats, *et al.*, Pis'ma Zh. Tekh. Fiz. **30** (19), 30 (2004) [Tech. Phys. Lett. **30**, 813 (2004)].

2. B. Juttner, V. F. Putchkarjov, and W. Rohrbech, in *Proceedings of the 7th International Symposium on Discharges and Electrical Insulation in Vacuum, Novosibirsk, 1976*, pp. 189–192.

3. S. Ya. Belomyttsev, S. D. Korovin, and G. A. Mesyats, Pis'ma Zh. Tekh. Fiz. **6**, 1089 (1980) [Sov. Tech. Phys. Lett. **6**, 466 (1980)].

4. A. V. Gunin, S. D. Korovin, V. F. Landl', *et al.*, Pis'ma Zh. Tekh. Fiz. **25** (22), 84 (1999) [Tech. Phys. Lett. **25**, 922 (1999)].

5. F. P. Bundy and R. H. Wentorf, Nature **176**, 51 (1955).

6. B. A. Koval', D. I. Proskurovsky, V. F. Tregubov, and E. B. Yankelevich, Pis'ma Zh. Tekh. Fiz. **5**, 603 (1979) [Sov. Tech. Phys. Lett. **5**, 246 (1979)].

Translated by P. Pozdeev

X-ray Topography Contrast of Edge Dislocations Perpendicular to the 6H-SiC Crystal Surface

A. O. Okunev[a,*] and I. L. Shul'pina[b,**]

[a] Novgorod State University, Novgorod, 173003 Russia
[b] Ioffe Physicotechnical Institute, Russian Academy of Sciences, St. Petersburg, 194021 Russia
*e-mail: * oao@novsu.ac.ru; ** iren.shulpina@mail.ioffe.ru*
Received February 17, 2005

Abstract—Features of the X-ray topography (XRT) images of edge dislocations perpendicular to the (0001) surface of a 6H-SiC single crystal are described. The contrast of topographs obtained in the regime of anomalous X-ray transmission is compared to the contrast of images obtained using section X-ray topography in the transmission geometry. © 2005 Pleiades Publishing, Inc.
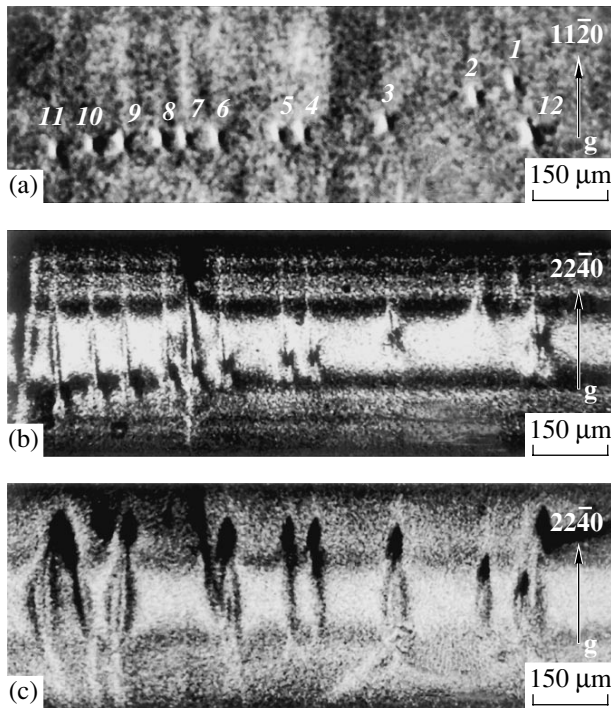
Dislocations emerging at the surface of crystals have been extensively studied using the contrast rosettes observed in X-ray topographs [1]. However, there are still some questions, in particular, concerning the dependence of the contrast on the dislocation line length. Experiments aimed at elucidating this question can be performed on SiC crystals grown by the conventional Lely method. Such crystals contain characteristic dislocations, which initially propagate in the basal plane and then make a 90° turn and emerge from bulk on the crystal surface [3]. Thus, a sample may contain dislocations with straight edge-type segments parallel to the [0001] axis. SiC crystals grown using the Lely method are frequently characterized by a low density of dislocations ($N_d < 10^2$ cm^{-2}). Such crystals can be used in special diffraction experiments devoted to the study of contrast due to individual dislocations.

This investigation was performed on a 6H-SiC single crystal containing a set of dislocations of the same type with the axes changing direction from $[\bar{1}\bar{1}20]$ to [0001] and emerging at the (0001) crystal surface. A special feature of the dislocations under consideration is that their deep portions are virtually parallel to the crystal surface. This circumstance makes the method of section X-ray topography in the transmission geometry very convenient for determining the depth of dislocations [4].

The sample had the shape of a 475-μm-thick plate cut parallel to the basal (0001) plane. First, a series of X-ray topographs were obtained in the regime of anomalous X-ray transmission (AXT) in order to select the crystal orientations for the section transmission topography measurements. The section topographs were obtained for two arrangements: in the first case, the X-ray beam crossed several dislocations in a region where these dislocations were parallel to the crystal surface; in the second case, the beam probed the site

where the dislocations emerge from bulk on the sample surface. The experiments were performed using the conventional laboratory X-ray sources (BSV-10 and BSV-22 tubes). The AXT images were obtained using the Cu$K_{\alpha 1}$ radiation in $11\bar{2}0$-type reflections ($\mu t \approx 6.7$, where μ is the photoelectric absorption coefficient and t is the crystal thickness); the section topographs were obtained using the Mo$K_{\alpha 1}$ radiation in $11\bar{2}0$- and $22\bar{4}0$-type reflections ($\mu t \approx 0.8$); the slit width in front of the crystal was 20 μm. The topographs were recorded on photographic plates with an MR type emulsion for nuclear investigations. The negatives were digitized for data processing with the aid of a MIN-8 microscope and an Olimpus Camedia C-5060 camera.

Figure 1a shows a fragment of the topograph with dislocations imaged in the AXT regime. The segments of dislocations perpendicular to the surface form contrast rosettes characteristic of the edge dislocations [1, 2]. The edge dislocation contrast is a superposition of the contrast from a deep part of the dislocation and the contrast due to stress relaxation on the free crystal surface. The topograph in Fig. 1a displays only four (two dark and two bright) rosette lobes, which are the closest to the dislocation core. These lobes are related to the strain field in depth of the crystal and represent the contrast zone formed due only to the dynamic diffraction effects, whereby specific channeling phenomena take place as a result of variations in the density of the Bloch wave trajectories in the elastic field of the dislocation [5]. The rosette antisymmetry plane coincides with the dislocation slip plane. Black lobes correspond to the region of compression near the extra half-plane (situated to the right from all dislocations), while bright lobes correspond to the region of tensile deformation [1]. All dislocations have the Burgers vector $\mathbf{b} = \frac{a}{3}[11\bar{2}0]$. The deep screw parts of dislocations oriented along the dif-

Fig. 1. Fragments of X-ray topographs showing edge dislocations emerging from bulk on the 6H-SiC crystal surface, (a) image obtained in the anomalous X-ray transmission mode; (b, c) images obtained using section topography experiments in the transmission geometry for the dislocation segments perpendicular and parallel to the crystal surface, respectively.
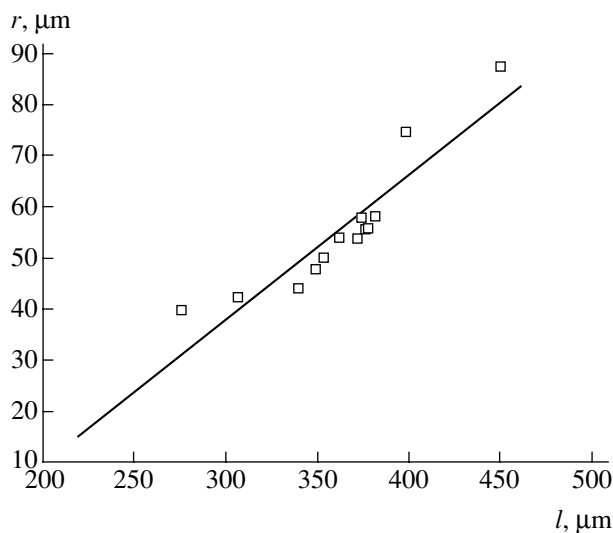
Fig. 2. Experimental plot of the contrast rosette diameter r versus length l of the dislocation line for the edge dislocations in a 6H-SiC crystal studied in the AXT mode.

fraction vector occupy the so-called "special" position and form a weak bright (negative) contrast in the topograph. The image of a deep part of the dislocation perpendicular to the crystal surface contains contributions

from all parts of the dislocation line: the contrast due to separate regions is summed, which leads to an increase in the rosette size. Dislocations having greater lengths of the part perpendicular to the crystal surface form contrast rosettes of a greater size. In Fig. 1, the maximum size is observed for rosette *12* and the minimum, for rosette *1*. The rosette size was compared with the length of a dislocation segment involved in the image formation.

If the X-ray beam crossed the segments of dislocations parallel to the (0001) surface in the section transmission topography mode, these segments formed a bright direct (kinematic) image on the topographs (Fig. 1c). Proceeding from geometric considerations and using the direct image position, we determined the depth of such segments and, hence, the length of edge dislocation lines parallel to the [0001] axis, which were responsible for the rosette formation. These calculations were performed taking into account the incident beam geometry.

Figure 2 shows the experimental plot of the rosette diameter versus the length of the dislocation segment forming the contrast rosette. The rosette diameter was measured for an azimuthal angle of 45° measured from the dislocation slip plane (rosette antisymmetry plane). For comparison, Fig. 2 also presents data on the rosette size for a straight edge dislocation passing from one surface to another in a 6H-SiC crystal with a thickness of 450 μm. An analysis of the topographs shows that, under the given experimental conditions, the rosette images on topographs can be recognized for their diameters $r \geq 20$ μm. Approximation of the plot in Fig. 2 toward smaller rosette diameters allows the corresponding edge dislocation length to be estimated as $l \geq 240$ μm. This result implies that shorter edge dislocations emerging on the sample surface at an angle close to 90° are not imaged as rosettes from their characteristics (Burgers vector direction and sign, slip plane and extra half-plane positions) can be reliably determined.

When the crystal was studied from the opposite side in the AXT mode (in which the entrance and exit sides are interchanged), the images from edge dislocation regions were not obtained, although these regions occurred at a distance as short as 60 μm from the exit surface. Thus, only dislocations emerging from bulk on the surface are imaged as rosettes.

As can be seen in Fig. 1b, the section topograph of an edge dislocation perpendicular to the crystal surface shows contrast rosettes of a more complicated shape than that obtained in the AXT mode. The largest image parts in Fig. 1b are the dark lobes situated on both sides of the dislocation slip plane. Note also that rosettes on the section topographs are asymmetric: more pronounced are the dark lobes on the right from the axes of dislocations and the corresponding lattice compression regions near the extra half-plane. Thus, the AXT mode, as well as the section topography regime, allows the direction and sign of the Burgers vector to be deter-

mined from a single topograph (in Fig. 1, the Burgers vector of all dislocations coincides in direction with the diffraction vector). The size of rosettes on the section topographs, as well as on the AXT images, increases with the length of the edge dislocation segment.

In order to ensure that the edge dislocations will form the contrast rosettes during measurements in the symmetric AXT mode, it is necessary for their axes to make angles close to 90° with the exit surface of the crystal. The rosette size depends (under otherwise equal conditions) on the length of the dislocation segment perpendicular to the surface: the longer the dislocation, the greater the corresponding rosette. Rosettes of the maximum size are due to dislocations passing through the entire crystal thickness. Such features of the topographic image are inherent only in the edge dislocations, since the contrast due to screw dislocations perpendicular to the surface imaged in the AXT mode is determined only by relaxation of the stress field at the crystal surface, while the regions of such dislocations situated in the bulk do not contribute to the rosette formation. Use of X-ray topography measurements both in the anomalous X-ray transmission regime and in the section mode for the identification of dislocations pro-vides additional information as compared to that obtained using each mode separately.

REFERENCES

1. L. N. Danil'chuk, Yu. A. Drozdov, A. O. Okunev, *et al.*, Zavod. Lab. **68** (11), 24 (2002).

2. V. A. Tkal', A. O. Okunev, Yu. A. Drozdov, *et al.*, Poverkhnost, No. 1, 32 (2004).

3. A. S. Tregubova and I. L. Shul'pina, Fiz. Tverd. Tela (Leningrad) **14**, 2670 (1972) [Sov. Phys. Solid State **14**, 2305 (1972)].

4. E. V. Suvorov, V. I. Polovinkina, V. I. Nikitenko, *et al.*, Phys. Status Solidi A **26**, 385 (1974).

5. V. L. Indenbom and F. N. Chukhovskiĭ, Usp. Fiz. Nauk **107**, 229 (1972) [Sov. Phys. Usp. **15**, 298 (1972)].

Translated by P. Pozdeev

Initial Stages of Cobalt Film Growth on MgO(001) Surface

I. I. Pronin[a,*]**, D. A. Valdaĭtsev**[a]**, A. S. Voronchikhin**[a]**, M. V. Gomoyunova**[a]**,**
S. F. Contri[b]**, S. Benedetti**[b]**, P. Lukes**[b]**, and S. Valeri**[b]

[a] *Ioffe Physicotechnical Institute, Russian Academy of Sciences, St. Petersburg, 194021 Russia*

[b] *INFM–National Research Center on Nanostructures and Biosystems at Surfaces (S³),*
Universitá di Modena e Reggio Emilia, via G. Campi 213/a, 41100 Modena, Italy
* e-mail: Igor.Pronin@mail.ioffe.ru
Received January 25, 2005

Abstract—The initial stages of cobalt film growth on a MgO(001) surface was studied by methods of sample surface structure imaging by reflected electrons, low-energy electron diffraction, and Auger electron spectroscopy. The measurements were performed at room temperature for cobalt layer thicknesses up to 40 Å. It is established that cobalt film growth proceeds according to the island mechanism. In the interval of cobalt film thicknesses below ~10 Å, the dominating surface phase has the form of cobalt islands with an fcc structure; at greater layer thicknesses, the surface film consists predominantly of cobalt grains with an hcp structure. © 2005 Pleiades Publishing, Inc.

The study of low-dimensional structures formed in the course of the deposition of various metals on dielectric substrates is an important research direction in the modern physics and chemistry of surfaces [1, 2]. In particular, much attention is devoted to the formation of clusters and ultrathin epitaxial films of ferromagnetic metals on the surface of chemically and thermally stable magnesium oxide. Such systems exhibit unusual properties and are of interest from the standpoint of both basic science and advanced nanotechnologies, in particular, for the creation of new magnetic data recording devices [3], sensors, and catalysts [4]. The available papers are devoted mostly to the formation of iron-based nanostructures on the MgO(001) crystal surface [5–10], while other systems, including Co/MgO(001), have been studied to a much lesser extent. To our knowledge, only two papers contain information about the crystal structure of nanometer-thick cobalt layers grown on the MgO surface by method of magnetron sputtering [11, 12]. These investigations, devoted to superlattices comprising alternating metal and dielectric layers, showed that their magnetic and optical properties significantly depend both on the thickness of cobalt layers and on their structure.

This Letter presents the results of an investigation into the growth mechanism and atomic structure of ultrathin cobalt layers formed on an atomically clean MgO(001) single crystal surface under ultrahigh vacuum conditions. The study was performed using a combination of modern surface analytical techniques, including Auger electron spectroscopy (AES), low-energy electron diffraction (LEED), and surface structure imaging by reflected electrons [13, 14].

The experiments were performed at the Ioffe Physicotechnical Institute (St. Petersburg) and at the INFM (Modena), where the samples were additionally characterized using the method of Auger electron emission modulated by the primary electron diffraction [15]. In both research laboratories, the study was performed on identical MgO(001) samples obtained by cleavage immediately prior to placing them into the vacuum chamber with a residual pressure below 2×10^{-10} Torr. According to the AES and LEED data,[1] this procedure provided reproducible atomically clean MgO surface with a quite perfect crystal structure. Cobalt was deposited onto the sample surface at room temperature at a rate of 1.6 Å/min, which was monitored (with the aid of the quarts microbalance technique) immediately in the course of metal deposition.

The results of experimental measurements are presented in Figs. 1a–1d. These photographs show the typical patterns of electron diffraction from MgO(001) single crystal samples with increasing thickness of the cobalt layer deposited onto the surface. The patterns were obtained using a standard LEED attachment using a primary beam of 1-keV electrons normally incident onto the sample surface. The data are presented in the form of two-dimensional maps (constructed in stereo-

---

[1] In order to reduce the effects of dielectric surface charging by the probing electron beam, the LEED and AES measurements were performed using primary electron beam energies above 82 eV and below 1.8 keV, respectively.

graphic projection using a linear black-and-white scale) of the intensity of electron scattered with respect to the polar and azimuthal escape angles. The range of electron escape angles measured was 7°–46°. The brightest regions in the patterns correspond to the diffraction maxima observed for electrons traveling along the most closely packed atomic chains in the sample studied. These features in the intensity distribution are related to the phenomenon of the focusing of inelastically scattered electrons in crystals [16], which enables this method to image the crystal structure of the near-surface layer of a sample in the real space [13, 14].

The most clear and contrast pattern is observed for a MgO(001) crystal sample with an atomically clean surface (Fig. 1a). This diffractogram demonstrates a fourfold mirror-rotational symmetry characteristic of the given crystal face. We have also calculated the pattern of electron diffraction from a MgO(001) single crystal surface within the framework of a cluster model of single scattering [16]. The results of these calculations, which were performed assuming that the atomic structure of the near-surface region of the sample coincides with the bulk crystal structure, are presented in Fig. 1e. A comparison of the patterns in Figs. 1a and 1e shows that all practically significant features of the experimental diffraction pattern are well reproduced by the results of the model calculation. Therefore, analogous modeling can be used for the interpretation of patterns observed in the course of cobalt deposition onto the substrate surface.

The deposition of cobalt leads, first, to a significant decrease in the contrast of diffraction patterns and, second, to an attenuation of the features related to the substrate. These trends are already well manifested after the deposition of a 5-Å-thick cobalt layer (Fig. 1b). Third, an increase in the cobalt layer thickness is accompanied by redistribution of the intensity between various diffraction maxima, which leads to a change in the general character of the pattern. All these variations are related to (i) a decrease in the contribution of substrate to the observed pattern and (ii) to the gradual formation of a metal film with the structure characteristic of this metal. The latter effect becomes predominant when the deposited metal thickness exceeds ~10 Å (Figs. 1c and 1d). It should be emphasized, however, that the diffraction patterns retain their fourfold symmetry. Taking into account that metallic cobalt usually possesses a hexagonal close packed (hcp) structure, the observed symmetry excludes the possibility that cobalt layers formed on the MgO(001) surface are characterized by the epitaxial relation hcp(001)‖MgO(001). Indeed, if this relation were valid, the observed pattern would exhibit a sixfold symmetry. Moreover, the results of model calculations showed that, in such a case, a layer-by-layer growth of the metal deposit would already render the substrate contribution negligibly small at a cobalt layer thickness of ~6 Å.
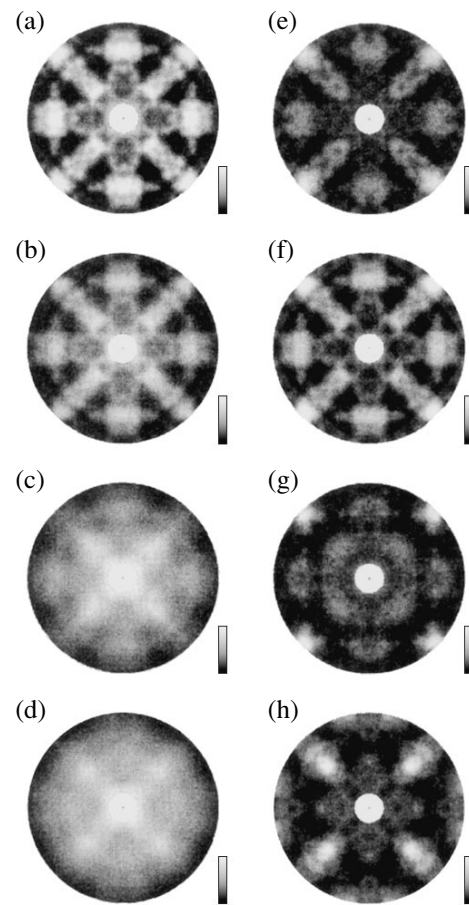
Fig. 1. (a–d) The patterns of scattering of 1-keV electron from a MgO(001) crystal with (a) an atomically clean surface and (b–d) with cobalt films of various thicknesses: (b) 5 Å; (c) 10 Å; (d) 20 Å. (e–f) The results of modeling of the experimental patterns in the cluster approximation of single scattering for a MgO(001) single crystal with (e) a clean surface and with (g) an epitaxial fcc cobalt film and (h) an epitaxial hcp cobalt film composed of the grains of two types; (f) a linear superposition of patterns (a), (g), and (h) with the weight coefficients 50, 30, and 20%.

The pattern with a fourfold symmetry may appear if the growing cobalt film is characterized by a different epitaxial relation, namely, hcp(100)‖MgO(001). Moreover, the surface of the film must contain approximately equal numbers of cobalt grains in which the hcp[001] directions are parallel to the MgO[100] and MgO[010] axes. Evidence for this possibility is provided by close values of the c and a lattice parameters for the cobalt and substrate (4.07 and 4.21 Å, respectively) with a difference of only 3.3%. A diffraction pattern calculated for such a system is depicted in Fig. 1h. As can be seen, this pattern quite satisfactorily reproduces all the main features of the experimental diffractogram observed for a 20-Å-thick cobalt layer (Fig. 1d). However, the contrast of the model pattern is much higher than that of the experimental one. This difference suggests that a relatively thick film contains, besides cobalt grains with the

C, %
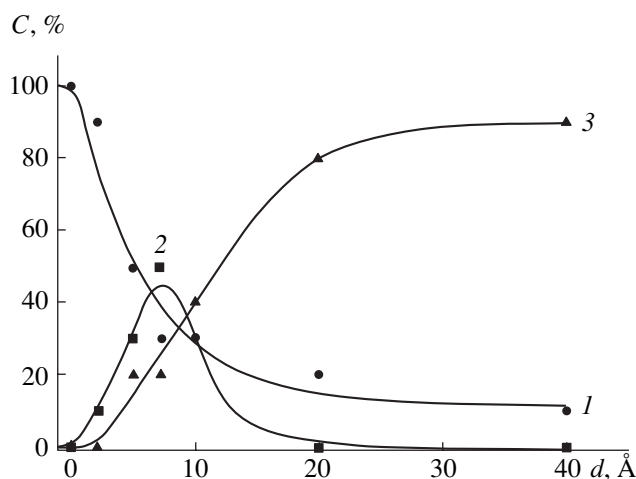
Fig. 2. Plots of the contributions of various crystalline cobalt phases to the diffraction patterns versus cobalt film thickness on MgO(001) substrate: (*1*) substrate; (*2*) fcc cobalt layer; (*3*) hcp cobalt layer.

aforementioned epitaxial ratio, a certain amount of grains with random mutual orientations and without preferred orientational relations with the substrate. In addition, a diffuse background may also appear as a result of the electron scattering from atoms localized in the regions of grain boundaries and some other defects in the film.

As is known, cobalt is also capable of crystallizing in a face-centered cubic (fcc) lattice. Therefore, it is necessary to consider the possibility of cobalt layer growth with the epitaxial relation fcc(001)‖MgO(001), which must also provide for the diffraction pattern with a fourfold symmetry. The results of model calculations are presented in Fig. 2g. As can be seen, all the four principal maxima (corresponding to the electrons emitted in the [110] directions) found in the peripheral region of the calculated pattern are weakly pronounced in the experimental diffractograms of thick cobalt films. Thus, the fcc crystal phase may form, if at all, only in the very early stages of cobalt adsorption.

In order to elucidate the crystal structure of cobalt films formed in the initial stage of deposition, the entire set of measured patterns was analyzed using the method described in [17]. The main idea of this approach consists in representing each pattern as a superposition of standard patterns of the substrate and those of the possible crystal phases of the adsorbate. Then, the superposition is optimized with respect to the statistical weights of various system components. In the course of this optimization, the corresponding coefficients are varied at a constant step in the interval from 0 to 1, and each set is characterized by quantitative comparison of the calculated and measured patterns in terms of the *R*-factors. This method showed good results for the adsorption systems with surface films

growing according to the island mechanism [14]. Taking into account that the MgO(001) surface possesses a lower free surface energy as compared to that of the transition metals, it is natural to assume that the cobalt film in our system also grows in the island mode and the aforementioned procedure is quite justified.

Using the patterns presented in Figs. 1a, 1g, and 1h as the standard components and applying the aforementioned approach, we succeeded in modeling the experimental results with a quite satisfactory precision. This is confirmed by a comparison of the pattern observed upon the deposition of a 5-Å-thick cobalt layer (Fig. 1b) with the model pattern (Fig. 1f) obtained assuming that cobalt islands occupy ~50% of the substrate surface. Among these islands, the fraction of cobalt grains with the fcc structure amounted to 60%, and the fraction of hcp grains was 40%. The good coincidence of the experimental and model patterns provides evidence that the Co/MgO(001) system is in fact characterized by the island growth mechanism and features the formation of fcc cobalt grains in the early deposition stages. The former conclusion was also confirmed by the AES data.

The results of analysis of the diffraction patterns are presented in Fig. 2, which shows variation of the statistical weight of the substrate (curve *1*) and the two crystalline phases of cobalt (curves *2* and *3*) depending on the deposited layer thickness. As can be seen, the dominating phase in the interval of film thicknesses below ~10 Å has the form of cobalt islands with an fcc structure; at greater layer thicknesses, the surface film consists predominantly of cobalt grains with an hcp structure. Thus, the application of the method of imaging of the surface crystal structure to the study of a Co/MgO(001) system allowed us to reveal variations in the crystal structure of cobalt films depending on their thickness. These results may be of importance for understanding the magnetic properties of ultrathin cobalt layers.

REFERENCES

1. H.-J. Freund, Surf. Sci. **500**, 271 (2002).

2. J. Shen and J. Kirschner, Surf. Sci. **500**, 300 (2002).

3. Y. Park, S. Adenwalla, G. P. Felcher, and S. D. Bader, Phys. Rev. B **52**, 12779 (1995).

4. R. A. Hubert and J. M. Gilles, Appl. Surf. Sci. **22**, 631 (1984).

5. B. M. Lairson, M. Visokay, R. Sinclair, and B. M. Clemens, Appl. Phys. Lett. **61**, 1390 (1992).

6. K. Thürmer, R. Koch, M. Weber, and K. H. Rieder, Phys. Rev. Lett. **75**, 1767 (1995).

7. T. Suzuki, S. Hishita, K. Oyoshi, and R. Souda, Surf. Sci. **442**, 291 (1999).

8. G. Fahsold, A. Pucci, and K.-H. Rieder, Phys. Rev. B **61**, 8475 (2000).

9. G. Fahsold, A. Priebe, and A. Pucci, Appl. Phys. A **73**, 39 (2001).

10. A. di Bona, C. Giovanardi, and S. Valeri, Surf. Sci. **498**, 193 (2002).

11. H. Sato and T. Miyazaki, J. Magn. Magn. Mater. **177–181**, 1197 (1998).

12. J.-W. Cai, S. Okamoto, O. Kitakami, and Y. Shimada, Phys. Rev. B **63**, 104418 (2001).

13. I. I. Pronin and M. V. Gomoyunova, Prog. Surf. Sci. **59**, 53 (1998).

14. M. V. Gomoyunova and I. I. Pronin, Zavod. Lab. **167** (4), 24 (2001).

15. S. Valeri and A. di Bona, Surf. Rev. Lett. **4**, 141 (1997).

16. M. V. Gomoyunova, I. I. Pronin, and N. S. Faradzhev, Zh. Éksp. Teor. Fiz. **110**, 311 (1996) [JETP **83**, 168 (1996)].

17. I. I. Pronin, D. A. Valdaitsev, N. S. Faradzhev, *et al.*, Appl. Surf. Sci. **175–176**, 83 (2001).

Translated by P. Pozdeev

Mechanisms of Light Absorption in Gamma-Irradiated Blanks for Optical Fibers Based on High-Purity Quartz Glass

M. O. Zabezhaĭlov, A. L. Tomashuk, I. V. Nikolin, V. G. Plotnichenko,
E. B. Kryukova, and V. V. Koltashev

Scientific Center for Fiber Optics, Prokhorov Institute of General Physics, Russian Academy of Sciences,
Moscow, 117924 Russia
e-mail: post@fo.gpi.ru
Received January 24, 2005

Abstract—The IR optical absorption spectra and the Raman spectra of rods made of high-purity quartz glass of the KU-1 and KS-4V grades have been studied in comparison to those measured for the blanks of optical fibers fabricated from this glass using the plasma outside deposition (POD) technology. Based on these data, a discussion is presented of the most probable mechanisms responsible for an increase in the γ-radiation-induced absorption in high-purity quartz glasses as a result of their processing in the course of optical fiber fabrication using the POD technology. © *2005 Pleiades Publishing, Inc.*

Introduction. Radiation-resistant optical fibers with a core made of high-purity quartz glasses can be used for remote spectroscopic monitoring and imaging in nuclear power engineering [1] and for the transmission of high-power UV laser radiation in medicine [2]. In the course of operation in such applications, optical fibers are subjected to the action of nuclear or UV radiation. This results in the appearance of radiation-induced defects (color centers) in the glass, which give rise to undesired optical losses.

The optical fibers for the aforementioned applications are usually fabricated by means of the so-called plasma outside deposition (POD) technology, whereby a reflecting fluorosilicate sheath is formed on a core rod made of undoped quartz glass [3]. It has been established [4] that use of the POD technology leads to the appearance of defects, which serve as precursors for the subsequent formation of radiation-induced color centers. Recently, we showed [5] that the formation of such defects during the POD process is not related to the diffusion of fluorine atoms into the core, as had been previously suggested [6]. We have assumed that an increase in the number of color center precursors during the processing of blanks is related to the incorporation of impurities (H_2O, HCl) into the glass and/or to the formation of stressed bonds as a result of the high-temperature treatment of the core in the plasma torch. However, no evidence has been available for the verification of our hypothesis.
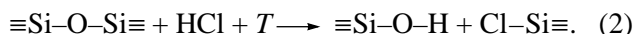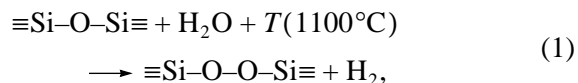
The aim of this study was to obtain experimental data confirming the assumption [5] concerning the factors responsible for the formation of color center precursors in the optical fiber core in the course of blank processing.
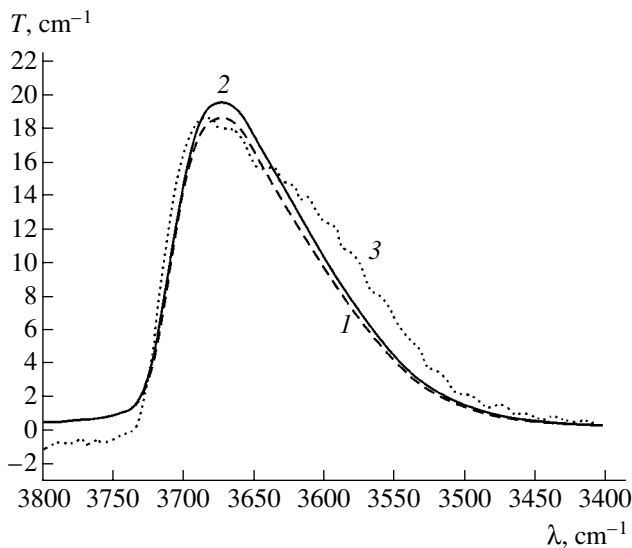
Experimental. We have studied the IR absorption spectra and the Raman spectra of cut sections of the KU-1 glass (containing ~800 ppm of OH groups and ~80 ppm of Cl), KS-4V glass (<1 ppm of OH groups and ~40 ppm of Cl), and the blanks made of these glasses using the POD process under standard technological conditions (temperature and duration) [5].

The IR absorption spectra were recorded on an IFS-113V vacuum Fourier spectrometer possessing a noise level not exceeding 0.1% of the transmission intensity and a resolution of 1 cm^{-1}. The thickness of samples cut for the IR measurements was approximately 0.5 mm.

The Raman spectra with a resolution of 1 cm^{-1} were obtained on a Triple Raman Spectrograph setup with an Ar laser excitation at a wavelength of 514.5 nm. The core and blank samples cut for these measurements had a thickness of 1 mm.

Results and discussion. The IR spectrum of samples of the KU-1 glass upon POD processing (blank cut section) shows an increase in amplitude of the main absorption band due to the OH stretching vibrations at 3670 cm^{-1} (Fig. 1). No such increase was observed for the KS-4V glass. These results show evidence in favor of our hypothesis [5] concerning the incorporation of hydrogen-containing impurities (e.g., H_2O, HCl) into the glass structure as a result of the POD processing, with the formation of peroxide and Si–Cl bonds. Such bonds are precursors of the color centers of two types: nonbridging oxygen and E' center, respectively, formed according to the reactions

$$\equiv\text{Si–O–Si}\equiv + H_2O + T(1100°C)$$
$$\longrightarrow\ \equiv\text{Si–O–O–Si}\equiv + H_2, \tag{1}$$

$$\equiv\text{Si–O–Si}\equiv + HCl + T \longrightarrow\ \equiv\text{Si–O–H} + \text{Cl–Si}\equiv. \tag{2}$$

Fig. 1. The IR absorption spectra of cut sections of (*1*) the KU-1 glass and (*2*) a blank obtained via POD processing of this glass. Curve *3* is the normalized difference between spectra *1* and *2* (normalization factor, 20).
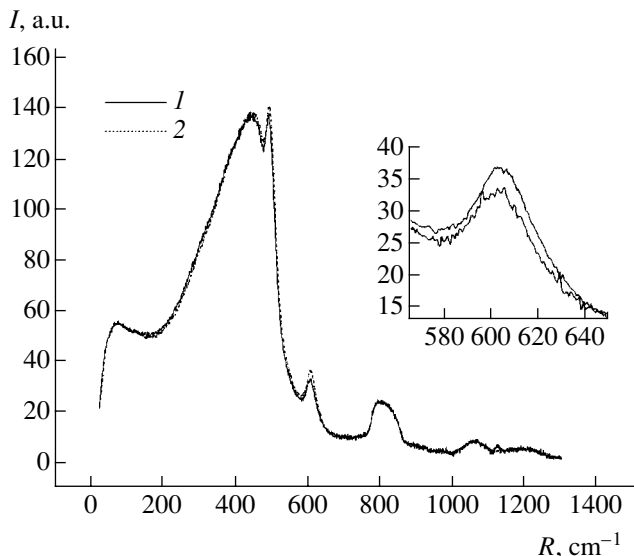
Fig. 2. The Raman spectra of cut sections of (*1*) the KU-1 glass and (*2*) a blank obtained via POD processing of this glass. The inset shows a fragment of the spectrum in the region of a peak at 606 cm^{-1} on a greater scale.

The density of the color center precursors formed in this way can reach 10^{18} cm^{-3} (as calculated proceeding from an increase in intensity of the absorption band due to OH groups). This estimate does not contradict evaluations of the density of color centers formed

in the KU-1 glass as a result of γ irradiation ($\sim 10^{17}$ cm^{-3} [5]).

The Raman spectrum of the KU-1 glass upon POD processing (Fig. 2) exhibits an increase in amplitude of the peaks at 495 and 606 cm^{-1}, which correspond to structures of the three- and four-chain rings. According to [7], the formation of such structures leads to an increase in the number of stressed bonds in the glass structure. The Raman spectra of samples of the KS-4V glass upon POD processing did not show such changes.

Conclusions. We obtained experimental data confirming the hypothesis [5] concerning a mechanism of the formation of color center precursors in the course of OWF blank processing using the POD technology. In particular, we established that the POD process may result in the following changes:

(i) formation of three- and four-chain rings in the glass structure, which lead to an increase in the number of stressed bonds–precursors of the color centers of two types (nonbridging oxygen and E' centers);

(ii) incorporation of hydrogen-containing impurities (e.g., H_2O, HCl) into the glass structure, which is accompanied by to the formation of OH groups, peroxide bonds, and Si–Cl bonds, which also are precursors of the color centers of two types (nonbridging oxygen and E' centers).

The absence of a significant amount of precursors of the color centers (nonbridging oxygen and E' centers) in the case of blank fabrication from the KS-4V glass can be explained by the significantly lower number of hydrogen bonds in this glass and the higher rigidity of its structure (as compared to the KU-1 glass), which hinders the development of the defect formation processes considered above.

REFERENCES

1. A. L. Tomashuk and K. M. Golant, Proc. SPIE **4083**, 188 (2000).
2. A. M. Prochorov, G. P. Kuz'min, A. V. Kisletsov, *et al.*, Proc. SPIE **3829**, 18 (1999).
3. A. S. Biriukov, E. M. Dianov, K. M. Golant, *et al.*, Sov. Lightwave Commun. **3**, 1 (1993).
4. K. Nagasawa, R. Tohmon, and Y. Ohki, Jpn. J. Appl. Phys. **26**, 148 (1987).
5. M. O. Zabezhaĭlov, A. L. Tomashuk, I. V. Nikolin, *et al.*, Neorg. Mater. **41**, 377 (2004).
6. D. L. Griscom, J. Appl. Phys. **77**, 5008 (1995).
7. K. Awazu and H. Kawazoe, J. Appl. Phys. **94**, 6243 (2003).

Translated by P. Pozdeev

The Normal Current Density Effect in Barrier Discharge

D. A. Malik, K. E. Orlov*, I. V. Miroshnikov, and A. S. Smirnov

St. Petersburg State Technical University, St. Petersburg, 195251 Russia
* e-mail: orlov@phtf.stu.neva.ru
Received February 24, 2005

Abstract—The evolution of the glow of a homogeneous barrier discharge during a single current pulse have been experimentally studied. It is demonstrated that the behavior of this discharge is analogous to the normal current density effect in a dc discharge. © 2005 Pleiades Publishing, Inc.

Barrier discharge is known as an effective means of obtaining nonequilibrium plasma at high pressures (on the order of 1 bar) of a working gas. Although the first experiments with barrier discharge were performed almost a century and a half ago [1], the most extensive investigations have been undertaken in the past two decades. This discharge is now widely used for the synthesis of ozone, modification of surfaces, deposition of coatings, destruction of nitrogen oxides, and excitation of excimer lamps and plasma displays [2].

Barrier discharge may exist in various forms [2–4]. Depending on the composition and pressure of the working gas, the thickness and material of the insulator, and the interelectrode distance, barrier discharge may take the form of a bundle of filaments (filamentary mode), spatially organized spots (spot mode), or spatially homogeneous plasma (diffuse mode). In the latter case, a homogeneous breakdown takes place over the entire volume of the discharge gap and a nonequilibrium plasma is formed, which uniformly fills the entire gap.

The diffuse form of barrier discharge, which is also called atmospheric pressure glow, offers a promising and relatively simple means of obtaining homogeneous nonequilibrium plasmas at high pressures. As a rule, homogeneous discharge of this kind is most readily obtained in pure helium or in mixtures where helium is the dominating component [5]. Homogeneous forms of barrier discharge are also quite readily obtained at reduced pressures. Recently, it was demonstrated [6] that the transitions between spark and homogeneous forms of barrier discharge could be determined by the regime of matching of a high-frequency drive oscillator to the discharge. A number of papers have been devoted to the dependence of the regime of barrier discharge operation on one of the possible control parameters, such as the thickness and material of the insulator and the working gas pressure [7–11]. Although the number of publications on the subject is constantly increasing, the possible scenarios of formation of a homogeneous barrier discharge have not yet been established and

explained. Acceptable and justified scaling relations for such discharges also remain unknown.

Previously, we experimentally demonstrated that, using a resonance system of oscillator matching to the discharge, it is possible to observe the regimes of barrier discharge with a partly filled electrode surface [12]. In such regimes, the average power deposited in the discharge varies at a virtually constant shape and amplitude of the interelectrode voltage and is accompanied by simultaneous change in the area occupied by the visible glow of discharge. In order to describe this behavior, we introduced the concept of the normal power density for the barrier discharge [12] by analogy with the well-known normal current density in the dc discharge.

This paper presents the results of an experimental investigation into the evolution of the glow of a homogeneous barrier discharge during a single current pulse. The experiments were performed using the experimental setup described in [12]. The discharge was initiated between two aluminum electrodes, both of which had a diameter of 33 mm. The electrodes were coated by insulating films of aluminum oxide. The oxide layer thickness was 100 μm, and the interelectrode distance was 2.4 mm. Pulsed voltage with a frequency of 100 kHz was applied to electrodes via a tunable system of resonance matching. The discharge glow was monitored using a charge-coupled-device camera with an optical signal amplifier (ICCD ProScan). The exposure time was 200 ns. The camera was synchronized with discharge current pulses at a preset phaseshift. One shot was accumulated over 100 sequential discharge current pulses of identical polarity (i.e., at a frequency of 50 kHz). The shots were made at a 100-ns step.

Figure 1b shows a series of photographs of the glow observed in the interelectrode gap at various moments of time during a single discharge current pulse. As can be seen, the discharge glow appears in the central region and then spreads in the radial directions toward edges of the electrodes. Evidently, the side view of the glow in the interelectrode gap represents chord projec-

Discharge current, A
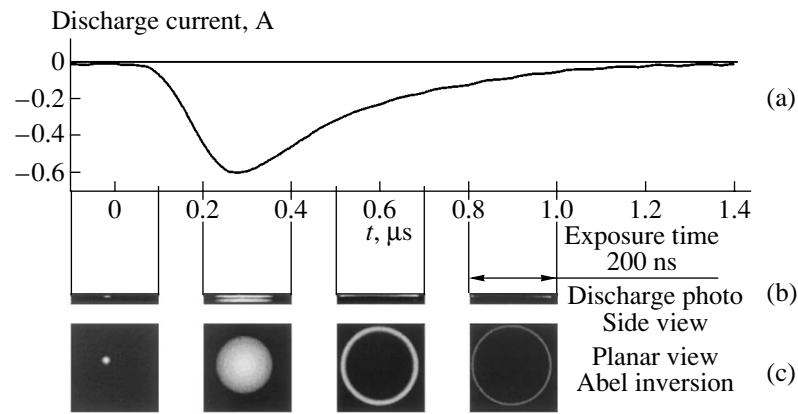
Fig. 1. Homogeneous barrier discharge evolution during a single current pulse: (a) oscillogram of the discharge current pulse; (b) a series of photographs of the discharge gap at various moments of time; (c) planar projections obtained by numerical inverse Abel transform assuming axial symmetry of the discharge glow intensity distribution in the plane of electrodes. Interelectrode distance, 2.4 mm; working gas mixture, CO_2–N_2–He (1 : 1 : 8); gas pressure, 40 Torr.

tions of the glow between two disk electrodes. An analysis of the general structure of these photographs leads to the conclusion that the glow intensity distribution is close to axially symmetric. The planar projections of the glow were obtained using the inverse Abel transform. The results are presented in Fig. 1c together with the corresponding photographs of the discharge glow (Fig. 1b). As can be seen, the discharge evolves as an expanding ring. Assuming that the glow region approximately corresponds to a real space occupied by the discharge, it is possible to use the obtained planar projections for estimating the electrode area occupied by the discharge at various moments of time.

Figure 2 shows an oscillogram of the total current through the discharge gap and the results of such an evaluation of the discharge area at various moments of time. As can be seen from these data, the discharge current is proportional to the discharge area. The current
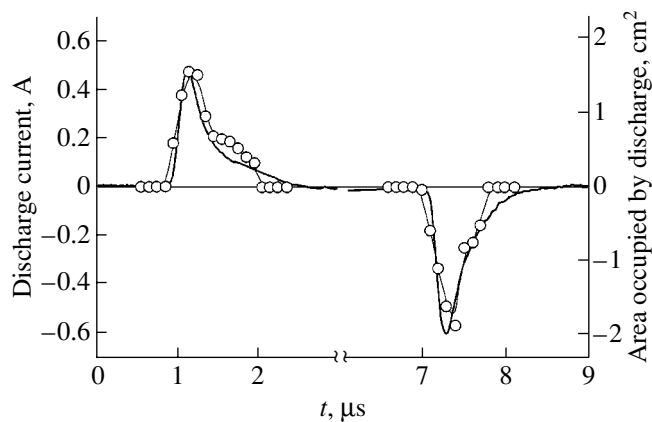
density is 300 mA/cm^2, which agrees in the order of magnitude with the normal current density for a dc discharge in an analogous gas mixture.

The obtained experimental results lead to the following conclusions. First, the insulator surface is charged gradually, accompanying the emission spot spreading over the electrode surface, rather than simultaneously over the entire electrode area. Second, the recharge in any local region of the electrode surface proceeds at a constant current density and takes a time on the order of a hundred nanoseconds. The relatively large duration (~1 μs) of the total discharge current pulse is determined primarily by the limitation of the total discharge current amplitude by the resonance matching system. It should be noted that this system also determines the magnitude and shape of the interelectrode voltage. In particular, the resonance matching system used in our experiments ensured a low output impedance at the excitation frequency and the frequencies corresponding to the discharge current pulse. As a result, the shape of the interelectrode voltage was nearly sinusoidal, while the amplitude was determined by power losses in the discharge. The use of an amplifier (oscillator) with a large output impedance for discharge excitation leads to the significant distortion of the voltage pulse shape, which considerably complicates the interpretation of experimental results. It should be noted that our experimental data also indicate that one-dimensional modeling cannot provide an adequate description of processes in the barrier discharge.

Fig. 2. Discharge current oscillograms (solid curves) and estimated values of the area occupied by the discharge (open circles) under the discharge conditions presented in Fig. 1.

REFERENCES

1. W. Siemens, Poggendorff's Ann. Phys. Chem. **102**, 66 (1857).

2. U. Kogelschatz, Plasma Chem. Plasma Proc. **23**, 1 (2003).

3. U. Kogelschatz, IEEE Trans. Plasma Sci. **30**, 1400 (2002).

4. G. J. Pietsch, Contrib. Plasma Phys. **41**, 620 (2001).

5. F. Massines, A. Rabeli, P. Decomps, *et al.*, J. Appl. Phys. **83**, 2950 (1998).

6. Zhiyu Chen, IEEE Trans. Plasma Sci. **30**, 1922 (2002).

7. F. Tochikubo, T. Chiba, and T. Watanabe, Jpn. J. Appl. Phys. **38**, 5244 (1999).

8. N. Gherardi, G. Gouda, E. Gat, *et al.*, Plasma Sources Sci. Technol. **9**, 340 (2000).

9. V. I. Gibalov and G. J. Pietsch, J. Phys. D: Appl. Phys. **33**, 2618 (2000).

10. Yu. B. Golubovskii, V. A. Maiorov, J. Behnke, and J. F. Behnke, J. Phys. D: Appl. Phys. **35**, 751 (2002).

11. L. Mangolini, C. Anderson, K. Sittig, *et al.*, in *Proceedings of the 16th International Symposium on Plasma Chemistry, Taormina, 2003*.

12. D. A. Malik, K. E. Orlov, and A. S. Smirnov, Pis'ma Zh. Tekh. Fiz. **30** (2), 44 (2004) [Tech. Phys. Lett. **30**, 908 (2004)].

Translated by P. Pozdeev

Decreasing the Action of a Flow Behind a Weak Shock Wave Emerging from a Channel upon an Obstacle

T. V. Bazhenova*, V. V. Golub, and A. S. Chizhikov

Institute for High Energy Densities, Associated Institute for High Temperatures, Russian Academy of Sciences, Moscow, Russia
* e-mail: bazhenova@ihed.ras.ru
Received February 14, 2005

Abstract—It is experimentally demonstrated that, if the flow behind shock waves outgoing from a channel is subsonic, the action of this flow upon an obstacle can be decreased by changing the shape of the output channel cross section. The results of numerical modeling of the experimental oscillograms show that, by replacing a round channel with a cross-shaped one, the excess action upon the obstacle in a quasi-stationary stage can be reduced by half. This decrease is related to energy dissipation in a three-dimensional flow as a result of the interference of rarefaction and compression waves. The interference arises due to mass redistribution between various symmetry axes in the gaseous medium and due to the flow energy losses for the vortex formation at the channel edges, which are revealed by schlieren photographs. © 2005 Pleiades Publishing, Inc.

It has been demonstrated [1] that total pressure losses in a jet can be minimized by controlling the wave structure of the flow. Previously, we studied the possibility of controlling the nonstationary action of shock waves outgoing from a channel upon an obstacle by changing the channel geometry [2, 3]. In particular, the action of a flow behind the shock wave outgoing from channels with round, square, and cross-shaped cross sections upon an obstacle was experimentally studied and numerically simulated for strong shock waves, the flow behind which is supersonic. It was established that the passage to a three-dimensional geometry (by changing the channel cross section from round to cross-shaped) leads to vanishing of the direct pressure jump (Mach disk) [4] and results in a twofold increase in the intensity of flow action upon the obstacle [5].

This paper presents the results of an experimental study of the interaction of an obstacle with the flow behind a shock weave outgoing from a cross-shaped channel in the case when the flow behind the shock wave is subsonic (weak shock wave). The possibility of decreasing the action of weak shock waves upon an obstacle is of interest in some applications related to increasing safety with respect to explosions in mines, houses, pipelines, and pressure vessels, and decreasing the acoustic action of exhaust gasses in internal combustion engines, etc.

The experimental setup comprised a shock tube with a 40×40 mm square cross section connected to a cylindrical vacuum chamber. The tube end was closed with a flange carrying a channel of round or cross-shaped cross section, which was situated inside the tube. The round channel had a diameter of 20 mm, while the cross-shaped channel represented two slits 37 mm long and 5 mm wide intersecting at a right angle. The end of the shock tube was placed against plane-parallel optical windows of a low-pressure chamber. This chamber accommodated a flat obstacle with a positioning mechanism that allowed the distance from the channel output edge to the obstacle to be varied. The low- and high-pressure chambers were filled with air at an initial pressure of $p_0 = 4.0$ kPa. The incident shock wave velocity was measured to within 1–2% using a base technique.

For the comparison of the total pressure variations in the flow upon the shock wave emergence from the channels with different cross sections, equivalent distances from the channel edge to the obstacle were determined using the condition of equal effective gauges. For a round channel, the effective gauge d equals the circle diameter ($d = d_0 = 20$ mm); for the cross-shaped channel, the effective gauge is the diameter of a circle of equivalent area ($d = 1.08d_0$).

A pressure sensor of the Kistler 603B type was mounted on the obstacle at the center of the flow. Pressure sensors arranged at a certain step along two radii forming an angle of 45° allowed the pressure to be measured in the flows with two symmetry axes, which was necessary for studying the diffraction of shock waves emerging from the cross-shaped channel.

The flow structure was visualized using a shadow device of the IAB-451 type and a high-speed optomechanical camera of the VSK-5 type. We compared the pressure oscillograms and the schlieren photographs for the channels with different cross sections and two
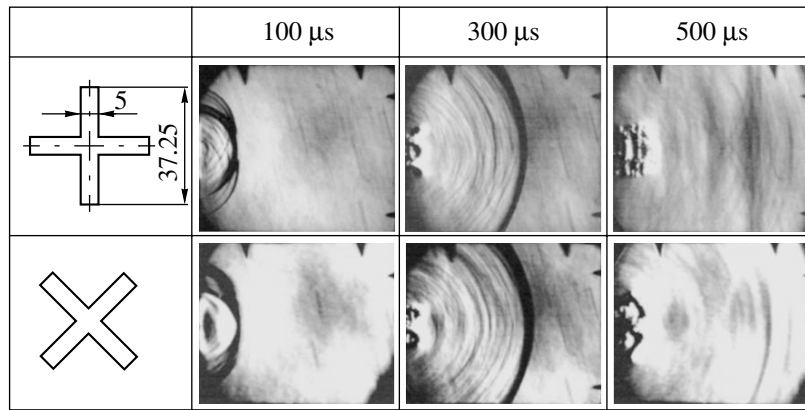
Fig. 1. Schlieren photographs showing the flow structure behind the shock wave emerging from a cross-shaped channel ($M_0 = 1.17$) in the nonstationary stage of the process. The distance between marks is 100 mm.

distances from the obstacle to the channel output $L = d$ and $2d$. The comparison was performed in a dimensionless time t related to the dimensional variable τ as $t = (\tau/d)\sqrt{p_0/\rho_0}$, where p_0 and ρ_0 are the pressure and density of unperturbed gas.

The flow behind the outgoing shock wave in air becomes subsonic for an incident shock wave Mach number of 2.2. However, when the shock wave is ejected from the channel, a rarefaction wave formed at the convex corner moves upstream along the wall and accelerates the flow. The minimum Mach number for which such a supersonic flow is formed is 1.35 [6, 7]. For this reason, our experiments, devoted to the influence of the channel cross section on shock wave action upon the obstacle, were performed for an incident shock wave Mach number of 1.17 (for which the calculated Mach number in the flow behind the outgoing shock wave was 0.25).

As can be seen from the schlieren photographs presented in Fig. 1, the flow outgoing from a cross-shaped channel in the nonstationary stage for the initial shock wave Mach number of $M_0 = 1.17$ exhibits no pressure jumps typical of a supersonic flow. At the initial moment, the shock wave front exhibits a flat portion against the channel output. Subsequently, the front gradually acquires a spherical shape and acoustic waves begin to propagate from the front along the flow. Vortices formed at the channel output edges may also account for the total pressure losses. The flow structure is different when viewed along the cross side and at an angle relative to this direction.

Measurements of the pressure at an obstacle using several sensors arranged in the radial direction provide an integral characteristic of the pressure distribution. Here, the boundary conditions are provided by the condition of symmetry at $R = 0$ and the condition of a finite perturbation at $R \longrightarrow \infty$. Then, using interpolation and

integrating over the radius, we determine the action upon the obstacle as

$$F(t) = \int_0^R \int_0^{2\pi} P^*(r, t)d\varphi dr, \quad \text{(kg m)/s}^2.$$

In the case of an axisymmetric flow, the integral is readily reduced to one-dimensional. For the graphical analysis of pressure oscillograms, we pass to dimensionless values by normalizing to the initial pressure P_0
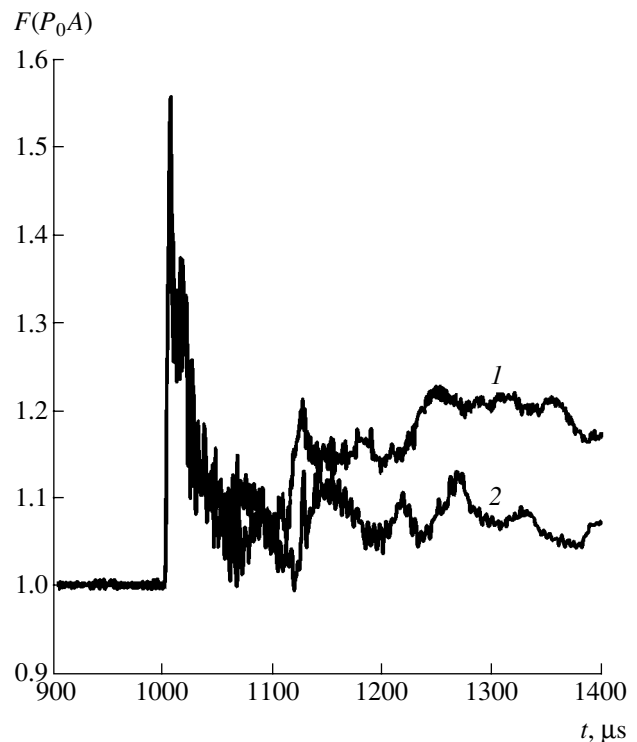
Fig. 2. Time variation of the force of pressure produced by a shock wave with $M_0 = 1.17$ emerging from a (*1*) round and (*2*) cross-shaped channel upon the obstacle occurring at a distance of $L = 2d$ from the channel output.

and the integration area A (the integration domain is a circle of radius R).

The integration domain was selected in the form of a circle with the radius $R = 0.5d$, which corresponds to the flow core. The field of pressures at each moment of time was determined by approximation in the radial direction and by interpolation over the angle. The results of numerical integration of the experimental oscillograms are presented in Fig. 2 (for $Z = d$). These curves, showing the time variation of the gas pressure upon the obstacle, indicate that the replacement of a round channel by the cross-shaped one decreases by half the intensity of flow action upon the target in the quasi-stationary interaction stage.

The results of our previous investigations showed that a change of the channel cross section from round to cross-shaped in the case of a supersonic flow behind the outgoing shock wave led to an increase in the flow action upon the obstacle as a result of decreasing total pressure losses at the direct pressure jump. In the case of a subsonic flow behind the shock wave, the losses at this pressure jump are absent. The decrease in flow action upon the obstacle observed in this study is related to energy dissipation in a three-dimensional flow as a result of the interference of rarefaction and compression waves. This interference arises due to mass redistribution between various symmetry axes in the gaseous medium and due to the flow energy losses for the vortex formation at the channel edges [8].

REFERENCES

1. V. N. Malozemov, A. V. Omel'chenko, and V. N. Uskov, Prikl. Mat. Mekh. **62**, 1014 (1998).

2. T. V. Bazhenova, T. A. Bormotova, and V. V. Golub, Pis'ma Zh. Tekh. Fiz. **27** (16), 10 (2001) [Tech. Phys. Lett. **27**, 669 (2001)].

3. T. V. Bazhenova, V. V. Golub, and T. A. Bormotova, Teplofiz. Vys. Temp. **40**, 250 (2002).

4. T. V. Bazhenova, V. V. Golub, and A. L. Kotel'nikov, Pis'ma Zh. Tekh. Fiz. **29** (9), 69 (2003) [Tech. Phys. Lett. **29**, 385 (2003)].

5. T. V. Bazhenova, V. V. Golub, and A. L. Kotel'nikov, Teplofiz. Vys. Temp. **42**, 900 (2004).

6. H. Kleine, E. Ritzerfeld, and H. Gronig, in *Proceedings of the 19th International Symposium on Shock Waves, Marseille, 1993*, pp. 117–122.

7. A. Abe and K. Takayama, in *Proceedings of the National Symposium on Shock Waves Phenomena, Japan, 1988*, pp. 41–56.

8. T. V. Bazhenova, T. A. Bormotova, and V. V. Golub, Pis'ma Zh. Tekh. Fiz. **28** (16), 52 (2002) [Tech. Phys. Lett. **28**, 687 (2002)].

Translated by P. Pozdeev

Fullerene-Modified Dacron Track Membranes and Adsorption of Nitroxyl Radicals on These Membranes

Yu. F. Biryulin*, Yu. Yu. Kostetskiĭ, M. F. Kudoyarov, M. Ya. Patrova, and D. A. Sykmanov

Ioffe Physicotechnical Institute, Russian Academy of Sciences, St. Petersburg, 194021 Russia

TREM Research and Production Corporation, St. Petersburg, Russia

National University of Singapore, 10 Kent Ridge Crescent, 119260 Singapore

* e-mail: biryulin@mail.ioffe.ru

Received February 1, 2005

Abstract—Fullerene-containing track membranes have been created using a Dacron film with C_{60} fullerene molecules physically grafted on their surface. The membranes were studied by IR spectroscopy, scanning electron microscopy, atomic force microscopy, and electron paramagnetic resonance. The fullerene molecules form aggregates on the membrane surface. The experiments with adsorption of Tempo nitroxyl radical showed that the sorption capacity of fullerene-containing Dacron track membranes is significantly greater than that of the initial membranes. © 2005 Pleiades Publishing, Inc.

Introduction. Polymer membranes, including the polymer-based track membranes distinguished for their high selectivity, are widely used in solving practical tasks. The synthesis of track membranes on the basis of poly(ethylene terephthalate) (PETP) films (in particular, Lavsan or Dacron) and their successful applications are described in [1, 2].

This paper demonstrates the possibility of significantly increasing the sorption capacity of polymer track membranes by modifying them with fullerenes, which are known to possess a high sorption capacity in solutions [3]. Taking into account the high chemical stability of Dacron, we used a method based on the physical grafting of fullerene molecules on the membrane surface.

Materials and methods. The track membranes were manufactured using a 10-μm-thick commercial PETP film. The film was irradiated by heavy ions on a cyclotron accelerator at the Ioffe Physicotechnical Institute using equipment of the TREM Company [4]. This processing, followed by a special physicochemical treatment, yielded track membranes with a pore diameter of ~0.4 μm and a relative porosity of about 8%. The total surface area of these membranes, including the inner pore surfaces, was one order of magnitude greater than the external surface area of the initial PETP film.

The track membranes were modified by grafting C_{60} fullerene aggregates on the polymer surface. Some of the samples were exposed to UV radiation during fullerene deposition from a solution. It was suggested that the UV radiation might initiate the formation of bonds between C_{60} molecules and the PETP film, thus grafting fullerene on the membrane surface. In all experiments, the initial PETP film was used as the reference. The samples were studied by IR spectroscopy, scanning electron microscopy (SEM), atomic force microscopy (AFM), and electron paramagnetic resonance (EPR).

The sorption capacity of track membranes was studied using 2,2,6,6-tetramethyl-1-piperidinyloxy (Tempo) nitroxyl radical as the adsorbate. This compound has a cyclic structure close to that of the fullerene rings and produces a characteristic, readily identified EPR signal. The initial and modified track membranes were kept in 1 mM Tempo solution for two days and then extracted
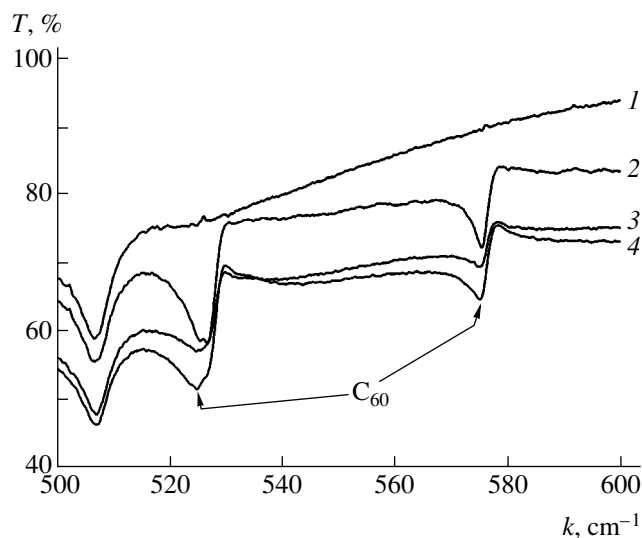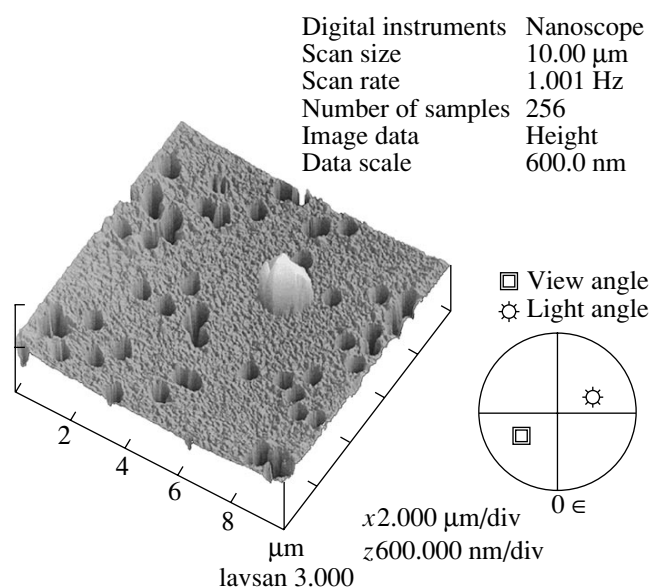

Fig. 1. IR absorption spectra of (*1*) initial and (*2–4*) fullerene modified track membrane (see text for explanations).

NUS_CHBE SEI 5.0 kV ×2.500   WD 8.6 mm

NUS_CHBE SEI 5.0 kV ×1.000   WD 8.4 mm
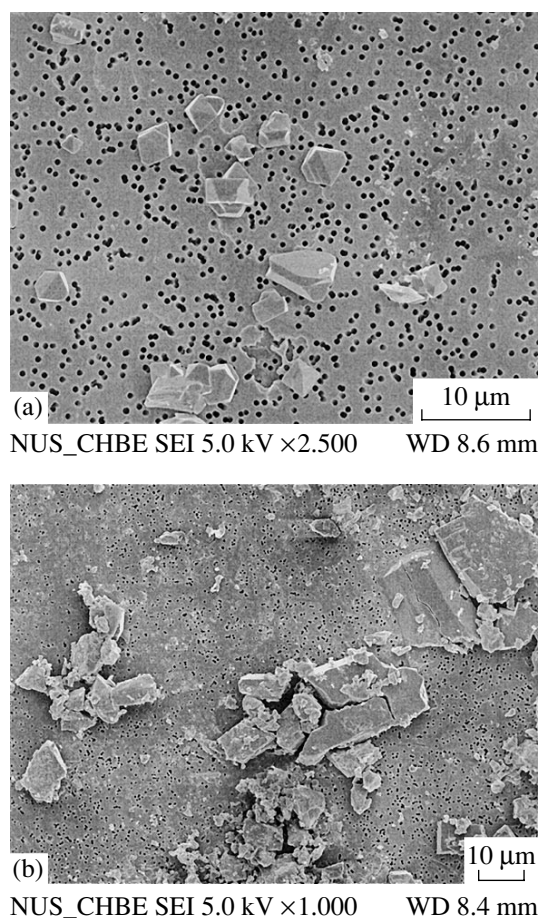
Fig. 2. Typical SEM micrographs of PETP track membranes modified with C_{60} fullerene: (a) without UV irradiation (note C_{60} single crystals of a regular shape); (b) with UV irradiation (C_{60} crystals are partly broken by internal stresses arising as a result of photopolymerization).

| Digital instruments | Nanoscope |
Scan size	10.00 μm
Scan rate	1.001 Hz
Number of samples	256
Image data	Height
Data scale	600.0 nm

Fig. 3. AFM image of the surface of a PETP track membrane modified by fullerene molecules without UV irradiation. The image reveals surface microrelief, pores in the track membrane, and a fullerene single crystal on the membrane surface.

and dried for one day in air at room temperature. The mount of adsorbed Tempo was evaluated using the relative intensity of the EPR signals of this radical.

Experimental results. The presence of fullerene molecules in the track membranes was confirmed by their IR absorption spectra (Fig. 1). The spectra of modified membranes display clear characteristic absorption bands at 527 and 576 cm^{-1}, which are known to belong to C_{60} fullerene molecules [5]. In Fig. 1, spectrum *1* refers to the initial track membrane, while spectra *2–4* characterize the track membranes modified in a fullerene solution without and with UV irradiation for various times. Spectrum *2* corresponds to a sample prepared without UV irradiation; spectrum *3* was obtained from a sample exposed to a UV dose equivalent to that used for the sensitization of latent tracks in the standard track membranes; and spectrum *4* characterizes a sample upon UV exposure to a twice greater dose. As can be seen, spectra *2–4* contain absorption bands characteristic of fullerenes, while spectrum *1* exhibits no such bands. As the exposure time increases, the bands due

to C_{60} shift to smaller wavenumbers, which may be indicative of a photopolymerization of fullerene molecules [6].

Figure 2 shows the typical SEM micrographs of fullerene-modified track membranes. Figure 2a shows the surface of a membrane not exposed to UV radiation during fullerene deposition. As can be seen, there are fullerene single crystals of a regular shape with the characteristic habit. The average crystal size is 4–5 μm, which is one order of magnitude greater than the pore diameter in the track membrane. Figure 2b shows a membrane modified under UV irradiation. In this case, the fullerene crystals exhibit no clear habit (such as in Fig. 2a) and appear as fractured. Apparently, UV irradiation led to a partial photopolymerization of fullerene crystals, and the arising internal stresses led to breakage of the crystals.

Figure 3 presents an AFM image of the surface of a track membrane modified by fullerene molecules without UV irradiation. The image shows pores in the track membrane and a fullerene crystal on the membrane surface. As can be seen, the characteristic height of the surface relief (~50 nm) is significantly smaller than the visible fullerene crystal size. The surface relief height on the initial (nonmodified) track membrane is somewhat lower (~30 nm). An increase in this value may be indicative of the formation of a fullerene film on the membrane surface.

Figure 4 shows the typical EPR spectrum of a fullerene-modified PETP track membrane after keeping in a Tempo solution and subsequent drying. The central peak in this spectrum belongs to C_{60} fullerene,
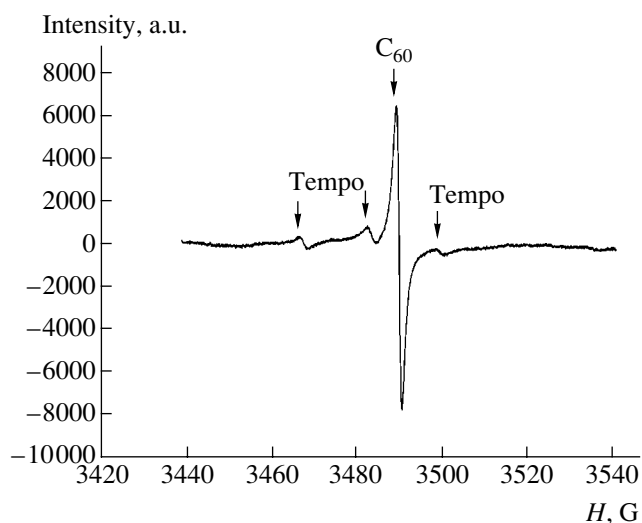
Fig. 4. The typical EPR spectrum of a fullerene-modified PETP track membrane after keeping in a Tempo solution and subsequent drying.

and the side peaks are due to the adsorbed Tempo nitroxyl radicals. Estimates of the spin density for the fullerene and Tempo signals give 6×10^{15} and 2×10^{14} spin/g, respectively. The g value for fullerene is 2.0041. A clear signal due to Tempo was observed only for fullerene-modified PETP membranes. In the spectrum of the initial track membrane, this signal was on a noise level, and a quantitative evaluation of the spin density was impossible. Therefore, the upper limit of the spin density of Tempo nitroxyl radicals adsorbed on the initial PETP membrane is at least one order of magnitude lower than that in the case of a modified membrane.

Conclusions. The above results clearly demonstrate that fullerene-modified PETP track membranes obtained using the proposed method possess a high sorption capacity and can be used in experiments on the adsorption of organic impurities. The results of charac-

terization by various techniques showed the presence of aggregates of C_{60} molecules in the surface of modified PETP track membranes. The experiments with the adsorption of Tempo nitroxyl radicals unambiguously showed that the sorption capacity of the fullerene-modified PETP track membranes significantly exceeds that of the nonmodified membranes. This property of the proposed membranes can be used for the filtration of aqueous solutions, as an additional stage of their purification from organic impurities.

REFERENCES

1. G. N. Flerov and V. S. Barashenkov, Usp. Fiz. Nauk **114**, 351 (1974) [Sov. Phys. Usp. **17**, 783 (1974)].

2. B. V. Mchedlishvili, in *Abstracts of Exhibition–Seminar on Track Membranes of New Type and Their Application in Biotechnology, Warsaw, 2003* (Mendeleev University of Chemical Technology, Moscow, 2004), p. 33.

3. V. I. Berezkin, I. V. Viktorovskiĭ, A. Ya. Vul', *et al.*, Fiz. Tekh. Poluprovodn. (St. Petersburg) **37**, 802 (2003) [Semiconductors **37**, 775 (2003)].

4. G. M. Gusinskiĭ, M. F. Kudoyarov, A. V. Matyukov, *et al.*, in *Proceedings of the All-Russia Conference on Membranes and Membrane-Related Technologies, Moscow, 1995*, p. 47.

5. A. V. Eletskiĭ and B. M. Smirnov, Usp. Fiz. Nauk **161**, 173 (1991) [Sov. Phys. Usp. **34**, 616 (1991)].

6. T. L. Makarova, Fiz. Tekh. Poluprovodn. (St. Petersburg) **35**, 257 (2001) [Semiconductors **35**, 243 (2001)].

Translated by P. Pozdeev

Photoluminescence of $Si_{0.9}Ge_{0.1}O_2$ and GeO_2 Films Irradiated with Silicon Ions

O. N. Gorshkov*, Yu. A. Dudin, V. A. Kamin, A. P. Kasatkin, A. N. Mikhaylov, V. A. Novikov, and D. I. Tetelbaum

Physicotechnical Research Institute, Nizhni Novgorod State University, Nizhni Novgorod, Russia
* e-mail: gorshkov@nifti.unn.ru
Revised manuscript received January 25, 2005

Abstract—We have studied the photoluminescence (PL) of GeO_2 and 90 mol % SiO_2–10 mol % GeO_2 films synthesized by method of RF magnetron sputtering and then irradiated with silicon ions and annealed. The PL of silicon-implanted GeO_2 films, related to the presence of Si nanocrystals (nc-Si), was observed for the first time. It is established that the transformation of the defect centers responsible for the PL in the spectral range 350–600 nm, as well as the formation of nc-Si emitting in the region of 700–800 nm, significantly depend on the matrix type. In particular, the PL intensity at 700–800 nm in 90 mol % SiO_2–10 mol % GeO_2 films is weak. The role of the isovalent substitution of Si and Ge atoms in the transformation of defect centers and the formation of nc-Si is discussed. © *2005 Pleiades Publishing, Inc.*

In recent years, much attention has been devoted to the synthesis and properties of silicon nanocrystals (nc-Si) in SiO_2 matrix, which is related to the search for new multifunctional materials for nano- and optoelectronics. Promising materials for such applications are offered by those based on GeO_2 and SiO_2–GeO_2 matrices. In contrast to silicon dioxide, these compounds change their refractive indices under the action of UV radiation (i.e., exhibit photosensitivity) and, hence, can be used as media for writing waveguides and gratings. The possibility of obtaining such matrices containing light-emitting nc-Si would greatly expand the range of their possible applications.

Light-emitting SiO_2 layers doped with germanium have been reported in [1–6]. However, there is no commonly accepted opinion concerning the nature of luminescence observed in such layers. In particular, it is still unclear whether this luminescence is related to the formation of Ge nanocrystals, Ge precipitates of other types, or some structural defects. As for GeO_2 layers, the formation of nanocrystals in such matrices and their luminescent properties remain practically unstudied.

In this context, we have investigated the photoluminescence (PL) of GeO_2 and 90 mol % SiO_2–10 mol % GeO_2 films irradiated with silicon ions. We also studied the effect of irradiation dose and subsequent annealing on the PL spectra. The PL of silicon-implanted GeO_2 films in the spectral range typical of nc-Si was observed for the first time.

The films of 90 mol % SiO_2–10 mol % GeO_2 (SiO_2–GeO_2) with a thickness of $d = 0.25$ μm and the films of GeO_2 with $d = 0.3$ μm were deposited onto fused quartz and silicon substrates by means of RF magnetron sput-

tering of the corresponding cold-pressed targets. The deposited films were implanted with 100-keV Si^+ ions at room temperature to various doses in the range $\Phi = 3 \times 10^{16}$–3×10^{17} cm^{-2}. The average projected range R_p of silicon ions in the irradiated materials according to the results of calculations using the TRIM-95 program was 0.12 μm for SiO_2–GeO_2 films and 0.08 μm for GeO_2 films. The postimplantation annealing of samples was performed for 2 h at 1000°C in a dry nitrogen atmosphere. The PL was excited at room temperature by radiation of a pulsed nitrogen laser operating at 337 nm with a power density of ~100 mW/cm^2.

Figure 1 shows the PL spectra of SiO_2–GeO_2 films. As can be seen, the spectra of the initial films contain a PL band with a maximum at ~400 nm. In the literature, the PL bands in the range from 300 to 500 nm for such films are assigned to the emission from complex oxygen-deficient germanium (ODG) centers [7, 8]. According to [1, 9–14], these centers may represent neutral oxygen vacancies or Ge^{2+} centers (Ge atoms twofold coordinated by oxygen). The emission from ODG centers is usually excited by photons with an energy of ~5 eV. However, the PL in the region of ~400 nm in SiO_2–GeO_2 films was also observed upon excitation with radiation of a nitrogen laser [15]. This emission, as well as that observed in our samples, can be related both to the absorption of laser radiation at $\lambda = 377$ nm [7] and to a two-photon absorption process [11].

After the irradiation of SiO_2–GeO_2 films with Si^+ ions to a small dose ($\Phi = 3 \times 10^{16}$ cm^{-2}), the intensity of the PL band at ~400 nm exhibited a sharp increase, which can be explained by the rupture of oxygen bonds
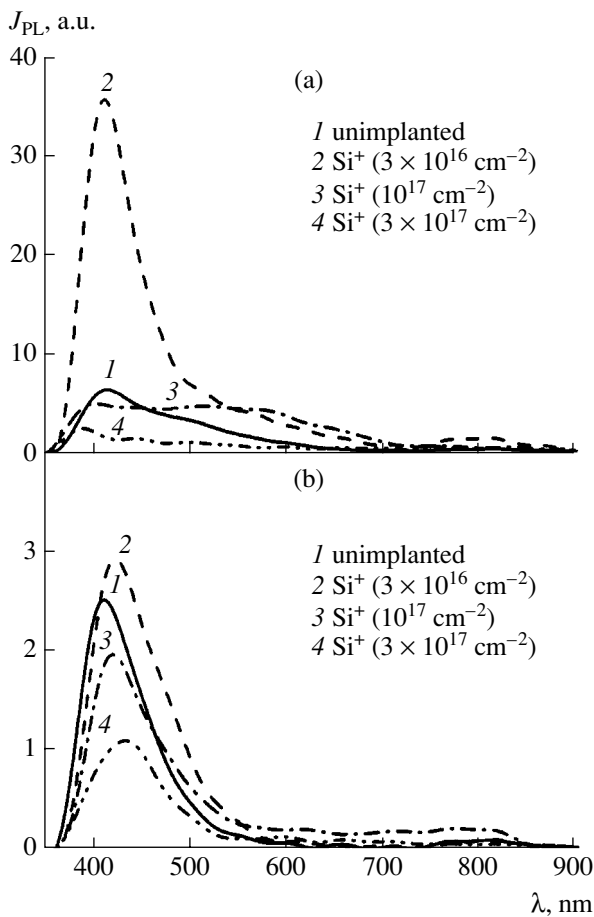
Fig. 1. PL spectra of 90 mol % SiO_2–10 mol % GeO_2 films in various states: (a) initial film (*1*) and the samples irradiated with 100-keV Si^+ ions to doses $\Phi = 3 \times 10^{16}$ (*2*), 1×10^{17} (*3*), and 3×10^{17} cm^{-2} (*4*); (b) same as in (a) plus additional annealing for 2 h at 1000°C. The PL intensities are normalized to the same scale for all curves.

and the resulting increase in the concentration of ODG centers [16]. However, an increase in the radiation dose to $\Phi = 1 \times 10^{17}$ cm^{-2} led to a decrease in the PL band intensity and an increase in its width. The decrease in intensity can be related to the fact that implanted silicon atoms may partly occupy oxygen vacancies adjacent to Si and/or Ge atoms. This leads to the formation of atomic chains of the Si–Si–Si, Ge–Si–Si, and Ge–Si–Ge types, which do not possess the properties of the ODG centers. According to [2], such chains emit in the region of 500–600 nm, and this may account for the appearance of a shoulder in this region of the PL spectrum of silicon implanted samples. Further decrease in the PL intensity with the irradiation dose increased to $\Phi = 3 \times 10^{17}$ cm^{-2} is probably related to the accumulation of defects behaving as the centers of nonradiative recombination.

Figure 1 also shows the PL spectra of SiO_2–GeO_2 films measured after postimplantation annealing at 1000°C. As can be seen, the PL band at 400 nm is

retained upon annealing, but the intensity of this band decreases (to various extents, depending on the implantation dose). Apparently, the thermal treatment restores the oxygen bonds and decreases the concentration of ODG centers. It should be noted that annealing also decreases the PL intensity for the initial (unimplanted) samples. This is additional evidence for the partial healing of oxygen vacancies. The shoulder at 500–600 nm practically vanishes after annealing, which implies (within the framework of the interpretation adopted) the decay of the Si–Si–Si, Ge–Si–Si, and Ge–Si–Ge chains. Analogous behavior was observed in SiO_2 films implanted with Ge^+ and was explained by the annealing-induced decomposition of so-called "nonphase" Ge inclusions [2].

The PL spectra of SiO_2–GeO_2 films measured after postimplantation annealing exhibit additional weak bands in the region of 700–800 nm, which is usually assigned to the emission of nc-Si [17–20]. This spectral feature will be considered in more detail below.

We have also found a number of features in the PL spectra of GeO_2 films. As can be seen from Fig. 2, the initial films emit (similarly to the SiO_2–GeO_2 films) in the violet and blue spectral regions, but this emission is characterized by a generally broader PL band extended up to ~700 nm. Apparently, this band is related to the presence of (i) centers analogous to ODG in the SiO_2–GeO_2 matrix and (ii) clusters of the type of nonphase Ge inclusions [2]. Also similar to the case of SiO_2–GeO_2 films, the implantation of Si^+ ions into GeO_2 films to relatively small doses leads to an increase in the PL intensity in this spectral region, while greater doses produce a decrease in this emission, this drop being especially noticeable in the short-wavelength region. At longer wavelengths, the tendency to decrease in the PL intensity is less pronounced as compared to that in SiO_2–GeO_2 films.

The most interesting fact is that the PL spectra of GeO_2 films implanted with Si^+ ions to large doses display a band in the region of 700–800 nm (characteristic of nc-Si) even without postimplantation annealing. It is unlikely that this emission is due to germanium nanocrystals. Indeed, such nanocrystals (even if they were formed in the oxide matrix) do not emit in this spectral range [2, 21, 22]. Moreover, the nanocrystals of germanium obtained by epitaxy on silicon substrates [23] exhibited luminescence in different spectral regions. As can be seen from Fig. 2, postimplantation annealing decreases the short-wavelength PL intensity (which is explained by the decomposition of defects and nonphase inclusions), while the band at 700–800 nm exhibits narrowing and growth (after which it is only 2–3 times smaller than the PL band observed for SiO_2 films with nc-Si that is formed by 150-keV Si^+ implantation to $\Phi = 10^{17}$ cm^{-2} followed by 2-h annealing at 1000°C [18]). The intensity of this PL band in the spectrum of silicon-implanted GeO_2 decreases (similarly to

the case of SiO_2 matrix with nc-Si [18, 20]) when the implantation dose is increased to 3×10^{17} cm^{-2}. Thus, the PL band at 700–800 nm can be naturally attributed to the emission from nc-Si. It is suggested that the position of this band is the same (despite the different matrix) as that for nc-Si obtained by other methods (such as ion implantation of Si$^+$ into SiO_2, various deposition techniques, porous silicon formation, etc.).

The basis of this assumption is the fact that, irrespective of the method of nc-Si formation, the PL band at 700–800 nm is nearly always observed for the films with nc-Si. This emission is usually attributed either to the interband transitions in nc-Si [17, 18, 24] or to the transitions involving energy levels and/or vibrational states localized in the SiO_x shell, at the nc-Si-matrix interface [20, 25, 26]. Such a shell is always present irrespective of the method of obtaining layers with nc-Si inclusions. For the former mechanism (interband transitions), the position of the nc-Si emission band must weakly depend on the matrix type and has to be determined only by the nc-Si (quantum dot) size, provided that the energy barrier height between nc-Si (greater than 3 nm) and the matrix are sufficiently large [27]. For the second mechanism (involving SiO_2 shell), significant changes in the nc-Si emission band position will be absent provided that nc-Si inclusions in GeO_2 matrix are in fact surrounded by SiO_x shells. The formation of such a shell is quite possible due to the higher (compared to germanium) affinity of silicon to oxygen and due to the presence of a large amount of defects (including unbound oxygen) around nc-Si. Thus, irrespective of the particular mechanism of PL, the band at 700–800 nm can be assigned with high confidence to the nc-Si luminescence. Of course, a reliable proof of this hypothesis will require using more direct methods, such as X-ray photoelectron spectroscopy and X-ray diffraction.

If we admit that the PL band at 700–800 nm is really due to nc-Si, the question arises as to why the formation of nc-Si is less pronounced in the mixed SiO_2–GeO_2 oxide matrix than in the "pure" GeO_2 film. This behavior can be related to the fact that the atomic (ionic) radius of Ge is significantly greater than that of Si. For this reason, Ge atoms in the mixed oxide induce local elastic stresses, which increase the free energy. Under such conditions, it is energetically more favorable for implanted (i.e., excess) silicon atoms to replace germanium atoms (and thus relieve the internal stresses) than to form nc-Si inclusions. In pure GeO_2 matrix, such local internal stresses are absent; moreover, the substitution of silicon for germanium would give rise to these stresses. For these reasons, implanted silicon atoms precipitate in the form of nc-Si. Note, however, that the fact of nc-Si formation in GeO_2 is, nevertheless, not a trivial result. The Si–O bond energy is 18% higher than that of Ge–O bonds [28]. From this standpoint, the excess silicon atoms must displace germanium and occupy the lattice sites. However, this process requires
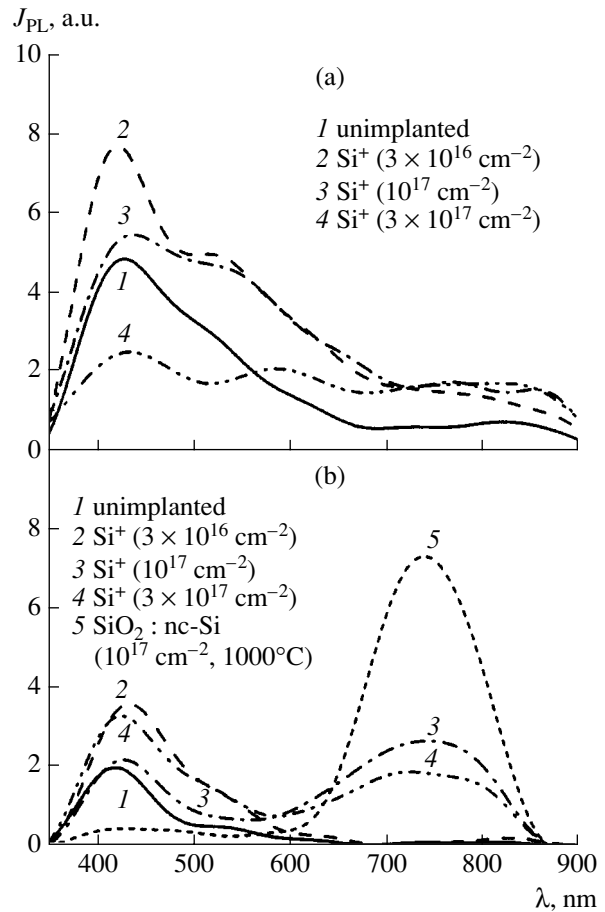
Fig. 2. PL spectra of GeO_2 films in various states: (a) initial film (*1*) and the samples irradiated with 100-keV Si$^+$ ions to doses $\Phi = 3 \times 10^{16}$ (*2*), 1×10^{17} (*3*), and 3×10^{17} cm^{-2} (*4*); (b) same as in (a) plus additional annealing for 2 h at 1000°C; (*5*) the spectrum of a SiO_2 film with nc-Si formed by irradiation with 100-keV Si$^+$ ions to $\Phi = 10^{17}$ cm^{-2} followed by annealing for 2 h at 1000°C [18]. The PL intensities are normalized to the same scale for all curves.

overcoming a certain potential barrier (kinetic factor), which can be higher than the barrier for the nc-Si formation. Then, especially in the case of a high concentration of excess silicon, the coagulation of silicon atoms and nc-Si formation will proceed more rapidly than the displacement of germanium. In addition, the aforementioned thermodynamic factor related to the appearance of local elastic stresses still works in favor of silicon precipitation.

Thus, the formation of nc-Si significantly depends on the state and composition of the initial oxide matrix. Apparently, the presence of high concentrations of an isovalent impurity with an atomic (ionic) radius significantly different from that of the host atoms hinders the formation of nanocrystals. However, in "pure" SiO_2 and GeO_2 matrices, the formation of luminescent nc-Si is energetically favorable. For this reason, GeO_2 can be a more promising matrix than mixed germanate-silicate

glasses for the synthesis of implanted multifunctional materials.

REFERENCES

1. L. Rebohle, J. von Borany, R. A. Yankov, *et al.*, Appl. Phys. Lett. **71**, 2809 (1997).

2. G. A. Kachurin, L. Rebole, I. E. Tyschenko, *et al.*, Fiz. Tekh. Poluprovodn. (St. Petersburg) **34**, 23 (2000) [Semiconductors **34**, 21 (2000)].

3. Y. Maeda, N. Tsukamoto, Y. Yazawa, *et al.*, Appl. Phys. Lett. **59**, 3168 (1991).

4. Y. Kanemitsu, H. Uto, Y. Masumoto, *et al.*, Appl. Phys. Lett. **61**, 2187 (1992).

5. Y. Maeda, Phys. Rev. B **51**, 1658 (1995).

6. S. Okamoto and Y. Kanemitsu, Phys. Rev. B **54**, 16421 (1996).

7. V. B. Neustruev, in *Fiber-Optical Technologies, Materials and Devices*, Ed. by E. M. Dianov and A. A. Makeev (Kaluga, 2000), No. 3, pp. 12–34 [in Russian].

8. W. Skorupa, L. Rebohle, and T. Gebel, Appl. Phys. A **76**, 1049 (2003).

9. H. Nishikawa, T. Shiroyama, R. Nakamura, *et al.*, Phys. Rev. B **45**, 586 (1992).

10. H. Hosono, Y. Abe, D. L. Kinser, *et al.*, Phys. Rev. B **46**, 11445 (1992).

11. J. Nishii, K. Fukumi, H. Yamanaka, *et al.*, Phys. Rev. B **52**, 1661 (1995).

12. L.-S. Liao, X.-M. Bao, X.-Q. Zheng, *et al.*, Appl. Phys. Lett. **68**, 850 (1998).

13. R. Tohmon, J. Shimogaichi, H. Mizuno, *et al.*, Phys. Rev. Lett. **62**, 1388 (1989).

14. M. Gallagher and U. Osterberg, Appl. Phys. Lett. **63**, 2987 (1993).

15. I. E. Tyschenko, A. B. Talochkin, A. G. Cherkov, *et al.*, Fiz. Tekh. Poluprovodn. (St. Petersburg) **37**, 479 (2003) [Semiconductors **37**, 462 (2003)].

16. P. J. Hughes, A. P. Knights, B. L. Weiss, *et al.*, Appl. Phys. Lett. **74**, 3311 (1999).

17. K. S. Min, K. V. Scheglov, C. M. Yang, *et al.*, Appl. Phys. Lett. **69**, 2033 (1996).

18. D. I. Tetelbaum, O. N. Gorshkov, S. A. Trushin, *et al.*, Nanotechnology **11**, 295 (2000).

19. G. A. Kachurin, I. E. Tischenko, K. S. Zhuravlev, *et al.*, Nucl. Instrum. Methods Phys. Res. B **122**, 571 (1997).

20. B. Garrido Fernandez, M. Lopez, C. Garcia, *et al.*, J. Appl. Phys. **91**, 798 (2002).

21. M. Zacharias and P. M. Fauchet, Appl. Phys. Lett. **71**, 380 (1997).

22. M. Zacharias, R. Weigand, B. Dietrich, *et al.*, J. Appl. Phys. **81**, 2384 (1997).

23. O. P. Pchelyakov, Yu. B. Bolkhovityanov, A. V. Dvurechenskiĭ, *et al.*, Fiz. Tekh. Poluprovodn. (St. Petersburg) **34**, 1281 (2000) [Semiconductors **34**, 1229 (2000)].

24. S. Guha, S. B. Qadri, R. G. Musket, *et al.*, J. Appl. Phys. **88**, 3954 (2000).

25. T. Shimizu-Iwayama, K. Fujita, S. Nakao, *et al.*, J. Appl. Phys. **75**, 7779 (1994).

26. K. S. Zhuravlev, A. M. Gilinsky, and A. Yu. Kobitsky, Appl. Phys. Lett. **73**, 2962 (1998).

27. V. A. Burdov, Fiz. Tekh. Poluprovodn. (St. Petersburg) **36**, 1233 (2002) [Semiconductors **36**, 1154 (2002)].

28. V. I. Vedeneev *et al.*, in *Energy of Chemical Bond Breakage, Ionization Potentials and Electron Affinity* (Izd. Akad. Nauk SSSR, Moscow, 1962) [in Russian].

Translated by P. Pozdeev

Anisotropy of the Magnetic Properties of Nickel Clusters

S. A. Nikitchuk*, M. V. Lokhanin, A. V. Prokaznikov**, N. A. Rud', and V. B. Svetovoi

Yaroslavl State University, Yaroslavl, Russia
Institute of Microelectronics and Informatics, Russian Academy of Sciences, Yaroslavl, Russia
*e-mail: *nikitchuk_sergey@mail.ru; **prokaznikov@mail.ru*
Received February 16, 2005

Abstract—A technology of polygonal nickel microclusters aligned in the same direction has been developed. The new technology is based on the incorporation of nickel from a salt solution into a porous silicon matrix. Anisotropic magnetic properties of nickel microclusters formed in the silicon matrix are established and studied for the first time. © 2005 Pleiades Publishing, Inc.

In recent years, much attention has been devoted to the properties of small metal particles. This interest is related both to the good prospects for their practical applications and to the deeper insight they may provide into basic principles of the organization of matter [1–5]. Small particles (clusters) occupy an intermediate position between atomic and crystalline states of solids (see, e.g., [5]). The basic properties of substances are related to the possible packing of atoms in clusters having various geometric shapes [5], which determine the symmetry and the physical characteristics of clusters. An example is offered by the class of fullerenes possessing a number of unusual properties (see, e.g., [6]). Detailed investigations can give information about the properties of clusters and provide an answer to the question as to why regular cluster structures are formed (occupying an intermediate position between individual atoms and molecules and macroscopic crystals). In particular, the magnetic properties of clusters may significantly differ from those of the same substances in the macroscopic crystalline state because the contribution due to the surface of these small objects becomes comparable to the bulk contribution [5, 7].

The possible spectrum of practical application is also very broad: clusters can be used as catalysts, surface nanostructures [1], ensembles of superparamagnetic particles incorporated in dielectric matrices [2], etc. The special magnetic properties of nanoclusters of various ferromagnetic materials can also find important applications, in particular, in rapidly developing magnetic computer memory (MRAM) devices [3]. The technology described below will provide the arrays of vertical metallized structures ordered over the material surface, with broad prospects for their implementation in various microelectronic systems. Investigations into the magnetic properties of clusters related to spin effects are of interest with a view to the development of quantum computers.

This paper presents the results of our investigation into the magnetic properties of nickel (Ni) microclusters forming extended chains. The technology of such clusters is essentially as follows. In the first step, a layer of porous silicon was formed on the basis of commercial (100)-oriented single crystal silicon (KEF-4.5 grade) wafers. These layers with vertical pores were formed by conventional anodizing in a mixed hydrofluoric acid solution with isopropanol (1 : 1, v/v) as described in [8]. Then, the polarity was changed and nickel was deposited into the pores from a mixed solution of $NiCl_2 \cdot 6H_2O$ (300 g/l) and H_3BO_3 (38 g/l).

As known, nickel can form various crystalline structures (see, e.g., [1] and references therein). In our case, the initial as-deposited structure comprised (i) a thick layer of nickel on the surface of a porous nickel substrate, (ii) long chains of polygonal Ni clusters formed in pores of the upper third part of the porous silicon layer (with a certain orientation of their crystallographic axes relative to the pore channels), (iii) a deposit on the pore walls, (iv) separate Ni clusters formed in the middle third part of the porous silicon layer, and (v) rare individual Ni clusters in the bottom third part of the porous layer. Figure 1 shows typical micrographs of the transverse cleavages of nickel structures in a porous silicon substrate, which show evidence for the existence of polygonal Ni clusters with dimensions up to a few microns.

As a rule, the properties of bulk nickel samples are determined by their structure representing a face centered cubic (fcc) lattice or a hexagonal close packed (hcp) lattice [1]. In the fcc nickel phase, the [111] crystal axis corresponds to the easy magnetization direction, whereas the [100] axis is the hard magnetization direction with a greater magnetic anisotropy energy [9]. The clusters had predominantly the shape of polygons with polyhedral cross sections (for the most part, pen-
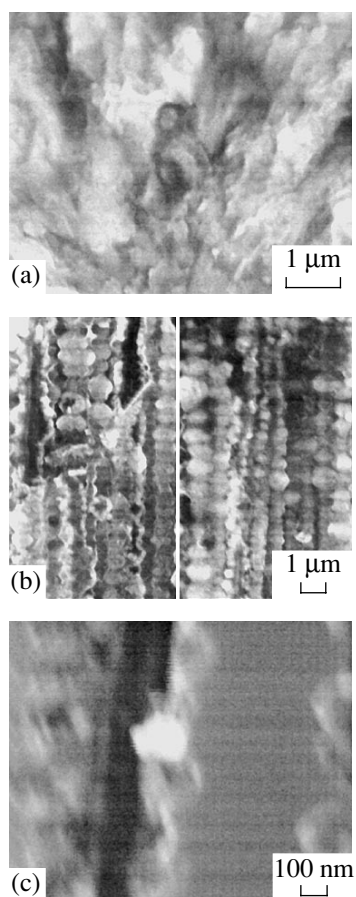
Fig. 1. Micrographs of the transverse cleavages of nickel-containing structures: (a) a thick layer of nickel removed from the surface of a porous nickel substrate after Ni deposition from a solution; (b) vertical columns (oriented along the normal to the silicon substrate surface) of polygonal Ni clusters formed in pores of the porous silicon matrix (an arrow indicates one cluster with a negative curvature); (c) a single Ni cluster formed in one of the pores.

tagons and hexagons), sometimes with a negative curvature of the surface (see Fig. 1). These characteristic features are indicative of the possible icosahedral (*Ih*) and dodecahedral (*Dh*) structures of the clusters (see, e.g., [1, 10]). It should be noted that pores exhibit a special (vertical) direction, so that the crystallographic axis of all Ni clusters in the upper third part of the porous layer have a practically identical orientation. This circumstance favors the manifestation of the anisotropic properties descried below. Should the clusters be randomly arranged, such anisotropic effects would hardly be observed as a result of the angular averaging. As is known (see, e.g., [1]), there is a certain discrepancy between theoretical papers, predicting the stability of the Au and Ni clusters in the *Ih* and *Dh* phases only for very small clusters (containing below 100 atoms), and the results of experimental investigations, which show that both *Ih* and *Dh* clusters exist with the number of atoms reaching up to several thousand. Figure 1 clearly

illustrates the possibility of obtaining polygonal clusters with dimensions on the order of microns.

The magnetic properties of Ni clusters were studied on a setup (vibrating-sample magnetometer) comprising a He–Ne laser, a Michelson interferometer, a positive lens, a tightly fastened silicon cantilever with a mirror-smooth surface, and two photodetectors with differential amplifiers. The magnetic field was generated by a cylindrical SmCo magnet, which was magnetized across the diameter and oriented with its side surface toward the sample studied. The field of such a magnet is well known and is characterized by a field component at the pole on the magnet surface on the order of 0.8 T. In order to exclude the effect of sample weight variations as a result of adsorption, the sample was glued with a wax to the silicon cantilever so that the porous silicon layer was facing downward. The main element of the magnetometer—silicon cantilever—occurred in a vacuum chamber with a volume of several cubic centimeters, where it was mounted so that the rear mirror-smooth side was in the focus of the lens and formed the working arm of the Michelson interferometer. The cantilever was excited by a piezotransducer for 2–3 s at a nearly resonance frequency, after which the excitation was terminated and the free oscillations were monitored for 3–4 s. The data from the interferometer photodetectors were digitized, fed into a computer, and processed by a special program, which calculated the fundamental frequency of the cantilever with a sample. All the magnetometer setup was mounted on a shock-absorbing base.

When the sample mounted on the cantilever end occurs in a magnetic field generated by the SmCo magnet (see the inset to Fig. 2a), it is possible to determine the force acting on the sample and calculate the derivative of this force. Using a solution of the general equation describing the transverse oscillations of a cantilever with a lumped magnetic force acting upon the end, it is possible to show that the gradient of this force shifts the fundamental frequency of the cantilever. Thus, by measuring this frequency shift, it is possible to determine the force acting upon the sample and the magnetic characteristics of a substance occurring in the field.

In order to study the properties of Ni nanoclusters, we removed the thick nickel layer from the plate and performed magnetic measurements separately for this continuous layer and the residual porous matrix with incorporated nickel particles. Figure 2 shows plots of the relative variation in the frequency of oscillations of the cantilever bearing the sample versus the angle between the magnetic moment of the magnet and the normal to the sample surface (see the inset to Fig. 2a). The curve obtained for the removed continuous nickel layer (depicted in Fig. 1a) has a shape resembling a cosine curve (Fig. 2a). In this case, the magnetization follows the magnetic field. In contrast, the curve for a sample (depicted in Fig. 1b) of nickel incorporated into
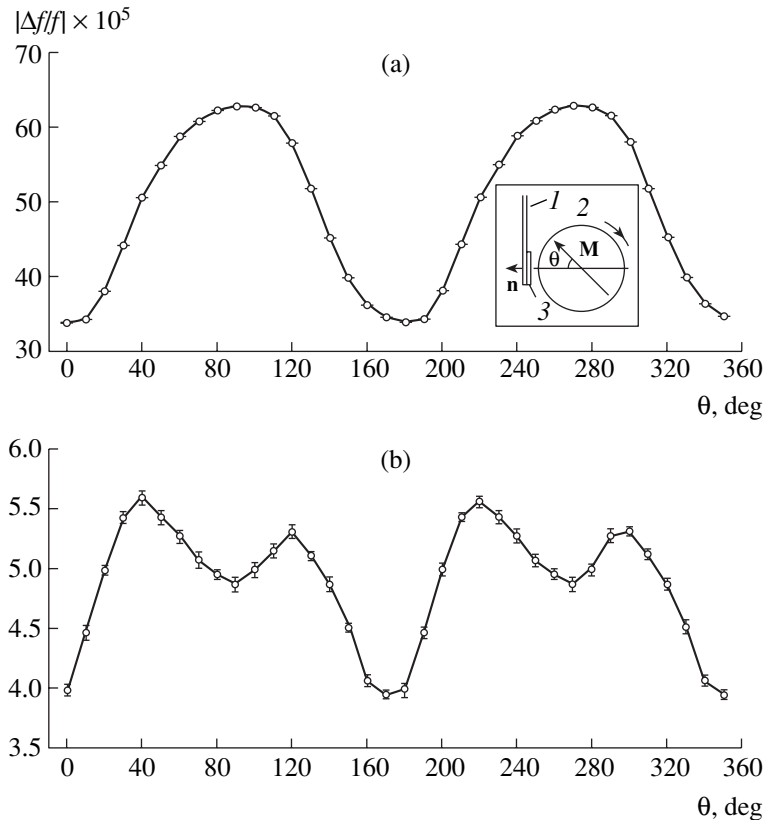
Fig. 2. Plots of the relative variation in the frequency of oscillations of the cantilever (see the inset, *1*) bearing the sample versus the angle between the magnetic moment of the SmCo magnet (*2*) and the normal to the sample surface (*3*) for (a) a continuous nickel layer removed from the porous silicon and (b) a sample of nickel incorporated into a porous silicon matrix. The inset shows the mutual arrangement of the sample and the magnet.

a porous silicon matrix with a completely removed continuous Ni layer appears as a cosine curve of double frequency, with a change in the amplitude for the magnetic fields oriented along ($\theta = 0°$, $180°$) and across ($\theta = 90°$, $270°$) the pores and the aligned columns composed of Ni clusters (Fig. 2b). It should be noted that the sensitivity of our experimental setup was $\Delta f/f_0 \approx 10^{-6}$, where f_0 is the fundamental frequency of the cantilever in a zero magnetic field.

A similar magnetometric technique with a silicon cantilever was used in [11] for studying Ni atoms incorporated into organic molecules so as to form square sublattices. The signal dependence on the magnitude and direction of magnetic field observed in [11] was analogous to our data for the continuous nickel sample. It should be noted that no oriented polygonal clusters were present in the samples studied in [11] and no anisotropic effects (such as that described above) were observed.

Specific features in the behavior of the cluster structure in our samples can be determined by two factors. First, by the magnetic symmetry of icosahedral (*Ih*) and dodecahedral (*Dh*) clusters having easy axes different from those in the fcc lattice. Second, by the possible formation of domains with dimensions comparable

with the dimensions of clusters proper (monodomain clusters), which exhibit specific rotations in the magnetic field. If a cluster structure possesses two easy axes in the angular interval from $0°$ to $180°$, the results of our measurements become quite clear.

It should be noted that observation of the effects described above is facilitated by the predominant orientation of the crystallographic axes of Ni clusters in a certain direction with respect to the normal to the sample surface (see the inset in Fig. 2a). This fact confirms the convenience of the proposed technology for obtaining cluster structures based on porous silicon matrices. Should the clusters be randomly arranged, the observation of anisotropic effects will be considerably complicated as a result of the angular averaging over the directions of magnetic axes of Ni clusters.

To summarize, we proposed a rather simple technology of polygonal Ni microclusters with an identical orientation of crystallographic axes. The technology is based on the deposition of metallic nickel from a mixed solution of $NiCl_2 \cdot 6H_2O$ and H_3BO_3 into vertical pores preliminarily formed in a silicon matrix. We established and studied the anisotropic magnetic properties of polygonal nickel microclusters with dimensions up to a few microns.

REFERENCES

1. Yu. Ya. Gafner, S. L. Gafner, and P. Entel', Fiz. Tverd. Tela (St. Petersburg) **46**, 1287 (2004) [Phys. Solid State **46**, 1327 (2004)].

2. G. I. Frolov, Zh. Tekh. Fiz. **74** (7), 102 (2004) [Tech. Phys. **49**, 909 (2004)].

3. A. Morozov and V. Grigor'ev, Élektron. Komponenty, No. 3, 2 (2000).

4. H. M. Duan, X. G. Gong, Q. Q. Zheng, *et al.*, J. Appl. Phys. **89**, 7308 (2001).

5. T. P. Martin, Phys. Rep. **273**, 199 (1996).

6. A. V. Eletskiĭ and B. M. Smirnov, Usp. Fiz. Nauk **163**, 33 (1993) [Phys. Usp. **36**, 202 (1993)].

7. E. De Biasi, C. A. Ramos, and R. D. Zysler, Phys. Rev. B **65**, 144416 (2002).

8. E. Yu. Buchin and A. V. Prokaznikov, Mikroélektronika **27**, 107 (1998).

9. S. V. Vonsovskiĭ, *Magnetism* (Nauka, Moscow, 1971; Wiley, New York, 1974).

10. J. A. Ascencio, M. Perez, and M. Jose-Yacaman, Surf. Sci. **447**, 73 (2000).

11. R. Koch, O. Waldman, P. Miller, *et al.*, Phys. Rev. B **67**, 094407 (2003).

Translated by P. Pozdeev

Composition and Photoelectric Properties of Epitaxial Silicon Layers Grown from a Tin-Based Solution Melt of Technical Silicon

B. Sapaev, A. S. Saidov, and Sh. I. Ibragimov

Physicotechnical Institute, "Solar Physics" Research and Production Corporation,
Academy of Sciences of the Republic of Uzbekistan, Tashkent, Uzbekistan
e-mail: bayram@physic.uzsci.net
Revised manuscript received January 27, 2005

Abstract—Epitaxial layers of $Si_{1-x}Sn_x$ ($0 < x < 0.04$) solid solutions on silicon substrates were grown by liquid phase epitaxy from a tin-based solution melt of technical silicon. The distribution of components over the surface and in depth of the $Si_{1-x}Sn_x$ epilayers was determined. The photoelectric properties of obtained epilayers and heterostructures were studied. The results of these investigations showed that the obtained epilayers are structurally perfect and contain no metallic inclusions. The photosensitivity spectrum of obtained silicon epilayers is shifted toward longer wavelengths as compared to the spectra of silicon films obtained by usual methods. © *2005 Pleiades Publishing, Inc.*

The standard chloride-silane technology of obtaining epitaxial silicon layers has not been significantly modified in the approximately 35 years in which this method has found practical application. This process retains all the drawbacks inherent in the chemical technology of 1950s: high energy consumption, low silicon yield (6–10%), and poor ecological safety. For this reason, it is still important to develop the synthesis of silicon epilayers with a quality acceptable for the electronic industry using the method of liquid phase epitaxy (LPE) from technical silicon melts.

This Letter presents the results of an experimental investigation of the composition and photoelectric properties of epitaxial layers grown by LPE from a tin-based solution melt of technical silicon.

The initial material was technical silicon of the Kr3 grade. The composition of samples of the initial material taken from different sides and various points of the ingot were analyzed with the aid of a JSM 5910LV electron probe microanalyzer (JEOL, Japan). Some results of these analyses, showing the content of impurities at various points of the initial silicon ingot, are given in Table 1. After preparation of the initial technical silicon solution, silicon substrates with a diameter of 20 mm were introduced into a reactor. The solubility of technical silicon in tin was determined in preliminary experiments. After accomplishing all preliminary procedures, the reactor chamber was evacuated to a residual pressure of 5×10^{-2} Torr. The epilayers were grown from a limited volume of tin-based solution melt confined between substrates in a palladium-purified (palladium 15T) hydrogen (H_2) atmosphere.

Prior to immersion into a solution melt, the substrates were kept at a distance of 5 mm above the melt surface. The solution melt was heated to a certain preset temperature and then kept at this temperature for 30 min in order to provide for complete homogenization. Then, the substrates were immersed into the liquid phase so that the melt filled the gap between the substrates. Finally, the substrates were extracted from the solution melt and returned to the initial position, after which the temperature was automatically decreased according to a special program so as to provide for the optimum crystallization conditions. The optimum rate

Table 1. Composition of technical silicon

Analyzer position	Content of components, wt %											
	Si	Na	Mg	Al	P	S	K	Ca	Ti	Mn	Fe	Total
1	97.3	0.00	0.00	2.31	0.00	0.00	0.07	0.00	0.20	0.00	0.13	100
2	39.49	0.15	0.00	1.29	4.84	0.34	0.13	0.00	21.90	0.43	31.43	100
3	39.71	0.00	0.30	23.32	0.14	0.27	0.94	5.75	0.00	0.42	29.15	100
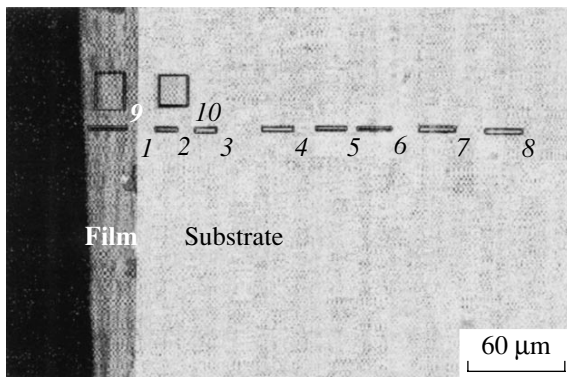
Fig. 1. Scanning micrograph of the transverse section of a *p*-Si–*n*-Si(Sn) structure measured using the JSM 5910LV electron probe microanalyzer.
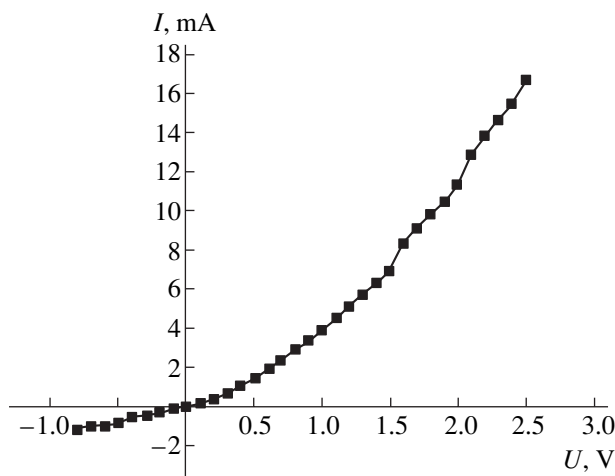
Fig. 2. The typical *I–U* curve measured at room temperature for a *p*-Si–*n*-Si(Sn) structure grown from a tin-based solution melt of technical silicon.

of solution melt cooling was 0.6–1.0 K/min. When the temperature decreased to a certain value, a centrifuge was switched on and the residue of the solution melt was ejected from the gap between horizontal substrates.

After the chemical and mechanical treatments of the obtained epilayer, the composition of grown material was quantitatively analyzed at various points in a cleaved section and over the surface of the $Si_{1-x}Sn_x$

film. The typical results of such analyses are presented in Table 2. These analyses were performed using the aforementioned electron probe microanalyzer and an SPS-3000 X-ray spectrum analyzer (Siemens, Germany) ensuring the detection of impurities on a level of $10^{-4}\%$. The experimental results obtained with these instruments were very similar. A comparison of the compositions of the initial (technical) silicon and the epilayer shows that the content of impurities in the latter case is significantly decreased (cf. Tables 1 and 2), while the distribution of silicon over the substrate surface becomes more homogeneous and close to the average level of 99.2%.

The epitaxial material is most effectively purified from the impurities such as As, P, Ca, Ti, and Fe. We believe that this phenomenon is related to the gettering properties of tin [1]. Figure 1 shows a micrograph of the transverse section of a *p*-Si–*n*-Si(Sn) structure measured using the JSM 5910LV electron probe microanalyzer in the scanning mode. It should be noted that no macroscopic defects and second phase inclusions were observed in depth of the epitaxial layer.

We have studied the photoelectric properties and measured the current versus voltage (*I–U*) curves of the obtained epilayers. For the electric measurements, the samples were provided with InSn alloy contacts. As can be seen from Fig. 2, the *I–U* curve has a quite standard shape. The reverse branch rapidly exhibits saturation, while the forward branch is exponential and extends up to 2.5 V, which is unambiguous evidence for the presence of either a significant serial resistance or an inverse layer formed during the LPE process. In both cases, the *I–U* curve is described by the expression [2, 3]

$$I = I_c e^{\frac{qU}{ckT}},$$

where

$$c = \frac{2b + \cosh\frac{W}{L} + 1}{b + 1},$$

$b = \mu_n/\mu_p$ is the ratio of electron and hole mobilities, *W* is the length of the inversion region (or the region of

Table 2. Composition of silicon epilayers grown from a tin-based solution melt of technical silicon

Analyzer position	Content of components, wt %											
	Si	Na	Mg	Al	P	S	K	Ti	Mn	Fe	Sn	Total
1	99.06	0.07	0.00	0.32	0.00	0.00	0.00	0.12	0.09	0.33	0.90	100
2	99.14	0.06	0.01	0.23	0.00	0.06	0.00	0.03	0.01	0.46	0.95	100
3	99.24	0.00	0.00	0.24	0.00	0.00	0.03	0.00	0.03	0.47	1.17	100

serial resistance) and L is the diffusion length of minority charge carriers.

The spectral sensitivity of epilayers grown from a tin-based solution melt of technical silicon was measured at room and liquid nitrogen temperatures. The measurements were performed using a prism monochromator (Carl Zeiss Jena, Germany). The typical spectra are presented in Fig. 3. The results of photosensitivity measurements at $T = 300$ and 77 K showed that the room temperature spectrum of n-Si(Sn) films is extended toward longer wavelengths ($\lambda = 1.20$ μm) (Fig. 3) as compared to the spectra of silicon films obtained by usual methods, in which the long-wavelength boundary at $T = 300$ K is observed at $\lambda = 1.10$ μm [4–6]. This result indicates that Sn entering into the composition of n-Si(Sn) film introduces an impurity energy level in the bandgap, 1 eV below the conduction band bottom. Light quanta transmitted through the silicon substrate and absorbed in the n-Si(Sn) film generate electron–hole pairs, which are separated at the p–n junction and involved in the photocurrent. Since the epitaxial growth of silicon proceeds from liquid tin (~98%) containing technical silicon (~2%), the epilayer contains an impurity of tin (Table 2), which is an isovalent impurity in silicon. For this reason, such $Si_{1-x}Sn_x$ solid solution layers are characterized by higher mobility μ and lifetime τ of both electrons and holes as compared to the analogous parameters for standard silicon. The presence of Sn also accounts for the extension of photosensitivity toward longer wavelengths. This conclusion agrees with the results reported in [7] on the improved structure parameters of silicon doped by isovalent Sn impurity. As is known [8], the presence of Sn in silicon based solar cells also increases the efficiency of solar energy conversion and slows down degradation of the solar cells. We believe that the same effects can be expected in the epitaxial structures grown using the proposed method. Thus, the epitaxial films of $Si_{1-x}Sn_x$ solid solutions can be successfully used for the fabrication of semiconductor devices such as near-IR photodetectors. The obtained structures can also be used for investigation of the transmission of silicon wafers used in IR optoelectronic devices.

Further investigations require an optimization of the technological process and improvement of the photo-
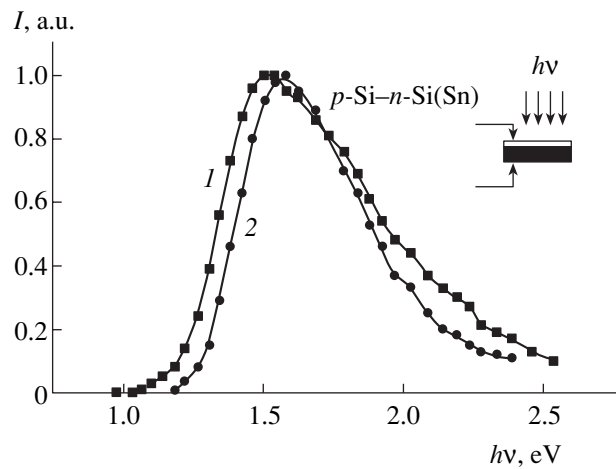
Fig. 3. Typical photosensitivity spectra of epilayers grown from a tin-based solution melt of technical silicon. The measurements were performed at (*1*) 300 K and (*2*) 77 K using light incident from the substrate side.

electric characteristics of silicon epilayers. Such layers will be applicable as active elements in solar cells.

REFERENCES

1. B. Sapaev, Pis'ma Zh. Tekh. Fiz. **29** (20), 64 (2003) [Tech. Phys. Lett. **29**, 865 (2003)].

2. I. V. Stafeev, Zh. Tekh. Fiz. **28**, 1631 (1958) [Sov. Phys. Tech. Phys. **3**, 1502 (1958)].

3. E. I. Adirovich, P. M. Karageorgiĭ-Alkalaev, and A. Yu. Leĭderman, *Double-Injection Currents in Semiconductors* (Sov. Radio, Moscow, 1978), p. 320 [in Russian].

4. M. S. Saidov, Geliotekhnika, No. 3, 4 (2001).

5. M. S. Saidov, É. A. Koshchakov, A. Sh. Razzakov, and U. Nasyrov, Geliotekhnika, No. 3, 16 (1997).

6. *Lightwave Communication Technology: Photodetectors*, Ed. by W. T. Tsang (Academic, New York, 1985).

7. A. S. Saidov, B. Sapaev, Sh. Usmonov, and D. V. Saparov, in *Proceedings of the 3rd National Conference on the Growth, Properties, and Application of Crystals, Tashkent, 2002*.

8. M. K. Bakhadyrkhanov, Kh. M. Iliev, A. R. Toshev, *et al.*, Geliotekhnika, No. 4, 13 (2001).

Translated by P. Pozdeev

Numerical Modeling of the Electrical Properties
of Si–SiO$_2$–VO$_2$ Structures

N. A. Kuldin*, A. A. Velichko, A. L. Pergament, G. B. Stefanovich, and P. P. Boriskov

Petrozavodsk State University, Petrozavodsk, Karelia, Russia
* e-mail: kuldin@psu.karelia.ru
Received August 24, 2004; in final form, February 21, 2005

Abstract—We have numerically modeled the ac current passage through a Si–SiO$_2$–VO$_2$ structure, which is known to exhibit switching with an S-like characteristic due to a metal–semiconductor phase transition in vanadium dioxide. It is shown that the dynamics of switching at high frequencies (10^5–10^9 Hz) can be effectively controlled, which makes such structures promising elements for use in high-frequency microelectronics as analogs of thyristors and photothyristors. © *2005 Pleiades Publishing, Inc.*

The metal–semiconductor phase transition (MSPT) in vanadium dioxide (VO$_2$) and the related phenomenon of electrical switching with an S-like current–voltage characteristic (*I–U* curve) provide a promising basis for the creation of various electronic devices [1]. The room-temperature switching effect is well described in terms of the critical temperature model [1, 2]. According to this model, an increase in the current passing through the structure to a definite threshold value I_{th} leads to Joule heating of the current channel up to a temperature of the direct MSPT ($T_t \sim 340$ K). As a result, the channel conductivity sharply increases, and the new stationary current I is determined by the applied voltage and a limiting resistance in the circuit. As the I value is decreased to a hold current level (I_h), the channel cools down to a temperature of the reverse MSPT ($T_t' \sim 320$–338 K) and the structure passes to a high-ohmic state ($T_t' < T_t$ because of a hysteresis [1]).

Previously, we described [3], a circuit involving the Si–SiO$_2$–VO$_2$ structure (Fig. 1), in which a switching dynamics could be controlled either by varying the bias voltage applied to the Si substrate (U_{Si}) relative to the ground or by changing the illumination intensity (J). The switching control consists in driving the structure from the "on" state (in which the dynamic *I–V* curve has the S-like shape with characteristic spikes in the current oscillograms) to the "off" state (characterized by the *I–V* curve without switching). The mechanism of the switching control is related to spatial redistribution of the ac current in the structure (due to a change in its intrinsic capacitance), whereby the amplitude of current via the VO$_2$ channel in the "on" ("off") state is greater (lower) than I_{th}. For the experimentally studied scheme ($R_1 = 100$ kΩ, $R_2 = 10$ Ω, $R_3 = 560$ kΩ, $C_1 = 0.022$ µF) and the Si–SiO$_2$–VO$_2$ structure configuration ($h = 40$ µm, $l = 13$ µm, $D = 1$ mm, *p*-Si, $\rho_{Si} = 1$ Ω cm;

$d_{SiO_2} \sim 1000$ Å, $d_{VO_2} \sim 3000$ Å), the most effective switching control was provided by applying ac bias voltage with a frequency *f* on the order of 1–10 kHz and an amplitude of $U = 15$ V. If the frequency *f* was increased above 10 kHz, the VO$_2$ channel was strongly shunted via the intrinsic capacitance and it was impossible to provide for the current I_{th} in the channel [4].

Is it possible to control switching in Si–SiO$_2$–VO$_2$ structures at higher frequencies and how do we estimate the maximum possible frequency by the order of magnitude? In order to answer these questions, we have numerically modeled the ac current passage through a Si–SiO$_2$–VO$_2$ structure.

First, let us estimate the characteristic switching time t_s. Cavalleri *et al.* [5] demonstrated that the PSPT development time is less that 10^{-13} s. For this reason, the main contribution to t_s for the thermal mechanism of switching is related to the process of channel cooling down to T_t' (with a characteristic heat removal time τ). Let us model the conducting channel of the structure under consideration using a rectangular rod of length *l*, with metal contacts at the ends occurring at a constant (ambient) temperature T_0. Assuming that the Joule heat is removed only via the contacts, a solution of the heat conduction equation for a finite rod [6] yields the following expression for the evaluation of τ:

$$\tau = \frac{l^2 c \rho}{\pi^2 \lambda}, \qquad (1)$$

where c, ρ, and λ are the heat capacity, density, and thermal conductivity of VO$_2$ in the metal state, respectively. Substituting $c \sim 770$ J/(kg K), $\rho = 4340$ kg/m^3, $\lambda = 9.8$ W/(m K) [7], and assuming $l = 100$ nm, we obtain $\tau \approx 3.5 \times 10^{-10}$ s. For example, a switching time

of ~10^{-9} s for $l \sim 100$ nm in a sandwich structure was experimentally observed in [8]. Thus, we have established that switching in the Si–SiO$_2$–VO$_2$ structure can be observed at frequencies up to 10^9 Hz.

In order to answer the question concerning the possibility of controlled switching in the Si–SiO$_2$–VO$_2$ structure in this frequency range, let us consider a simplified equivalent scheme of this system (Fig. 1c). Here we ignore the small leak resistance R_2, the filter $C_1 R_3$, and the source 2 (these elements constitute a circuit of the dc control voltage U_{Si} applied to the Si substrate and exhibit a weak effect on the ac current passing from the Si substrate to the ground). In the simplified scheme, R_{VO_2} denotes the resistance of the VO$_2$ channel in a semiconducting state at $T \sim T_t$, C_{ox} is the capacitance of the gate insulator SiO$_2$, C_{sc} is the capacitance of the space charge region at the Si–SiO$_2$ interface, and C_{ss} is the capacitance of the surface states (these three capacitances occur under the left contact in Fig. 1a). It should be noted that the capacitance under the right (grounded) contact in Fig. 1a is not involved in the current transfer and, hence, is not taken into consideration. Another simplification of the scheme in Fig. 1c is the absence of the capacitance C_{VO_2} related to the space charge region of the VO$_2$ layer, which corresponds to the ideal case whereby the Al contacts are applied directly onto SiO$_2$. This simplification is also justified by virtue of the higher density n_e of the majority carriers (electrons) in the VO$_2$ film ($n_e \sim 10^{18}$ cm^{-3} [2]; $T_0 \sim 300$ K) in the semiconductor state as compared to the density n_p of the majority carriers (holes) in the Si substrate (p-Si, $n_p \sim N_A = 10^{16}$ cm^{-3}; $T_0 \sim 300$ K; N_A is the acceptor concentration). As a result, the Debye length in the space charge region of the VO$_2$ layer is one order of magnitude smaller than in the space charge region of the Si substrate and, hence, the former region provides a slower contribution to the resulting total structure capacitance.

The control over the current amplitude in R_{VO_2} is provided by changing the total capacitance C through variation of the surface potential ψ_s, which is dependent on U_{Si} [9]. As can be readily seen from the scheme in Fig. 1c, the capacitance C is given by the expression

$$\frac{1}{C} = \frac{1}{C_{ox}} + \frac{1}{C_{sc} + C_{ss}}. \qquad (2)$$

Representing C_{sc} as the sum of three components C_p, C_B, and C_n (corresponding to the space charge regions in the layers of enrichment, depletion and weak
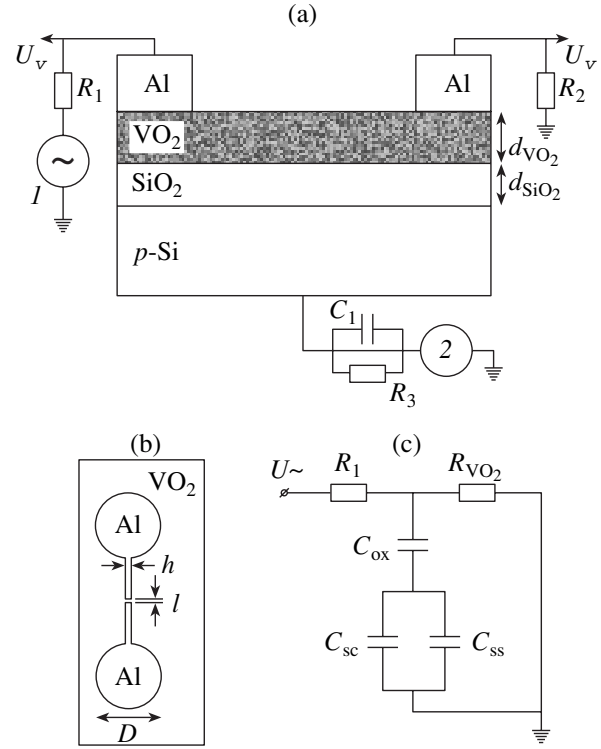

Fig. 1. Schematic diagrams of the Si–SiO$_2$–VO$_2$ structure studied, showing (a) the effective scheme of measurements, (b) the sample geometry, and (c) a simplified equivalent scheme (see text for explanations): (d_{VO_2}) VO$_2$ film thickness; (d_{SiO_2}) SiO$_2$ layer thickness; (1) source of a probing signal with frequency f and amplitude U; (2) source of a dc bias voltage applied to Si substrate; (R_1) limiting resistance; (R_2) bias resistance; $C_1 R_3$ filter; (U_v, I_v) leads for I–U measurements; (l, h) the length and width of the switching channel, respectively; (D) Al contact diameter.

inversion, and strong inversion, respectively) and taking into account the dependence of C_n and C_{ss} on the frequency [9], we can rewrite expression (2) as

$$\frac{1}{C} = \frac{1}{C_{ox}} + \frac{1}{C_p + C_B + \dfrac{C_n}{1 + \omega^2 \tau_n^2} + \dfrac{C_{ss}}{1 + \omega^2 \tau_{ss}^2}}, \qquad (3)$$

where τ_n is the lifetime of minority carriers in the space charge region, τ_{ss} is the characteristic time of recharge of the surface states, and $\omega = 2\pi f$. Note that C_p, C_B, and C_n are added in order to render formula (3) universal for the numerical calculations, rather than because these capacitances are connected in parallel. For various ψ_s, one of these components prevails over the other two [9], so that the sum adequately describes the dependence of C_{sc} on ψ_s.
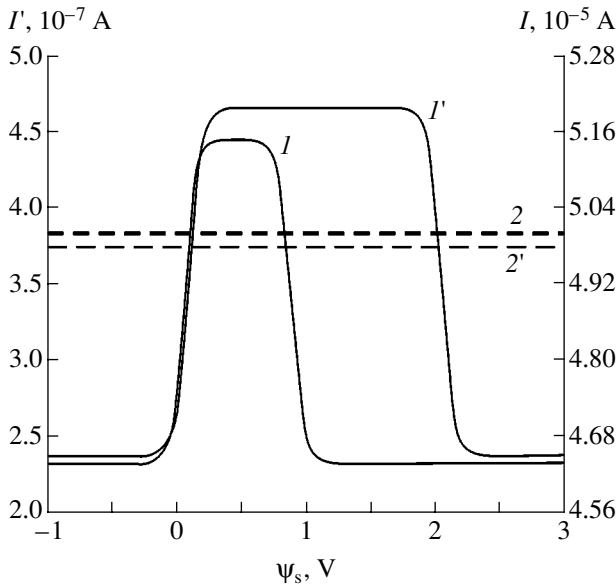
Fig. 2. Calculated plots of the amplitude I of the current via R_{VO_2} versus ψ_s calculated for frequencies $f = 6$ kHz (*1*) and 10^9 Hz (*1'*) and the corresponding critical currents $I_{\mathrm{th}} = 5 \times 10^{-5}$ A (*2*, right scale) and 3.75×10^{-7} A (*2'*, left-hand scale), respectively.

Using the equivalent scheme (Fig. 1c), we readily obtain an expression for the current amplitude I in R_{VO_2}:

$$I = \frac{U}{\sqrt{(R_1 + R_{\mathrm{VO}_2})^2 + (\omega C R_1 R_{\mathrm{VO}_2})^2}}. \tag{4}$$

Taking into account that C_p, C_B, and C_n are functions of ψ_s [9], assuming that the energy spectrum of surface states at the Si–SiO$_2$ interface is quasi-continuous [9], and using formulas (3) and (4), we have calculated the dependence of I on ψ_s at a frequency of $f = 6$ kHz (Fig. 2, curve *1*). These model calculations were performed for $U = 14$ V, $R_1 = 100$ kΩ, $R_{\mathrm{VO}_2} = 160$ kΩ, $h = 40$ μm, $l = 13$ μm, $D = 1$ mm, $S = 7.85 \times 10^{-3}$ cm^2 (contact area), $d_{\mathrm{VO}_2} = 3000$ Å, $\varepsilon_s = 11.9$ (permittivity of Si), $\varepsilon_{\mathrm{ox}} = 3.82$ (permittivity of SiO$_2$), $L_d = 4.06 \times 10^{-6}$ (Debye length), $T = 290$ K, $d_{\mathrm{SiO}_2} = 10^{-5}$ cm, $\varphi_0 = 0.35$ V (distance from the Fermi level to the midgap in the quasi-neutral volume of Si), $N_A = 10^{16}$ cm^{-3} (*p*-Si), $N_{\mathrm{ss}} = 10^{11}$ cm^{-2} eV^{-1} (energy density of the surface states), $\tau_n = 2.5 \times 10^{-4}$ s, $\tau_{\mathrm{ss}} = 10^{-4}$ s, $j_{\mathrm{th}} = 4.17 \times 10^2$ A/cm^2 (critical current density for $I_{\mathrm{th}} = 5 \times 10^{-5}$ A).

As can be seen from Fig. 2, curve *1* intersects the level I_{th} (indicated by dashed line *2*) at two working points, $\psi_s = 0.1$ and 0.84 V, which correspond to two experimentally determined critical control bias voltages: $U_{\mathrm{Si}} = 4.6$ and -12.2 V, respectively [3]. The results

of numerical modeling showed that an increase in the frequency of the signal applied to the structure leads to a decrease in the maximum current amplitude $I_{\max}$, and results in the disappearance of switching if $I_{\max} < I_{\mathrm{th}}$ ($I_{\max}$ and $I_{\min}$ are the maximum and minimum current amplitudes observed for the variation of ψ_s). However, if the switch dimensions (namely, the contact area S) are decreased, the $I_{\max}$ value will again exceed I_{th}.

The parameters of switching, such as the critical current (I_{th}), critical voltage (U_{th}), and R_{VO_2}, can be controlled by changing the interelectrode gap. Indeed, these values can be estimated using the following formulas:

$$I_{\mathrm{th}} = j_{\mathrm{th}} h d_{\mathrm{VO}_2}. \tag{5}$$

$$U_{\mathrm{th}} = \rho_{\mathrm{VO}_2} j_{\mathrm{th}} l, \tag{6}$$

$$R_{\mathrm{VO}_2} = \frac{\rho_{\mathrm{VO}_2} l}{h d_{\mathrm{VO}_2}}, \tag{7}$$

where $\rho_{\mathrm{VO}_2} \sim 14.8$ Ω cm is the resistivity of VO$_2$ film in the semiconductor state at $T \sim T_t$.

Using formulas (1)–(7), we have also calculated the dependence of I on ψ_s at a frequency of $f = 10^9$ kHz (Fig. 2, curve *1'*). These model calculations were performed for the following parameters (differing from those used in the calculations for $f = 6$ kHz): $U = 8$ V, $R_{\mathrm{VO}_2} = 164$ kΩ, $h = 0.3$ μm, $l = 0.1$ μm, $D = 35$ μm, $S = 9.62 \times 10^{-6}$ cm^2 (contact area), $I_{\mathrm{th}} = 3.75 \times 10^{-7}$ A, and $U_{\mathrm{th}} = 0.062$ V. As can be seen from Fig. 2, the passage to the gigahertz frequency range (where $f^{-1} \ll \tau_n, \tau_{\mathrm{ss}}$) is accompanied by a significant shift of one of the working points toward large ψ_s values ($\psi_s > 2$) practically inaccessible for any U_{Si} [9].

Thus, we demonstrated that a decrease in the switch size (e.g., by means of a lithographic process developed for vanadium oxides [10]) leads to reduction of the switching time in the Si–SiO$_2$–VO$_2$ structure and opens the way to reaching a gigahertz frequency range. For $f^{-1} \ll \tau_n, \tau_{\mathrm{ss}}$, the switch has a single critical control bias voltage U_{Si}. The obtained results indicate that Si–SiO$_2$–VO$_2$ structures are a promising element for use in high-frequency microelectronics as analogs of thyristors and photothyristors (the possibility of optical control was demonstrated previously [3]).

REFERENCES

1. A. A. Bugaev, B. P. Zakharchenya, and F. A. Chudnovskiĭ, *Semiconductor–Metal Phase Transition and Its Applications* (Nauka, Leningrad, 1979) [in Russian].

2. P. P. Boriskov, A. A. Velichko, A. L. Pergament, *et al.*, Pis'ma Zh. Tekh. Fiz. **28** (10), 13 (2002) [Tech. Phys. Lett. **28**, 406 (2002)].

3. A. A. Velichko, N. A. Kuldin, G. B. Stefanovich, *et al.*, Pis'ma Zh. Tekh. Fiz. **29** (12), 49 (2003) [Tech. Phys. Lett. **29**, 507 (2003)].

4. N. A. Kuldin and A. A. Velichko, Usp. Sovrem. Estestv. **4**, 44 (2004).

5. A. Cavalleri, C. Toth, C. Siders, *et al.*, Phys. Rev. Lett. **87**, 237401 (2001).

6. Yu. S. Ochan, *Methods of Mathematical Physics* (Vysshaya Shkola, Moscow, 1965) [in Russian].

7. *The Oxide Handbook,* Ed. by G. V. Samsonov, 2nd ed. (Metallurgiya, Moscow, 1978; Plenum Press, New York, 1982).

8. G. Stefanovich, A. Pergament, and D. Stefanovich, J. Phys.: Condens. Matter **12**, 8837 (2000).

9. S. Sze, *Physics of Semiconductor Devices* (Wiley, New York, 1981), Vol. 1.

10. G. Stefanovich, A. Pergament, A. Velichko, *et al.*, J. Phys.: Condens. Matter **16**, 4013 (2004).

Translated by P. Pozdeev

A Theory of Convective Gas Motion
in a Cylindrical Volume

S. O. Gladkov

Moscow State Regional University, Moscow, Russia
e-mail: Sglad@new.mail.ru
Revised manuscript received February 2, 2005

Abstract—The convective motion of gas in the gravitational field is described for an axisymmetric body with the cylinder ends maintained at different temperatures. A system including the equation of heat conduction, the Navier–Stokes equations, and the continuity equation is analyzed. The convective velocity components $v'_z(r, z)$, $v'_r(r, z)$ and the temperature T are determined as functions of the cylindrical coordinates. The time required for the establishment of thermal equilibrium by means of convection and heat conduction is estimated. © 2005 Pleiades Publishing, Inc.

Problems related to the manifestation of convective forces have been extensively studied, as they are of interest both from the standpoint of basic science and in numerous applications. Despite this attention, there is one problem of purely applied significance that remains open: the description of the convective motion of gas in a cavity that has the shape of an extended body of revolution penetrating deep into the Earth (for brevity, this object will be referred to below as a mine) with a total length l and different temperatures at the top (T_0) and bottom (T) ends such that $T > T_0$.

Let us select a cylindrical coordinate system with the axis z coinciding with the mine axis and write a system including the equation of heat conduction, the Navier–Stokes equations with a convective term, and the continuity equation (see, e.g., [1]):

$$\begin{cases} \dfrac{\partial T}{\partial t} + \mathbf{v}\nabla T = \chi\Delta T, & (1) \\[2mm] \dfrac{\partial \mathbf{v}}{\partial t} + (\mathbf{v}\nabla)\mathbf{v} = -\dfrac{\nabla P}{\rho} + \mathbf{g} + \nu\Delta\mathbf{v} - \beta\mathbf{g}(T - T_0), & (2) \\[2mm] \dfrac{\partial \rho}{\partial t} + \mathrm{div}(\rho\mathbf{v}) = 0. & (3) \end{cases}$$

Here, $\mathbf{v}$ is the velocity, t is the time, $\mathbf{g}$ is the acceleration of gravity, P is the pressure, ρ is the gas density, ν is the kinematic viscosity, χ is the thermal diffusivity, and β is the thermal expansion coefficient. We assume that the gas is incompressible, in which case Eq. (3) implies that $\mathrm{div}\,\mathbf{v} = 0$.

Since we are speaking of convection below the ground level on the Earth, it is necessary to take into account (see, e.g., [2]) that the acceleration of gravity for $r \le R$ (where R is the Earth radius) varies as

$$\mathbf{g} = g\frac{\mathbf{r}}{R}, \qquad (4)$$

where $\mathbf{r}$ is the radius vector from the Earth center to the point of observation within a certain region V (under the Earth surface).

First, let us find a solution in the stationary case by putting $\dfrac{\partial T}{\partial t} = \dfrac{\partial \mathbf{v}}{\partial t} = 0$. Then, Eqs. (1) and (2) can be rewritten as

$$\begin{cases} \dot{v}\nabla T = \chi\Delta T, & (5) \\[2mm] (\dot{v}\nabla)\dot{v} = -\dfrac{\nabla P}{\rho} + g\dfrac{\mathbf{r}}{R} + \nu\Delta\dot{v} - \beta g(T - T_0)\dfrac{\mathbf{r}}{R}. & (6) \end{cases}$$

Taking curl (rot) from both parts of Eq. (6), we obtain

$$\Delta\mathrm{rot}\mathbf{v} = \frac{\beta g}{\nu R}[\mathbf{r} \times \nabla T]. \qquad (7)$$

Now let us pass to the most convenient coordinate system with the origin at the middle of the bottom cylinder end, in which case the radius vector of an arbitrary point in the mine is $\mathbf{r}' = \mathbf{R} - \mathbf{l} + \mathbf{r}_0 + \mathbf{r}$, where r_0 is the radius of the bottom end. Introducing the unit vector of normal to the cylinder surface, we may rewrite Eq. (7) as

$$\Delta\mathrm{rot}\mathbf{v} = \frac{\beta g}{\nu}[\mathbf{n} \times \nabla T], \qquad (8)$$

where the differential refers to the new, primed coordinate system (below, the prime sign is omitted). Owing to the cylindrical symmetry, the temperature depends

only on the coordinates r and z. As for the velocity, the equation $\mathrm{div}\,\mathbf{v} = 0$ will automatically be satisfied if this variable has the form of

$$\mathbf{v} = \mathrm{rot}\mathbf{A}, \qquad (9)$$

where $\mathbf{A}$ is the new unknown vector.

Finally, Eqs. (5) and (8) yield

$$\begin{cases} (v_{0z} + v_z')\dfrac{\partial T}{\partial z} = \chi\Delta T, \\[2mm] \Delta^2\mathbf{A} = -\dfrac{\beta g}{\nu}[\mathbf{n}\times\nabla T], \end{cases} \qquad (10)$$

where $\mathbf{v} = \mathbf{v}_0 + \mathbf{v}'$, $\mathbf{v}_0$ is a certain velocity, and $\mathbf{v}'$ is a purely convective velocity component. In deriving system (10), we selected calibration of the vector $\mathbf{A}$ such that $\mathrm{div}\mathbf{A} = 0$. This choice is quite evident, since the only nonzero component of vector $\mathbf{A}$ is A_φ, which is a function of r and z.

In the case of a purely convective motion, we may assume that $\mathbf{v}_0 = 0$. By virtue of the smallness of $\mathbf{v}'$, we can also ignore the nonlinear term $\mathbf{v}'\nabla T$ in the left-hand side of the heat conduction equation, which yields

$$\Delta T = 0.$$

The solution of this equation in the cylindrical coordinate system is well known and can be written as

$$T(r, z) = J_0\!\left(\frac{\lambda r}{r_0}\right)\!\left(C_1 e^{\frac{\lambda z}{r_0}} + C_2 e^{-\frac{\lambda z}{r_0}}\right), \qquad (11)$$

where λ is a parameter of the separation of variables and $J_0(\xi)$ is the zero-order Bessel function. The boundary condition, which can be written in the form of the Newton law,

$$T(r, z)_{r = r_0} = T_0 + (T - T_0)\frac{z}{l},$$

yields

$$T(r, z)_{r = r_0} = T_0 + (T - T_0)\frac{z}{l} \approx T_0 e^{\frac{(T - T_0)z}{T_0}\frac{1}{l}}. \qquad (12)$$

Comparing Eq. (12) to the solution (11), we conclude that $C_2 = 0$, $C_1 = \dfrac{T_0}{J_0(\lambda)}$, and $\lambda = \dfrac{r_0(T - T_0)}{l\,T_0}$. Therefore, the temperature as a function of the coordinates can be written as

$$T(r, z) = T_0\frac{J_0\!\left(\dfrac{T - T_0}{T_0}\dfrac{r}{l}\right)}{J_0\!\left(\dfrac{T - T_0}{T_0}\dfrac{r_0}{l}\right)}e^{\frac{(T - T_0)z}{T_0}\frac{1}{l}}. \qquad (13)$$

Once the solution (13) is known, the second equation in system (10) yields an inhomogeneous biharmonic

equation $\Delta^2 A_\varphi = -\dfrac{\beta g}{\nu}\dfrac{\partial T}{\partial r}$ for the φ component of vector $\mathbf{A}$. Taking into account expression (13), we can rewrite this equation as

$$\Delta^2 A_\varphi = \frac{\beta g(T - T_0)}{\nu l}\frac{J_1(\xi)}{J_0(\xi_0)}e^{\frac{(T - T_0)z}{T_0}\frac{1}{l}}, \qquad (14)$$

where $\xi = \dfrac{(T - T_0)r}{T_0}\dfrac{1}{l}$, $\xi_0 = \dfrac{(T - T_0)r_0}{T_0}\dfrac{1}{l}$, and $J_1(\xi)$ is the first-order Bessel function.

A solution to Eq. (14) can be found in the form of a product,

$$A_\varphi = e^{\frac{(T - T_0)z}{T_0}\frac{1}{l}}\psi(r), \qquad (15)$$

where $\psi(r)$ is a new function satisfying the equation

$$\left[\frac{1}{r}\frac{\partial}{\partial r}\!\left(r\frac{\partial}{\partial r}\right) + \left(\frac{T - T_0}{T_0 l}\right)^2\right]^2\psi = -\frac{\beta g(T - T_0)}{\nu l J_0(\xi_0)}J_0'(\xi). \qquad (16)$$

For all realistic values of the parameters involved in the definition of ξ, this quantity is always significantly smaller than unity. Therefore, $J_0(\xi_0) \approx 1$ and, hence, $-J_1(\xi) = J_0'(\xi) \approx -\dfrac{\xi}{2} = -\dfrac{(T - T_0)r}{2T_0}\dfrac{1}{l}$. As a result, Eq. (16) considerably simplifies and, with neglect of the second term in the left-hand side of this equation,

$$\left[\frac{1}{r}\frac{\partial}{\partial r}\!\left(r\frac{\partial}{\partial r}\right)\right]^2\psi = -Br, \qquad (17)$$

where $B = \dfrac{\beta g T_0}{2\nu l^2}\left(\dfrac{T - T_0}{T_0}\right)^2$. This yields

$$\psi(r) = \frac{Br^5}{225} + \frac{C_1 r^2}{4}\ln r + \frac{C_2 r^2}{4} + C_3\ln r + C_4, \qquad (18)$$

where C_1, C_2, C_3, and C_4 are the integration constants.

Within the framework of the problem under consideration, only the first term in Eq. (18) has a physical sense. Putting all C_i values equal to zero, we obtain

$$\psi(r) = \frac{Br^5}{225}. \qquad (19)$$

Taking into account expression (15), we obtain

$$A_\varphi = \frac{Br^5}{225}e^{\frac{(T - T_0)z}{T_0}\frac{1}{l}}, \qquad (20)$$

and the convective velocity components appear as

$$
\begin{cases}
v_z' = \dfrac{\partial A_\varphi}{\partial r} = \dfrac{Br^4}{45}e^{\alpha\frac{z}{l}}, \\[2mm]
v_r' = -\dfrac{\partial A_\varphi}{\partial z} = -\dfrac{\alpha Br^5}{225l}e^{\alpha\frac{z}{l}},
\end{cases}
\tag{21}
$$

where $\alpha = \dfrac{T - T_0}{T_0}$. According to the above solution procedure, the condition $\mathrm{div}\,\mathbf{v} = 0$ is satisfied automatically. Since $v_z' = \dfrac{dz}{dt}$ and $v_r' = \dfrac{dr}{dt}$, the lines of convective flows can be readily determined by solving the system of equations (21). Since the exponent weakly depends on the coordinate z, the solution to Eq. (21) can be written as

$$
\begin{cases}
r(t) = r_0 e^{\alpha\frac{z}{5l}}, \\[2mm]
z(t) = \dfrac{5l}{4\alpha}\ln\left(1 + \dfrac{4\alpha Br_0^4}{225l}t\right) \approx \dfrac{Br_0^4}{45}t,
\end{cases}
\tag{22}
$$

where r_0 is the radius vector for $z = 0$ (i.e., on the top edge of the mine).

These equations imply that the velocity v_z' along the mine axis remains virtually constant during the entire period of motion of the convective flow:

$$
v_z' = \frac{Br_0^4}{45}.
\tag{23}
$$

The radial velocity v_r' is determined from the evident relation

$$
v_r' = \dot{r} = \frac{\alpha r_0}{5l}\dot{z}e^{\alpha\frac{z}{5l}} \approx \frac{\alpha Br_0^5}{225l}.
\tag{24}
$$

A comparison of solutions (23) and (24) shows that

$$
v_r' \ll v_z'
\tag{25}
$$

and the physical picture is quite clear.

Indeed, the gas flows along the z axis toward the bottom end of the mine due to two factors: gravity and convection. On this background, there is a still slower shift of the flow toward the central axis, along which the flow streams upward (the velocity v_z' changes sign) after reaching the bottom edge.

The time of the convective motion in the radial direction at the bottom edge is $\Delta t = \dfrac{r_0}{v_r'}$. Since the radial velocity according to Eq. (24) is $v_r' = \dfrac{\alpha Br_0^5}{225l}$, we obtain

$\Delta t = \dfrac{225l}{\alpha Br_0^4}$. Using the explicit expression $B = \dfrac{\alpha^2\beta gT_0}{2\nu l^2}$

and taking into account that $\beta = \dfrac{1}{T}$ (for the gas), we eventually obtain

$$
\Delta t = \frac{450\nu l^3}{\alpha^3 gr_0^4}.
\tag{26}
$$

Taking the kinematic viscosity of air $\nu = 0.15$ cm^2/s, the geometric parameters $l = 10^3$ cm and $r_0 = 10^2$ cm, and $g = 10^3$ cm/s^2 and $\alpha = 0.1$, we obtain an estimate of $\Delta t \approx 7$ days. For $\alpha = 1$, this characteristic time decreases by three orders of magnitude and amounts to approximately ten minutes (instead of a week).

The real situation is closer to the first estimate, according to which the gas performs a slow convective downward motion along the side walls of the axisymmetric mine and very slowly shifts to the axis ($r = 0$), after which the heated gas slowly ascends. It is important to evaluate the parameters for which this ascending flow becomes possible. Apparently, this takes place when

$$
\Delta t \le t_0,
\tag{27}
$$

where t_0 is the time of gas cooling by means of heat conduction. Denoting by δ the linear size of the transition region of contact between the gas flow and the bottom edge of the mine, we obtain $t_0 \approx \dfrac{\delta^2}{\chi}$, where χ is the thermal diffusivity of the gas. Using relations (26) and (27), we obtain

$$
l_{cr} \le \alpha^3\sqrt{\frac{g\delta^2 r_0^4}{450\nu\chi}}.
\tag{28}
$$

In particular, $\delta = 1$ cm in air ($\nu = 0.15$ cm^2/s, $\chi = 0.187$ cm^2/s) for the selected values of $\alpha = 0.1$ and $r_0 = 10^2$ cm yields the upper estimate $l_{cr} \le 2$ m.

It should be noted that this estimate is in good agreement with the so-called "freezing depth" of the ground in winter. Indeed, according to the classical approach, this value is determined from the condition $L \sim \sqrt{\chi t^*}$, and for $t^* = 90$ days (cold period of the year) and $\chi = 0.187$ cm^2/s we obtain precisely $L \approx 2$ m (see monograph [3]), so that $L \sim l_{cr}$.

As for the dependence of pressure on the coordinates r, z in the stationary case, the Navier–Stokes equation yields the relation $\dfrac{\partial P}{\partial z} = \rho g + \eta\Delta v_z' - \beta\rho g(T - T_0)$.

According to solution (21), $v'_z \approx \dfrac{Br^4}{45}$. Then, taking the integral over z, we obtain

$$P = P_0 + z\rho\left[g + \frac{16}{45}B\nu r^2 - \beta g(T - T_0) \right],$$

where P_0 is the pressure at $z = 0$. This relation leads to simple conclusions. First, in a convective gas flow ($B \neq 0$), the pressure at each point is proportional to the square of the distance from the symmetry axis. Second, a comparison of the last two terms in square brackets shows that the pressure can both increase and decrease relative to $P = P_0 + \rho gz$.

In conclusion, we considered the laminar convective flow of incompressible gas in a vertical axisymmetric mine situated beneath the ground level and extended in the radial direction, analyzed and estimated the time of convection, established that the vertical and radial components of the convective velocity are nonzero, and numerically evaluated (within the framework of the hydrodynamic approach) the "freezing depth" of the ground and the corresponding physical conditions.

REFERENCES

1. L. D. Landau and E. M. Lifshitz, *Course of Theoretical Physics*, Vol. 6: *Fluid Mechanics* (Nauka, Moscow, 1986; Pergamon, New York, 1987).

2. S. O. Gladkov, Zh. Tekh. Fiz. **73** (8), 19 (2003) [Tech. Phys. **48**, 958 (2003)].

3. H. S. Carslaw and J. C. Jaeger, *Conduction of Heat in Solids* (Clarendon Press, Oxford, 1959).

Translated by P. Pozdeev

Self-Defocusing of Laser Radiation in a Composite Material Containing ZnSe:O Nanoparticles

O. P. Vinogradova, M. S. Marukhina, and A. I. Sidorov*

Institute of Laser Physics, St. Petersburg, Russia
** e-mail: sidorov@ilph.spb.su*
Received February 7, 2005

Abstract—We present experimental data on the self-defocusing of nanosecond pulses of 0.53-, 1.06-, and 1.54-μm laser radiation in a thick composite material containing nanoparticles of oxygen-doped zinc selenide. This medium can provide for a linear transmission coefficient of 50–60% at a 20–50 pJ energy threshold for the onset of a nonlinear optical response. © *2005 Pleiades Publishing, Inc.*

The phenomenon of radiation self-defocusing accompanying the photogeneration of free charge carriers in semiconductors is of practical interest from the standpoint of the creation of nonlinear optical switches and radiation limiters. This phenomenon has been studied in sufficient detail for single crystals of both the undoped semiconductors (Si, GaAs, ZnSe [1, 2]) and those containing deep impurity levels [3]. In the former case, a nonequilibrium charge carrier density was created by single- or two-photon interband transitions, while in the latter case this was achieved via photoionization of the deep impurity levels. In both cases, the primary process is the absorption of radiation. For this reason, the transmission coefficient of the medium before the onset of a nonlinear response usually falls within 1–30% in the visible spectral range and 50–80% in the near IR range.

This paper demonstrates the possibility of increasing the linear transmission coefficient of a medium featuring self-defocusing by using composite materials containing semiconductor nanoparticles.

The experiments were performed with a matrix containing zinc selenide (ZnSe) nanoparticles doped with oxygen to a concentration of 10^{16}–10^{17} cm^{-3}. The average nanoparticle size was about 50 nm. The ZnSe:O nanoparticles were introduced into the matrix—an optical epoxy compound—to a volume fraction of 0.5–1%. The composite samples had a thickness of 5 mm. The radiation sources were a YAG:Nd laser ($\lambda = 0.53$ and 1.06 μm; $\tau = 10$ ns) and an erbium glass laser ($\lambda = 1.54$ μm; $\tau = 20$ ns).

The composite samples were transparent in the visible spectral range (with a slight yellowish tint), whereas ZnSe:O single crystals with a dopant concentration of 10^{16}–10^{17} cm^{-3} have a dark-brown color. Figure 1 shows the typical transmission spectra of a ZnSe:O single crystal (*1*), a pure epoxy compound (*2*), and a composite material containing ZnSe:O nanoparticles (*3*). As can be seen, the linear transmission of the

composite material is significantly higher than that of the ZnSe:O single crystal: at $\lambda = 0.5$ μm, the transmission coefficients are $T = 0.5\%$ and 60%, and at $\lambda = 0.7$ μm, these values are $T = 8$ and 59%, respectively. For $\lambda > 1.4$ μm, the gain in transmission is absent because of the intrinsic absorption of the epoxy compound. However, one can expect that, by selecting a proper transparent matrix for nanoparticles, it is possible to provide for an increase in the transmission coefficient in the range of $\lambda = 1.4$–2 μm as well.

The scheme of optical measurements is depicted in the inset to Fig. 2a. A composite sample was placed into the focal plane of a telescope with a 9-cm focal length of the first lens. A diaphragm ensured the transmission of 95% of radiation prior to the onset of the nonlinear response. Figure 2 presents experimental plots of the output radiation energy E_{out} measured behind the diaphragm versus the incident radiation energy E_{in}. For
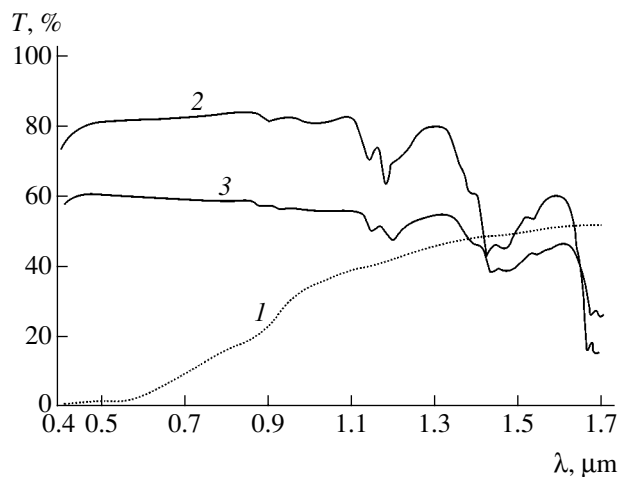
Fig. 1. The typical transmission spectra of (*1*) a ZnSe:O single crystal, (*2*) a pure epoxy compound, and (*3*) composite material containing ZnSe:O nanoparticles (all samples had a thickness of 5 mm).
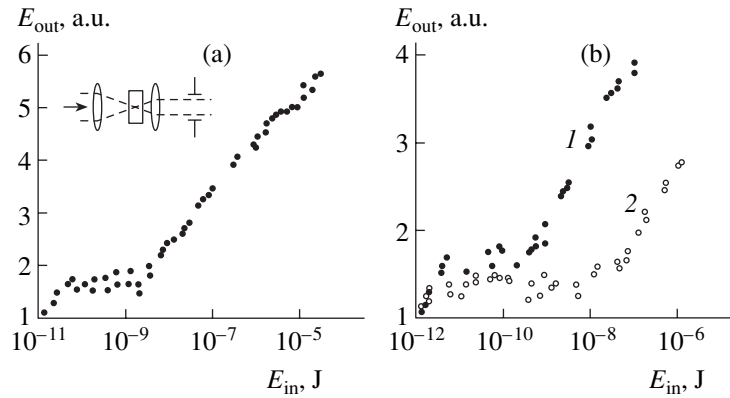
Fig. 2. Experimental plots of the output radiation energy E_{out} versus the incident radiation energy E_{in} for a composite material with ZnSe:O nanoparticles: (a) $\lambda = 0.53$ μm; (b) $\lambda = 1.06$ μm (*1*) and 1.54 μm (*2*). The inset shows the scheme of optical measurements.

$\lambda = 0.53$ μm, the threshold for the onset of the radiation limitation is $E_{thr} = 30$ pJ, and the dynamic range D of the limitation is $D = 100$ (D is defined as the ratio of the maximum energy for which the limitation takes place to the threshold value). For $\lambda = 1.06$ μm, we have $E_{thr} = 3$ pJ and $D = 200$; and for $\lambda = 1.54$ μm, we have $E_{thr} = 2$ pJ and $D = 4 \times 10^3$. Note that the curve for $\lambda = 0.53$ μm exhibits a limitation region at $E_{in} = 1$–10 μJ.

The phenomenon of radiation limitation in the composite material is related to the radiation self-defocusing that accompanies the single-photon photoexcitation of free charge carriers from deep impurity levels in ZnSe:O nanoparticles. An increase in the charge carrier density leads to a decrease in the index of refraction of nanoparticles in the region of radiation energy deposition. This results in a decrease in the effective refraction index composite and in the formation of a negative dynamic lens [4]. The limitation threshold decreases with increasing radiation wavelength because the nonlinear additive to the refractive index varies as $\Delta n \sim \lambda^2$. The limitation effect increases with the incident energy E_{in}, which is related to two factors: (i) saturation of the impurity absorption and (ii) the formation of a positive dynamic lens as a result of the radiation-induced heating of nanoparticles. Since the optical absorption of ZnSe:O increases with decreasing radiation wavelength (Fig. 1, curve *1*), these thermal processes most significantly influence the dynamic range of limitation in the visible spectral range. However, an additional contribution to the limitation at $\lambda = 0.53$ μm may be due to the two-photon interband absorption (Fig. 2a, $E_{in} = 1$–10 μJ). The composite material is characterized by a significant (50- to 100-fold) decrease in the dynamic range of limitation as compared to semiconductor single crystals [3], which is related to the lower density of active centers in the former case.

Thus, using a composite material containing semiconductor nanoparticles with deep impurity levels, it is possible to obtain a high linear transmission coefficient in the visible and near IR spectral ranges, with a threshold for the onset of a nonlinear optical response on a level of several units or tens of picojoules. Such materials can be used for the creation of low-threshold optical switches and radiation limiters.

REFERENCES

1. T. F. Boggess, S. C. Moss, J. W. Boyd, *et al.*, Opt. Lett. **9**, 291 (1984).

2. E. W. Van Stryland, Y. Y. Wu, D. J. Hagan, *et al.*, J. Opt. Soc. Am. B **5**, 1980 (1988).

3. I. V. Bagrov, A. P. Zhevlakov, A. I. Sidorov, *et al.*, Opt. Zh. **69** (2), 15 (2002).

4. A. I. Sidorov, Pis'ma Zh. Tekh. Fiz. **29** (7), 77 (2003) [Tech. Phys. Lett. **29**, 300 (2003)].

Translated by P. Pozdeev

A Method for Determining the Main Mechanical Properties of Soft Soils at High Strain Rates (10³–10⁵ s⁻¹) and Load Amplitudes up to Several Gigapascals

A. M. Bragov[a],*, A. K. Lomunov[a], I. V. Sergeichev[a],
W. Proud[b],**, K. Tsembelis[b], and P. Church[c],***

[a] *Research Institute of Mechanics, Nizhni Novgorod State University, Nizhni Novgorod, Russia*
[b] *Cavendish Laboratory, Cambridge University, Cambridge, UK*
[c] *QinetiQ, Lethal Mechanisms, Fort Halstead, Sevenoaks, UK*
*e-mail: * bragov@mech.unn.ru; ** wgp1000@phy.cam.ac.uk; ***PDChurch@qinetiq.com*
Received February 8, 2005

Abstract—A new method has been developed for determining the main laws of the deformation of soft soils under conditions of dynamic loading with amplitudes of up to several gigapascals. The method is based on the results of high-strain-rate tests under uniaxial deformation conditions, which were obtained using a modified Kolsky method and the plane shock wave technique. The possibilities of the proposed method are illustrated by determining the dynamic properties of sand. © *2005 Pleiades Publishing, Inc.*

The dynamic properties of soft soils in the range of loads up to 100 MPa and strain rates up to 10^2 s⁻¹ have been investigated in great detail [1–5]. The compressibility of soft soils loaded by shock waves with amplitudes up to several gigapascals was studied in [6–8]. However, the range of high dynamic loads (from 50 MPa to 5 GPa) and high strain rates (10^3–10^5 s⁻¹) remains insufficiently studied.

At present, the dynamic properties of soft soils at a strain rate on the order of $\sim10^3$ s⁻¹ are studied using a modified Kolsky method [8]. According to this method, a sample in a rigid jacket is placed between two hard pressure bars. It has been shown [9] that the stressed state under these conditions can be considered as volumetric, while the deformation is uniaxial. We propose to supplement the measurement of strain pulses in the pressure bars by the measurement of strain at the container circumference with the aid of strain gages. This modification makes it possible to measure the uniaxial stress–strain ($\sigma_x \sim \varepsilon_x$) curve, the volume compressibility ($P \sim \rho$) curve, the pressure dependence of the shear strength ($\tau \sim P$), and the lateral thrust coefficient—all in one experiment.

Recently, it was demonstrated [10] that the range of applicability of the modified Kolsky method in the determination of the $\sigma_x \sim \varepsilon_x$, $P \sim \rho$, and $\tau \sim P$ dependences is restricted to axial stresses on the order of 500 MPa. Higher load amplitudes are achieved in the case of shock wave loading. Such experiments are usually performed so as to measure a shock wave adiabate relating the longitudinal stress σ_x to the axial strain ε_x. Since the stressed states realized in the modified Kolsky method and in the case of plane shock wave loading are

similar, the joint use of the results obtained by these techniques allows the uniaxial compression curve $\sigma_x \sim \varepsilon_x$ to be constructed in a wide range of strain rates and load amplitudes. An example of such construction is presented in the figure (curves *1* and *2*), which illustrates the example considered below.

In order to construct the compressibility curve $P \sim \rho$ based on the results of a plane shock wave test at moderate loads, it is necessary to measure two components of the stress tensor. In the case of soils, such measurements are difficult to perform. For this reason, we propose to determine the pressure P from the obtained shock wave adiabate $\sigma_x \sim \varepsilon_x$ using the following procedure.
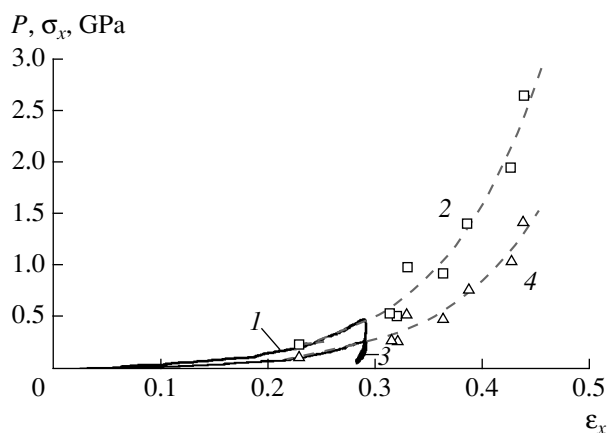
Complete compressibility curves $\sigma_x \sim \varepsilon_x$ (*1, 2*) and $P \sim \varepsilon_x$ (*3, 4*) constructed for sand using the experimental dynamic diagrams (*1, 3*) and the shock wave adiabates (*2, 4*).

Granulometric composition of sand

Particle size, mm	1.6	1	0.63	0.4	0.315	0.2	0.16	0.1	0.063	0.05	0.001
Fraction content, %	0.03	0.375	4.425	22.955	18.035	40.09	9.22	3.31	0.42	0.215	0.265

From the available experimental data, it was established that the relation between the shear strength and the pressure for soft soils loaded up to ~500 MPa is close to linear [2, 3, 10]:

$$\tau = a + (\tan\varphi)P, \tag{1}$$

where a is the cohesion and φ is the internal friction angle.

Let us assume that this relation is also valid at higher pressures (up to several gigapascals). Indirect evidence of the validity of this assumption is provided by the results of plane shock wave tests, in which two stress tensor components were determined for a cement mortar [11].

For uniaxial deformation, we have

$$P = \sigma_x - \frac{4}{3}\tau. \tag{2}$$

Using this formula and the linear relation (1), we obtain an expression for the pressure as a function of the stress σ_x:

$$P = \frac{\sigma_x - 4/3 a}{1 + 4/3 \tan\varphi}. \tag{3}$$

Thus, under the above assumption, this expression provides the relation $P \sim \varepsilon_x$ (or $P \sim \rho$) in the region of shock-wave compression, proceeding from the shock adiabate $\sigma_x \sim \varepsilon_x$ and using the known values of a and $\tan\varphi$. In combination with the $P \sim \varepsilon_x$ curve obtained using the modified Kolsky method, this provides the complete $P \sim \varepsilon_x$ relation for a broad range of load amplitudes.

As an example, we present data obtained from the dynamical tests performed for sand with a density of ~1.5 g/cm^3 and the granulometric composition presented in the table. The coefficients in relation (1), determined using the modified Kolsky method, are $a \approx 0$ and $\tan\varphi = 0.643$. The results of plane shock wave tests [11] gave the linear shock wave adiabate, $D = A + BU$, where D is the shock wave velocity, U is the mass velocity, and $A = 510.9$ m/s and $B = 1.71$ are constant coefficients. Using this adiabate and expression (3), it is possible to construct a compressibility curve $P \sim \varepsilon_x$ or $P \sim \rho$.

The complete $\sigma_x \sim \varepsilon_x$ (1, 2) and $P \sim \rho$ (3, 4) curves constructed as described above are depicted in the figure, where curves 1 and 3 represent the dynamic diagrams obtained using the Kolsky method, while curves 2

and 4 are the shock wave adiabates constructed using the results of plane shock wave tests. As can be seen, the results obtained by the two independent methods are in good agreement and complement each other, thus significantly expanding the domain of determination of the main laws for the deformation of soils.

Conclusion. We proposed a new method for determining the main laws of the high-rate straining of soft soils in a broad range of variation of the impact load amplitude and strain rate. This method was successfully used to determine the main dynamic properties of sand. We believe that the experimental data obtained using the proposed method may provide the parameters and constants necessary for the development of mathematical models of soft soils.

REFERENCES

1. S. S. Grigoryan, Prikl. Mat. Mekh. **24**, 1057 (1960).

2. G. M. Lyakhov, *Waves in Soils and Porous Multicomponent Media* (Nauka, Moscow, 1982) [in Russian].

3. Kh. A. Rakhmatulin, A. Ya. Sagomonyan, and N. A. Alekseev, *Soil Dynamics* (Izd. MGU, Moscow, 1964) [in Russian].

4. A. A. Vovk, B. V. Zamyshlyaev, L. S. Evterev, *et al.*, *Soil Behavior under Pulsed Load* (Naukova Dumka, Kiev, 1984) [in Russian].

5. A. Gasagrande and W. Z. Schanon, Proc. Am. Soc. Civ. Eng. **74** (4), 29 (1948).

6. M. D. Dianov, N. A. Zlatin, S. M. Mochalov, *et al.*, Pis'ma Zh. Tekh. Fiz. **12**, 529 (1976) [Sov. Tech. Phys. Lett. **12**, 207 (1976)].

7. V. A. Lagunov and V. A. Stepanov, Prikl. Mekh. Tekh. Fiz., No. 1, 88 (1963).

8. A. M. Bragov, G. M. Grushevsky, and A. K. Lomunov, Exp. Mech. **36**, 237 (1996).

9. A. M. Bragov, G. M. Grushevsky, and A. K. Lomunov, DYMAT J. **1**, 253 (1994).

10. A. M. Bragov, V. L. Kotov, A. K. Lomunov, and I. V. Sergeichev, Prikl. Mekh. Tekh. Fiz. **45**, 147 (2004).

11. K. Tsembelis, W. G. Proud, B. A. M. Vaughan, and J. E. Field, in *Proceedings of the 14th DYMAT Technical Meeting "Behavior of Materials at High Strain Rates: Numerical Modeling," Sevilla, 2002*, pp. 193–203.

Translated by P. Pozdeev

Determining the Control Functions of Wave Processes in Regions with Mobile Boundaries for a Plasma Cylinder of Finite Length Expanding in a Compressible Medium

V. S. Krutikov

Institute of Pulse Processes and Technologies, National Academy of Sciences of Ukraine,
Nikolaev, Ukraine
e-mail: iipt@iipt.com.ua
Received February 17, 2005

Abstract—Exact analytical solutions of the wave equation in regions with mobile boundaries for the general case of cylindrical symmetry are obtained using an original method developed previously for solving inverse problems with allowance for the interaction of nonlinear arguments. The obtained solutions are universal and are valid for both inverse and direct problems. A method of eliminating logarithmic singularities, known to exist in the case of cylindrical symmetry, is proposed for the quantitative determination of the control functions of wave processes in regions with mobile boundaries, including the case of a plasma cylinder of finite length expanding in a compressible medium. © 2005 Pleiades Publishing, Inc.

Description of the expansion of a plasma cylinder [1] of finite length presents an extremely complicated multidimensional wave problem in a region with mobile boundaries. Observations with the aid of a high-speed photochronograph show that the expanding plasma cylinder transforms with time into a cavity with a dumbbell shape [2, 3]. To date, numerical solutions have been obtained (e.g., by the Godunov method [4–6]) only for direct problems of this kind.

This study presents an attempt to find the control functions (pressure and velocity at the mobile boundary) for the wave processes induced by a plasma cylinder of finite length. Problems of this kind have not previously been considered in mathematical physics.

Let us consider the physical phenomena involved in the initial stage of plasma cavity expansion, for a period of time within $t = 0$–15 μs, which approximately corresponds to the process of energy deposition. This process determines (with a certain delay $t^0 = (r_1 - r_0)/a$) the form of the pressure function $P(r_1, t)$ at a point with the radius r_1. For this time, even at a constant velocity of $v^*(R(t), t) = 200$ m/s = const [7], the cavity size will reach $R(t) = r_0 + v^*t = 3.1 \times 10^{-3}$ m, where $r_0 = 0.1$ mm is the initial radius. Thus, the plasma front occurs between electrodes (spaced by ~8 mm) or between the electrode and wall (for the electric discharge in liquid). For this reason, in calculating the volume V for the energy balance equation according to the Godunov method [4–6], we may consider only the radial velocity as producing the maximum contribution to the function $P(r_1, t)$ in the period of time under consideration ($t = 0$–15 μs).

It is also physically clear that the control functions for the expansion of both the infinite cylinder and a cylinder of finite length l will be identical in a certain time interval $\Delta t = c/a - t^0$, where $c = [(0.5l)^2 + (r_1 - r_0)^2]^{1/2}$. During this period of time, the expansion of the infinite cylinder parts greater than l will not be manifested at a point with the radius r_1. Proceeding from these considerations, we may choose a time interval in which the control functions for the infinite and finite cylinders are identical. In selecting the approximating control functions, we may assume that the parameters (constants) of these functions determined for the time interval of coincidence can also be used for determining the control functions for the moments of time that are somewhat outside this interval. The initial (preset) shape of the function $P(r_1, t)$ used for the reconstruction (and for determining the aforementioned parameters) bears information that it is induced by the expansion of a cylindrical plasma cavity of finite length.

A wave equation with cylindrical symmetry has the following form:

$$\varphi_{tt} - a^2 \varphi_{rr} - a^2 r^{-1} \varphi_r = 0, \tag{1}$$

where φ is the velocity potential, r is the coordinate, t is the time, and a is the velocity of the perturbation propagation in the initially unperturbed liquid medium. Considering zero initial conditions and using the

method of solving inverse problems with allowance for the interaction of nonlinear arguments (this method is described in detail in [8–11]), we obtain in the general case the following control functions $P(R(t), t)$ (case 1) and $v(R(t), t)$ (case 2):

$$\left| \int_0^t P(r, t - \tau) X(r_1) d\tau = \int_0^t f(r, \xi - \tau) X(r) d\tau \right|_{r = R(t)}, \quad (2)$$

$$\left| \rho \int_0^t v(r, t - \tau) X(r_1) d\tau \right.$$
$$= \left. \int_0^t \frac{1}{r} f(r, \xi - \tau) X(r) \left(\tau + \frac{r}{a} \right) d\tau \right|_{r = R(t)}, \quad (3)$$

$$\left| \frac{\rho}{2} \int_0^t [r^2(t - \tau) - r_0^2] X(r_1) d\tau \right.$$
$$= \left. \int_0^t f^*(r, \xi - \tau) X(r) \left(\tau + \frac{r}{a} \right) d\tau \right|_{r = R(t)}, \quad (4)$$

$$X(r) = \left(\tau^2 + 2 \frac{r}{a} \tau \right)^{-1/2}, \quad X(r_1) = \left(\tau^2 + 2 \frac{r_1}{a} \tau \right)^{-1/2},$$

$$\xi = t - \frac{r - r_0}{a}, \quad f^* = \int_0^t f(r, \xi) dt.$$

Setting the image function $P(r_1, t) = A[(t + \beta)^2 - (r_1/a)^2]^{-1/2}$ in the class of Bessel functions [14], we obtain the control functions in cases 1 and 2 in the following form:

$$P(R(t), t) = \frac{A}{\omega} - \frac{1}{2} \rho v^2(R(t), t),$$
$$v(R(t), t) = \frac{A(t + \beta)}{R(t) \rho \omega}, \quad (5)$$

$$R(t) = \left\{ r_0^2 + \frac{2A}{\rho} [\omega - \omega_1] \right.$$
$$\left. + \frac{2A^2}{\rho^2 a^2} \left[\ln \left| \omega - \frac{A}{\rho a^2} \right| - \ln \left| \omega_1 - \frac{A}{a^2 \rho} \right| \right] \right\}^{1/2}, \quad (6)$$

where

$$\omega = \sqrt{(t + \beta)^2 - \frac{R^2(t)}{a^2}}, \quad \omega_1 = \sqrt{\beta^2 - \frac{r_0^2}{a^2}},$$

$$\beta = \alpha + \frac{r_0}{a}, \quad A, a, \rho, r_0, \alpha = \text{const}.$$

In particular, for $t \longrightarrow 0$,

$$P(R(t), t)$$
$$= A[\zeta^2 - (r_0/a)^2]^{-1/2} - 0.5 \rho v^2(R(t), t), \quad (7)$$

$$v(R(t), t) = A\zeta/r_0 \rho [\zeta^2 - (r_0/a)^2]^{-1/2},$$
$$\zeta = \alpha + r_0/a, \quad (8)$$

and for $a \longrightarrow \infty$,

$$R(t) = (r_0 + 2At\rho^{-1})^{1/2}. \quad (9)$$

It should be noted that, for $\alpha \longrightarrow 0$ and $r_0 \longrightarrow 0$, formulas (5)–(9) transform into expressions obtained previously [11, Eqs. (8)–(10)].

In order to determine the control functions in cases 1 and 2 using Eqs. (2) and (3), respectively, it is necessary to know the law of variation of the mobile boundary radius. Calculations of the $R(t)$ function using Eq. (4) encounter difficulties, since the unknown function $R(t)$ enters into the argument of the function on the right-hand side of this equation. For this reason, the solution is obtained using the iterative method described previously [12]. It should be noted that Baev [13] also used the iterative method for solving inverse wave problems of a different kind, not involving mobile boundaries.

The iterative procedure begins with determining the r_2 value. This point is selected, based on the physical sense, as the nearest point not reached by the mobile boundary within the period of time under consideration. Since $v(R(t), t)$ is unknown, r_2 can be approximately set with a safety margin (a) for $v(R(t), t) = \text{const} = 200$ m/s [7] or (b) using formulas (5)–(9); the jump of pressure $P(r_1, t)$ for the inverse problem is known. The initial radius r_0 and the finite length l of the expanding cylinder must be chosen. It should be taken into account that a preset law of variation of the pressure $P(r_1, t)$ can be provided for various r_0 and l values, but the laws of boundary motion may also be substantially different.

The two-dimensional problem for a liquid flowing in electric discharge (free of any limitations related to the one-dimensional and nonlinear character of the flow and consistent with the experimental results [7–9]) is described by a system of hydrodynamic equations [4–6].

$v(R(t), t)$, m/s

$P(r_1, t)/P_0$

200

100

10   20 130   160

t, μs
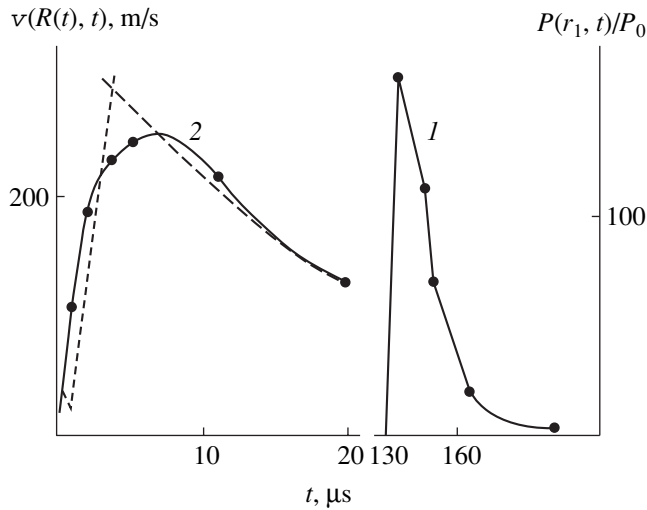
Reconstruction of the control function $v(R(t), t)$ from a preset pressure $P(r_1, t)$ (curve *1*) induced at point r_1 by a cylindrical plasma piston of a finite length: dashed curve *2* shows the first approximation; solid curves present the results of calculations for the direct problem solved using the Godunov method.

The relationship between the channel volume, the pressure, and the power deposited in the channel was suggested by Naugol'nykh and Roĭ (see [3, Eq. (3.44)]). The results of calculations performed in [6] using the Godunov method [4] for a system of equations ([6, Eq. (1)] and [3, Eq. (3.44)]) describing the expansion of a plasma cylinder with $l = 50$ mm are presented for $v(R(t), t)$ and $P(r_1 = 0.2$ m, $t)$ in the figure. The latter result (curve *1*) was used in the reconstruction and approximated as follows:

$$P(r_1, t) = D(t - t^0)\sigma_0(t - t^0)$$
$$- D(t - t^0)\sigma_0(t - \alpha_2) + \sum_{m=0}^{\infty} A_m(t - \alpha_2)^m, \quad (10)$$

where $m = 0$–3, $A_0 = 163$, $A_1 = -5.60(6) \times 10^6$, $A_2 = 0.201(9) \times 10^{12}$, $A_3 = -0.0161(3) \times 10^{18}$, $\alpha_2 = t_0 + 4 \times 10^{-6}$ s $= 140.85$ μs, σ_0 is the zero-order unit step function, $\alpha_1 = t^0 = 136.85$ μs, $D = (163/4) \times 10^{-6} = 40.75 \times 10^6$ kgf/(cm^2 s), and $P_{max}(r_1, t) = 163$. The Lagrange multipliers A_m bear information that the wave processes are induced by the expansion of a cylinder of finite length.

Using Eq. (3) (for $r = R(t) \approx r_2$, $a = 1460$ m/s, $\rho = 102$ (kgf s^2)/m^4, $r_0 = 0.2$ mm, $r_1 = 0.2$ m), the right-hand part of Eq. (10), and the expansion $v(R(t), t) =$

$\sum_{m=0}^{4} C_m t^m$ for $t = (0.5, 1, 2, 3,$ and $4) \times 10^{-6}$ s, we obtain a system of algebraic equations:

$$\rho \int_0^t \sum_{m=0}^{4} C_m(t - \tau)^m X(r_1)d\tau = D\frac{1}{r_2}\int_0^t \left[\left(\xi - \frac{r_2}{a}\right)\tau X(r_2)\right.$$
$$\left. - \tau^2 X(r_2) + \xi\frac{r_2}{a}\right]d\tau, \quad \xi = t - \frac{r_2 - r_0}{a}, \quad (11)$$

where $r_2 = 0.73$ mm (with the "margin") according to formula (9) with $A = 163 \times 10^{-6}$ (kgf s)/cm^2 for a jump in $P(r_1, t)$. Solving this system, we obtain $C_0 = 44.966053$, $C_1 = -1.58226 \times 10^8$, $C_2 = 1.867363 \times 10^{14}$, $C_3 = -5.8156 \times 10^{19}$, and $C_4 = 6.454306 \times 10^{24}$. This result corresponds to the ascending branch of the dashed curve. For a period of time $t > 4$ μs, let us approximate the control function as $v(R(t), t) = A\exp(-\alpha_1 t)$, where A and α_1 are the constant parameters to be determined. The value of $A = v(R(t), t = 0) = 357.35$ m/s was determined using Eqs. (5)–(9) with $r_0 = 0.2$ mm, $r_1 = 0.2$ m, $t_0 = 136.849315$ μs, and $\alpha = 0.003649699 \times 10^{-6}$ [14]. Taking into account this approximation and using the expansion $\exp(\alpha_1 \tau) = 1 + \alpha_1\tau + \ldots$, relation (3) can be written as in [12, Eq. (15)]. For $t = 6.5$ μs and $r_2 = 1.3$ mm, we obtain $\exp(-\alpha_1 \cdot 6.5)\{1.11847049 + \alpha_1 \cdot 2.4157629\} = 0.840076478$. This equation can be solved using conventional methods, which yield $\alpha_1 = 0.0523 \times 10^6$. Finally, we obtain $v(R(t), t) = 357.35\exp(-0.0523 \times 10^6 t)\sigma_0(t - 4 \times 10^{-6})$ m/s.

An analysis of the results shows that the proposed approach allows the control functions for a wave process in the expanding cylindrical plasma piston of a finite length to be correctly evaluated already in the first approximation. This reduces to a minimum the number of trials (experimental or numerical) required for selecting the characteristics of a pulsed source or process necessary to obtain the desired action functions $P(r_1, t)$ and $v(r_1, t)$. There are no other means of reaching the goal except those described above; solving the inverse problems using the methods described in [15] is problematic.

REFERENCES

1. V. K. Kedrinskiĭ, Prikl. Mekh. Tekh. Fiz., No. 4, 23 (1987).

2. L. M. Lyamshev, Usp. Fiz. Nauk **151**, 479 (1987) [Sov. Phys. Usp. **30**, 252 (1987)].

3. K. A. Naugol'nykh and N. A. Roĭ, *Electrical Discharge in Water* (Nauka, Moscow, 1971) [in Russian].

4. *Numerical Solution of Multidimensional Problems of Gas Dynamics*, Ed. by S. K. Godunov (Nauka, Moscow, 1976) [in Russian].

5. L. V. Shurshalov, Zh. Vychisl. Mat. Mat. Fiz., No. 4, 793 (1980).

6. G. A. Barbashova and A. V. Ivanov, Gidromekhanika (Kiev), No. 53, 16 (1986).

7. V. S. Krutikov, Akust. Zh. **42**, 534 (1996) [Acoust. Phys. **42**, 471 (1996)].

8. V. S. Krutikov, *One-Dimensional Problems in the Mechanics of Continuous Media with Moving Boundaries* (Naukova Dumka, Kiev, 1985) [in Russian].

9. V. S. Krutikov, Dokl. Akad. Nauk **364**, 17 (1999).

10. V. S. Krutikov, Pis'ma Zh. Tekh. Fiz. **14**, 510 (1988) [Sov. Tech. Phys. Lett. **14**, 226 (1988)].

11. V. S. Krutikov, Dokl. Akad. Nauk **368**, 755 (1999) [Dokl. Phys. **44**, 674 (1999)].

12. V. S. Krutikov, Pis'ma Zh. Tekh. Fiz. **31** (1), 9 (2005) [Tech. Phys. Lett. **31**, 4 (2005)].

13. A. V. Baev, Dokl. Akad. Nauk SSSR **287**, 1358 (1986) [Sov. Phys. Dokl. **31**, 314 (1986)].

14. V. S. Krutikov, Pis'ma Zh. Tekh. Fiz. **29** (24), 7 (2003) [Tech. Phys. Lett. **29**, 1014 (2003)].

15. G. A. Grinberg, Prikl. Mat. Mekh. **31**, 193 (1967).

Translated by P. Pozdeev